DEVELOPMENT AND CHARACTERIZATION OF A CONTINUOUS-FLOW OPTICAL PUMPING SYSTEM

by

Josephine Lee Herman
Bachelor of Science, McGill University

THESIS SUBMITTED IN PARTIAL FULFILLMENT
OF THE REQUIREMENTS FOR THE DEGREE OF
MASTER OF SCIENCE
IN THE DEPARTMENT
OF
PHYSICS

SIMON FRASER UNIVERSITY
Fall 2006

APPROVAL

Name:	Josephine Lee Herman
Degree:	Master of Science
Title of Thesis:	Development and Characterization of a Continuous-Flow Optical Pumping System
Examining Committee:	Dr. J. Bechhoefer, Professor (Chair)

Dr. M.E. Hayden, Associate Professor
Senior Supervisor

Dr. J.S. Dodge, Assistant Professor
Supervisor

Dr. N. Forde, Assistant Professor
Supervisor

Dr. D. Broun, Assistant Professor
Internal Examiner

Date Approved: October 5, 2006

SIMON FRASER UNIVERSITY library

DECLARATION OF PARTIAL COPYRIGHT LICENCE

The author, whose copyright is declared on the title page of this work, has granted to Simon Fraser University the right to lend this thesis, project or extended essay to users of the Simon Fraser University Library, and to make partial or single copies only for such users or in response to a request from the library of any other university, or other educational institution, on its own behalf or for one of its users.

The author has further granted permission to Simon Fraser University to keep or make a digital copy for use in its circulating collection (currently available to the public at the "Institutional Repository" link of the SFU Library website <www.lib.sfu.ca> at: <http://ir.lib.sfu.ca/handle/1892/112>) and, without changing the content, to translate the thesis/project or extended essays, if technically possible, to any medium or format for the purpose of preservation of the digital work.

The author has further agreed that permission for multiple copying of this work for scholarly purposes may be granted by either the author or the Dean of Graduate Studies.

It is understood that copying or publication of this work for financial gain shall not be allowed without the author's written permission.

Permission for public performance, or limited permission for private scholarly use, of any multimedia materials forming part of this work, may have been granted by the author. This information may be found on the separately catalogued multimedia material and in the signed Partial Copyright Licence.

The original Partial Copyright Licence attesting to these terms, and signed by this author, may be found in the original bound copy of this work, retained in the Simon Fraser University Archive.

Simon Fraser University Library
Burnaby, BC, Canada

Revised: Fall 2006

Abstract

Litre-quantities of nuclear-spin polarized gas can be subjected to magnetic resonance imaging (MRI) techniques to obtain information on the lung morphology and to perform regionally specific measurements of lung function. This thesis characterizes and provides protocols for operating a system that produces nuclear-spin polarized ^{3}He by metastability exchange optical pumping (MEOP) of a continuous stream of gas. Optical monitoring of the ^{3}He emission spectrum and polarization are used to aid in the efficient production of highly non-equilibrium nuclear-spin polarized (hyperpolarized) ^{3}He. Preliminary measurements of the total magnetic moment and longitudinal relaxation time were made on the first samples of compressed, hyperpolarized ^{3}He. The results suggest that the continuous-flow MEOP system is fully functional but requires several minor procedural and design modifications before samples of hyperpolarized ^{3}He gas can be produced with magnetic moments suitable for lung airspace MRI.

Keywords: Hyperpolarized; Helium-3; MRI; Metastability Exchange Optical Pumping

This thesis is dedicated to my mom and my brother.
Their support and encouragement has given me confidence in
myself and in my abilities.

Acknowledgments

The work that is presented in this thesis has been made possible because of the various contributions made by the Canadian governement, various educators, colleagues, peers and my friends and familiy.

The Candian government, namely the Natural Science and Engineering Research Council (NSERC), lifted much of the financial burden of obtaining a post-secondary education by providing outstanding funding during my undergraduate and graduate studies. The two summer research assistant positions that I acquired with the help of NSERC grants enriched my education with valuable laboratory skills and experience. The very generous financial support NSERC awarded me throughout my graduate studies allowed me to focus on my research and meet my educational goals in a timely fashion.

There have been numerous educators that have offered me exceptional encouragement and support in addition to teaching me the tools I would need for academic success. I was fortunate to have several very dedicated senior science and math teachers in high school, Mr. McLeod, Mr. Hill, Mrs. Fuller and Mr. Abra, whose compassion for educating helped to prepare me for my university career. Dr. David Hanna, my undergraduate supervisor and Dr. Mike Hayden, my graduate supervisor, have both invested a lot of time into developing my understanding in the realm of experimental physics. It was Dr. Mike Hayden's enthusiasm and outright passion for understanding the underlying physics of our surroundings that sparked my interest in physics in my first year of university and that continued to inspire me throughout my graduate studies. Dr. Elana Brief has been a invaluable mentor since I met her four years ago. She has helped me turn countless lack-luster presentations and cover letters into stimulating and effective forms of communication.

My friends and family have offered me more than their support and encouragement, as they have also been very valuable resources over the last few years. It was my mother's, Terrill Welch, feminist believe-system and problem-solving approach that indirectly encouraged me to pursue an education in science. She has always been there to lift my spirits and to celebrate my successes, even if it had to be via telephone or email. My brother, Kris Welch, encouraged me with his unquestionable belief that I was capable of any task I took on. My friends have enriched my life with laughter and good times.

I was very happy to work in a laboratory alongside four very dynamic individuals. Dr. Chris Bidinosti shared his expertise in the field and guided me in my studies. His curiosity and genuine interest in his research combined with his thorough and systematic approach to problems are the truly admirable qualities. Erin Chapple has been a great friend and companion to who helped me maintain a general sense of well-being. Jason Hobson helped me deal with some difficult circumstances by offering his insight and words of encouragement. Geoff Archibald helped to improve my understanding of countless pieces of equipment and physical concepts by very patiently answering my seemingly endless questions.

I have been very fortunate to have such talented and charismatic friends, family members and colleagues. All of you have influenced my work, my education and my character and as a result have helped me to complete this degree. I extend my thanks to each and every one of you.

Contents

Approval ii

Abstract iii

Dedication iv

Acknowledgments v

Contents vii

List of Figures ix

1 Introduction 1

2 Theory 5

2.1 ^{3}He and Nuclear Magnetic Resonance Imaging 5

2.2 The ^{3}He Energy Spectrum 6

2.3 Metastability Exchange Optical Pumping (MEOP) 14

2.4 Nuclear Magnetic Resonance 18

2.4.1 The NMR Signal 24

2.5 Hyperpolarized ^{3}He NMR 26

2.5.1 Relaxation 28

3 Metastability Exchange Optical Pumping Station 34

3.1 The Homogeneous Magnetic Field 34

3.2 The Magnetic Field Gradient Coils 35

3.3 The Stainless Steel Section of the Gas Manifold 38
3.4 The Borosilicate Section of the Gas Manifold 39
3.5 The Compressor 41
3.6 Summary 42

4 Optical Pumping Cell and Laser Optics **45**
4.1 The Optical Pumping Cell and the Discharge Coil 45
4.2 The Laser and the Laser Optics 47

5 Ancillary Equipment **51**
5.1 The Spectrometer 51
5.2 The Polarimeter 57
5.3 The NMR System 63
5.4 The Imaging Magnet 70

6 Continuous-Flow Optical Pumping Procedure **72**
6.1 Step-by-Step Procedure 72
6.2 Detailed Procedure 74

7 Preliminary Measurements and System Assessment **83**
7.1 Total Magnetic Moment Measurement 83
7.2 T_1 Measurement 87
7.3 Necessary System Improvements 89

A Cell Specifications **92**

Bibliography **93**

List of Figures

2.1 The energy-level structure of helium. 9

2.2 The energy-level structure of helium when the effects of fine and hyperfine coupling are included. 11

2.3 A flow-chart for MEOP. 15

2.4 The ^{3}He energy transitions during MEOP. 16

2.5 The MEOP transitions $C_1 - C_9$. 17

2.6 The precession of a magnetic moment $\boldsymbol{\mu}$ about $\mathbf{B}_0$. 19

2.7 The rotating frame (with angular frequency ω) and the laboratory frame. . . 22

2.8 A precessing magnetization induces an emf across a receive coil 24

2.9 The degeneracy in ground state ^{3}He atoms is lifted in non-zero magnetic fields. 27

3.1 A schematic diagram showing the layout of the MEOP station. 35

3.2 The relative positions of the magnetic field coils, the storage and optical pumping cells. 36

3.3 The z-gradient coils. 37

3.4 The saddle coil geometry used for the y-gradient coils. 37

3.5 The front panel of the stainless steel section of the gas manifold. 39

3.6 A detailed schematic of the glassware of the MEOP station gas manifold. . 40

3.7 A schematic diagram of the compressor. 41

3.8 The non-magnetic bearings of the compressor. 43

3.9 The gas flow path through the glassware section of the gas-handling manifold. 44

4.1 A photograph of the optical pumping cell. 46

4.2 The RF resonant circuit used to ignite and maintain the discharge in the OPC. 47
4.3 The optical components coupled to the laser. 48
4.4 The intensity of the ^{3}He discharge as a function of the laser piezovoltage. . 50

5.1 The MEOP station and ancillary equipment. 52
5.2 The optical emission spectrum from a helium discharge. 52
5.3 The optical emission spectrum for helium at two different pressures. 53
5.4 The optical emission spectrum when there is a small amount of air present. 54
5.5 The optical emission spectrum when Masterflex C tubing impurites have contaminated the gas. 55
5.6 The optical emission spectrum before and after one cleaning iteration. . . . 56
5.7 The energy transition corresponding to the 668 nm emission. 58
5.8 The nuclear-spin polarization from the optical polarization of the 668 nm ^{3}He emission line. 59
5.9 The polarimeter collects 668 nm light close to the quantization axis. 60
5.10 The optical components of each polarimeter lens tube. 61
5.11 The $\sin\phi$ distribution of the B_1 coil used in the MEOP station NMR system. 64
5.12 A photograph of the B_1 and receive coils. 65
5.13 The relative magnetic field strength of $\mathbf{B}_1$. 66
5.14 The four NMR receive coils and their orientation relative to $\mathbf{B}_1$. 67
5.15 The four NMR receive coils. 68
5.16 The quadrature detection NMR system used in the MEOP station. 69
5.17 An NMR signal recorded by the MEOP Station NMR system. 70
5.18 Schematic diagram of the imaging magnet NMR system 71

6.1 MEOP station glassware to be used in accordance with the procedure. . . . 73
6.2 The ^{3}He optical emission spectrum before and after a continuous-flow MEOP operation. 80
6.3 An NMR signal acquired in the MEOP station from ^{3}He in the storage cell. 81
6.4 An NMR signal acquired after the NMR signal shown in Fig. 6.3. 82

7.1 An NMR signal acquired in the imaging magnet. 86
7.2 The NMR signal amplitude resulting from a small tipping pulse α. 88

7.3 The NMR signal amplitude is plotted as a function of the time. 89

Chapter 1

Introduction

Magnetic resonance imaging (MRI) was first accomplished over thirty years ago [1]. Since then, dramatic improvements in system hardware and imaging techniques have enabled routine collection of high resolution morphological and functional images of most human organs. Despite these successes, the lungs have proven to be difficult to image using conventional (i.e. ^{1}H) MR techniques. This is due, in part, to the difference in the magnetic susceptibility of lung tissue and air which results in large local gradients at the alveolar wall that act to reduce the duration of the NMR signal to milliseconds at conventional MRI field strengths [2, 3]. In addition the lungs have a very low proton density which limits the signal strength. The combined effect of these two factors makes ^{1}H MRI of the lung tissue challenging [4].

Over the last decade, several research groups have taken an entirely different approach to lung MRI. Rather than imaging the lung tissue, MR techniques are applied to gas within the lung to obtain images of the airspace. During this imaging modality, nuclear-spin polarized ^{129}Xe or ^{3}He is inhaled and acts as a contrast agent in the ventilated regions of the lungs. The nuclear-spin polarization is produced using optical pumping techniques which give rise to a highly non-equilibrium polarization (hyperpolarization) that is independent of field strength. This is quite unlike ^{1}H MRI where the nuclear-spin polarization is an equilibrium (Boltzmann) polarization and is proportional to the strength of the static magnetic field provided by the MR scanner. Several research groups have exploited the fact that the degree of polarization in the hyperpolarized gas is independent of field strength and have conducted this imaging modality at low ($\sim$3 mT) field strengths to complement those conducted at high ($\geq$ 1 T) field strengths [5–10].

One method to produce hyperpolarized ^{3}He is metastability exchange optical pumping (MEOP), which was first developed during the 1960s. MEOP is conducted in pure ^{3}He gas at low-pressure (1-10 Torr), and indirectly produces large nuclear-spin polarizations through optical pumping of one of the excited helium states. This method has been used to produce nuclear-spin polarizations as high as 80-90 %, which is roughly six orders of magnitude larger than the Boltzmann polarization the gas would have at room temperature in a 1 T magnetic field [11].

In order to be suitable for lung airspace MRI, dense samples (i.e. at atmospheric pressure) of hyperpolarized ^{3}He are required [12]. This can be accomplished by optically pumping a continuous stream of ^{3}He and subsequently compressing it. There are about 5 to 10 of these 'continuous-flow' systems worldwide and although the exact design varies from one implementation to another, there are several components that are common amongst all of them. First of all, there needs to be a container (a cell) in which MEOP is actually conducted. This is usually referred to as the optical pumping cell. This cell is equipped with electrodes that are used ignite a discharge in the ^{3}He gas and thereby populates excited states. These excited states are then optically pumped using a 1083 nm light source which can be either linearly or circularly polarized [13, 14]. The light must be polarized because optical pumping relies on a transfer of angular momentum from light to atomic states. The quantization axis for the two angular momenta is defined using a homogeneous magnetic field which is made to be colinear with the direction of propagation of the 1083 nm light. Finally, once the gas has been hyperpolarized, a pump is used to compress it into a second container where the gas is stored until it is required for MR experiments.

Over the last 40 years, substantial improvements to the lifetime and the maximum polarization of ^{3}He that can be achieved have been made through advancements in the components used for the MOEP process. One of the major developments was that of high-power (up to 10 W) infrared fiber lasers, now commercially available, which have replaced the ^{4}He arc-lamps that were originally used for optical pumping [11, 12, 15–17]. Some groups have increased the photon efficiency by using very long optical pumping cells (up to 2.4 m) and using mirrors to reflect the 1083 nm light back through the cell volume [11, 17–21]. The mechanical pump that is used to compress the gas is usually custom-built because it must be made entirely of non-magnetic materials in order to minimize polarization losses [12, 22, 23]. Storage cells fabricated out of aluminosilicate glass lined with a thin metallic coating (usually cesium, bismuth or rubidium) have been used to give lifetimes over a hundred hours [24–26]. However, because it is easier for glass-blowers to work with, borosilicate glass (such as Corning's Pyrex © or Schott's Duran©) is often used instead of aluminosilicate glass despite an order of magnitude decrease in polarization lifetime [24, 26]. Once a sufficiently spin-dense sample of hyperpolarized ^{3}He has been collected in the storage cell, it can be transferred to a inert plastic (Tedlar ©) bag and topped up with a buffer gas such as N_2 or ^{4}He before it is transported to another location and used for lung airspace MRI [6, 17].

In this thesis, I document the commissioning and characterization of a continuous-flow MEOP system. The design of this system is loosely based on the continuous-flow system at the École Normale Superière (Paris) by P.J. Nacher and G. Tastevin. The design is such that polarization efficiency is somewhat sacrificed for design simplicity, ease of operation and overall cost. My contributions to the development of the new MEOP system can be divided into two categories. First of all, I was responsible for developing and conducting tests to characterize the performance of each element of the polarization apparatus. I began with a nearly assembled and completely untested apparatus and finished by demonstrating that I could produce nuclear-spin polarized ^{3}He gas with adequate quantities of nuclear magnetization. Along the way I implemented a number of significant modifications to the system and developed a comprehensive protocol for its operation. Second, and perhaps more important in the long term, I developed a number of diagnostic devices (collectively referred to as the ancillary equipment) and protocols that ultimately played a crucial role in enhancing the reliability of the MEOP system. Together, these contributions provide a solid foundation upon which future modifications and procedures can be based.

The remainder of this thesis is structured as follows. Chapter 2 describes some of the underlying physical principles that pertain to the work presented in later chapters. Chapter 3 describes the design of the optical pumping station. In Chapter 4, the section of the apparatus directly involved in the optical pumping process is introduced and characterized. Chapter 5 presents the architecture and implementation of ancillary equipment used in the MEOP process. Chapter 6 outlines a step-by-step procedure for the collection of hyperpolarized ^{3}He using the MEOP apparatus described in Chapters 3-5. Finally, Chapter 7 presents preliminary NMR experiments conducted on some of the first nuclear-spin polarized ^{3}He samples collected with the MEOP station. The results of these experiments are used to characterize the performance of the MEOP system and to show that with only minor modifications, this apparatus should be able to produce hyperpolarized gas in quantities suitable for MR imaging of human lungs.

Chapter 2

Theory

This chapter describes the physics underlying metastability exchange optical pumping (MEOP) and nuclear magnetic resonance (NMR) of hyperpolarized gas. It is organized so as to first introduce nuclear-spin hyperpolarization of ^{3}He gas, then to describe hyperpolarized gas NMR and finally to outline some of the factors that can destroy the nuclear-spin hyperpolarization. The first section includes a description of the energy-level structure of the ground and first-excited states of ^{3}He. The ^{3}He energy-level structure is then used to assist in an explanation of metastability exchange optical pumping. A classical description of NMR is then presented and is extended to cover topics relevant to hyperpolarized ^{3}He NMR in the subsequent sections. This is followed by an outline of several nuclear-spin relaxation mechanisms that can destroy the polarization of the gas.

2.1 ^{3}He and Nuclear Magnetic Resonance Imaging

Helium-3 (^{3}He) is one of the two stable isotopes of helium. The ^{3}He nucleus comprises two protons and one neutron - only one neutron shy of the more abundant ^{4}He isotope. Because of the odd number of nucleons, the ^{3}He nucleus has a non-zero spin making it suitable for NMR experiments. In addition, ^{3}He is also suitable for magnetic resonance imaging (MRI) of human lung airspaces because it is inert, stable and lipid insoluble (it will not diffuse into the bloodstream) [10].

Hyperpolarized gas is often used for gas NMR instead of equilibrium (Boltzmann) polarized gas because the significant increase in nuclear magnetization makes it much simpler to perform NMR experiments. For example, optical pumping techniques have been used to routinely produce magnetizations five orders of magnitude larger than those corresponding the Boltzmann polarization of the gas at room temperature in a 1 T magnetic field [5]. There are two optical pumping methods that can be used to produce hyperpolarized ^{3}He. The method described in this thesis is metastability exchange optical pumping (MEOP). In MEOP, nuclear-spin polarization is indirectly created in an ensemble of ground state ^{3}He atoms at low pressure by optically pumping the electron spin-states of excited ^{3}He atoms. The second method, spin exchange optical pumping (SEOP), can be performed at higher pressures (up to 10 atm) and makes use of an intermediate atom, such as rubidium, to polarize the ^{3}He spins [10]. In both methods, the electron-spin polarization and subsequent nuclear-spin polarization, results from a transfer of spin angular momentum from light to atomic energy eigenstates. MEOP was chosen as the optical pumping method for this apparatus because it has a high photon effieciency (of order 0.1-0.5) and can produce large polarizations in pure ^{3}He at room temperature in tens of seconds [10, 15].

In MEOP the atomic-spin states of excited ^{3}He are optically pumped. Knowledge of the fine and hyperfine structure of the first excited states of the ^{3}He atom is necessary to discuss MEOP in detail. Thus, a discussion of the ^{3}He energy-level structure precedes a thorough description of MEOP.

2.2 The ^{3}He Energy Spectrum

The basic energy spectrum of helium is the same for both ^{4}He and ^{3}He, and can be derived by considering the Coulomb interactions between the two electrons and between the electrons and protons in the nucleus. The helium energy spectrum is constructed from the energy eigenstates the Hamiltonian of the helium atom. The general expression for the Schrödinger equation is [27]

$$\frac{\hbar}{2\mu}\nabla^2\Psi(\mathbf{r}) + V(r)\Psi(\mathbf{r}) = E\,\Psi(\mathbf{r}) \ , \tag{2.1}$$

where $\hbar$ is Planck's constant h divided by 2π, μ is the reduced mass ($\mu = \frac{m_e m_n}{m_e + m_n}$) and $\Psi(\mathbf{r})$ is the Schrödinger wave function for an electron at position $\mathbf{r}$. The position vectors that point from the nucleus to the two electrons are $\mathbf{r_1}$ and $\mathbf{r_2}$, and thus $|\mathbf{r_1} - \mathbf{r_2}|$ is the distance between the two electrons. E is the energy, Z is the number of protons in the nucleus, e is the electron charge, m_e is the electron mass, m_n is the mass of the nucleus and ε_o is the permittivity of free space. For helium, the potential $V(r)$ includes the proton-electron attraction terms (one for each electron) and the electron-electron repulsion term:

$$V(r) = -\frac{Ze^2}{4\pi\varepsilon_o r_1} - \frac{Ze^2}{4\pi\varepsilon_o r_2} + \frac{e^2}{4\pi\varepsilon_o|\mathbf{r_1}-\mathbf{r_2}|} \; . \tag{2.2}$$

A brief outline of the solution to the Schrödinger equation for a helium atom is described here. A more detailed solution can be found in most introductory-level quantum mechanics textbooks. This discussion of the helium atom energy-level structure follows the explanation given in *Modern Physics* by Bernstein [27].

The form of the potential $V(r)$ for helium makes the solving the Schrödinger equation directly somewhat complicated. One approach to simplifying the solution is to ignore the two Coulomb interactions that result from the presence of the second electron. That is, the Coulomb attraction between the second electron and the nucleus and Coulomb repulsion between the two electrons. The resulting potential has the same form as the potential corresponding to a hydrogen atom with the only difference being the number of protons in the expression. Consequently, the solution of the wave function for helium can be derived in exactly the same fashion as the wave function for hydrogen. The standard method for solving Eq. 2.1 is by separation of variables, where $\Psi(\mathbf{r})$ is written as a product of a radial wave function $R(r)$ and an angular wave function $Y(\theta,\phi)$:

$$\Psi(\mathbf{r}) = R(r)Y(\theta,\phi) \; . \tag{2.3}$$

By substitution of Eq. 2.3 into Eq. 2.1, the radial and angular parts of the of the Schrödinger equation can be separated. The radial part of the Schrödinger equation is

$$\frac{\hbar}{2\mu}\nabla^2 R(r) + V(r)R(r) = ER(r) \; . \tag{2.4}$$

The solution to the radial part of the Schrödinger equation is an eigenfunction of the energy E with eigenvalues

$$E = -\frac{1}{2}\mu\left(\frac{Ze^2}{4\pi\varepsilon_o\hbar}\right)^2 \frac{1}{(n_r+\ell+1)^2} \; . \tag{2.5}$$

where n_r is the radial quantum number and ℓ is the angular-momentum quantum number, which will be discussed shortly. The principal quantum number, $n = n_r + \ell + 1$, is conventionally used to specify atomic energy levels.

The angular part of the Schrodinger equation is given by

$$\left(\frac{\partial^2}{\partial\theta^2} + \cot\theta + \frac{1}{\sin^2\theta}\frac{\partial^2}{\partial\phi^2}\right) Y(\theta,\phi) = \ell(\ell+1) Y(\theta,\phi) \ . \tag{2.6}$$

where the term in parentheses on the left hand side of Eq. 2.6 is the square of the angular momentum $\mathbf{L}$ expressed in spherical coordinates. Thus, the total angular wavefunction $Y(\theta,\phi)$ is an eigenfunction of $\mathbf{L}^2$ which has integer eigenvalues $\ell(\ell+1)$. The allowed values for the angular momentum quantum number ℓ are limited to integers less than $n-1$. That is

$$\ell \leq n-1 \text{ where } n \geq 1 \ . \tag{2.7}$$

By treating $Y(\theta,\phi)$ itself as a product of two wavefunctions, namely $\Phi(\phi)$ and $F(\theta)$, it can further be shown that $\Phi(\phi)$ is an eigenfunction of the z-component of the angular momentum $L_z = -i\hbar\partial/\partial\phi$, written appropriately in spherical coordinates. The eigenvalues of L_z are characterized by an integer m_ℓ which is bounded such that

$$m_\ell = -\ell, -\ell+1, \ldots \ell-1, \ell \ . \tag{2.8}$$

In summary, for a given energy level defined by the principal quantum number n, there are n degenerate states resulting from ℓ-degeneracy and an additional $2(\ell+1)$ degenerate states for each value of ℓ resulting from m_ℓ-degeneracy.

The energy eigenvalues of Eq. 2.5 are only correct for hydrogen-like atoms, where the electron in question only experiences a Coulomb attraction to the nucleus of charge Ze. The energy eigenvalues for helium are modified slightly from those of hydrogen-like atoms because of the Coulomb repulsion between the two electrons that must be included in the potential of the Hamiltonian. One method to account for the Coulomb repulsion, without having to add an extra term to the potential in the Hamiltonian, is to assume that the nucleus has an effective charge Z^*e that is smaller than the actual charge Ze. This reduced nuclear charge can be thought of being due to screening of the nucleus by the second electron. The smaller nuclear charge results in a reduction in Coulomb attraction. Both Z^*e and the

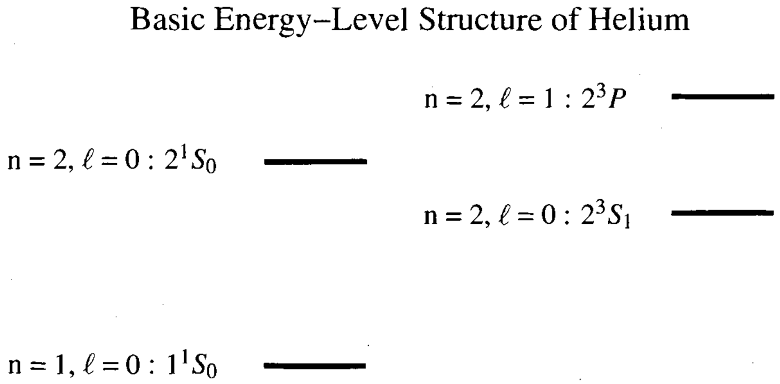

Figure 2.1: The basic structure of the ground and first excited states of helium. The notation used here will be explained in detail over the next several pages.

Coulomb attraction will then decrease with increasing electron orbital angular momentum, and hence with increasing ℓ. Therefore, by use of an effective nuclear-charge, the energy eigenvalues reveal an ℓ-dependence such that the the electron is less-tightly bound for increasing ℓ-values. Figure 2.1 summarizes the basic energy-level spectrum for the ground and first excited-states of the helium atom.

The discussion thus far has not led to a distinction between the ^{4}He and ^{3}He energy-level structure. Both ^{4}He and ^{3}He have further splittings in their energy spectra that come from the fine-structure interactions between the spin and orbital angular momenta of the electrons. Of interest here is the energy spectrum of the first excited states of ^{3}He, which exhibits even more energy-level splitting due to hyperfine structure that results from its non-zero nuclear-spin angular momentum interacting with the total electron angular momentum. The fine and hyperfine structure of the ^{3}He energy spectrum are of utmost importance in MEOP applications because these states are individually manipulated by the 1083 nm polarized optical pumping light.

The fine structure of the helium atom is a result of spin-orbit coupling, where the total electron-spin angular momentum interacts with the excited electron's orbital angular momentum, $\mathbf{L}$. The total electron-spin angular momentum ($\mathbf{S} = \mathbf{S}_1 + \mathbf{S}_2$) is the sum of the angular momentum of the two electrons $\mathbf{S}_1$ and $\mathbf{S}_2$. In the excited electron's rest frame, the electron sees a magnetic dipole resulting from the orbiting, positively-charged nucleus. The interaction of the magnetic moments gives rise to a potential energy $U_{spin-orbit}$ that is proportional to the scalar product of its spin and orbital angular momentum

$$U_{spin-orbit} \propto \mathbf{L} \cdot \mathbf{S} \ . \tag{2.9}$$

The eigenvalues of the operator $\mathbf{L} \cdot \mathbf{S}$ are not obvious when the operator is expressed in this form and the total angular momentum vector $\mathbf{J} = \mathbf{L} + \mathbf{S}$ is useful in this case. The operator $\mathbf{L} \cdot \mathbf{S}$ can be written as a function of $\mathbf{J}^2$ since $\mathbf{J}^2 = \mathbf{L}^2 + \mathbf{S}^2 + 2\mathbf{L} \cdot \mathbf{S}$. This expression is useful because it allows $\mathbf{L} \cdot \mathbf{S}$ to be written in terms of operators with known eigenvalues and then be substituted into Eq. 2.9 to give

$$U_{spin-orbit} \propto \mathbf{J}^2 - \mathbf{L}^2 - \mathbf{S}^2 \ . \tag{2.10}$$

The eigenvalues of the total electron spin $\mathbf{S}$ are $s = 0$ when the electron spins are antiparallel (a singlet state: $\frac{1}{\sqrt{2}}(\uparrow\downarrow - \downarrow\uparrow)$) and $s = 1$ when the electrons are parallel (a triplet state as the electron spins can be: $\uparrow\uparrow, \downarrow\downarrow, \frac{1}{\sqrt{2}}(\uparrow\downarrow + \downarrow\uparrow)$). The eigenvalues of $\mathbf{J}^2$ are $j_\pm(j_\pm + 1)$ when the orbital angular momentum and spin angular momentum are parallel (j_+) and antiparallel (j_-). The total angular momentum eigenvalues $j_\pm$ are determined by the angular momentum eigenvalue ℓ and the total electron spin eigenvalue s:

$$j_+ = \ell + s \qquad \mathbf{L} \text{ and } \mathbf{S} \text{ parallel} \tag{2.11}$$

$$j_- = \ell - s \qquad \mathbf{L} \text{ and } \mathbf{S} \text{ anti-parallel} \ . \tag{2.12}$$

The energy shift resulting from spin-orbit coupling will be proportional to the eigenvalues of the operator in Eq. 2.10:

$$U_{spin-orbit} \propto j_\pm(j_\pm + 1) - \ell(\ell + 1) - s(s + 1) \ . \tag{2.13}$$

With the inclusion of spin-orbit coupling, the energy levels of the helium atom become functions of the principal quantum number n, the angular momentum quantum number ℓ, and the spin angular momentum quantum number s. Equation 2.13 reveals that the inclusion of fine coupling in the energy eigenvalues removes the degeneracy of the triplet and singlet spin states ($s = 1$ and $s = 0$). Because spin-orbit coupling requires non-zero spin and orbital angular momentum, fine structure will be exhibited for all spin triplet states in

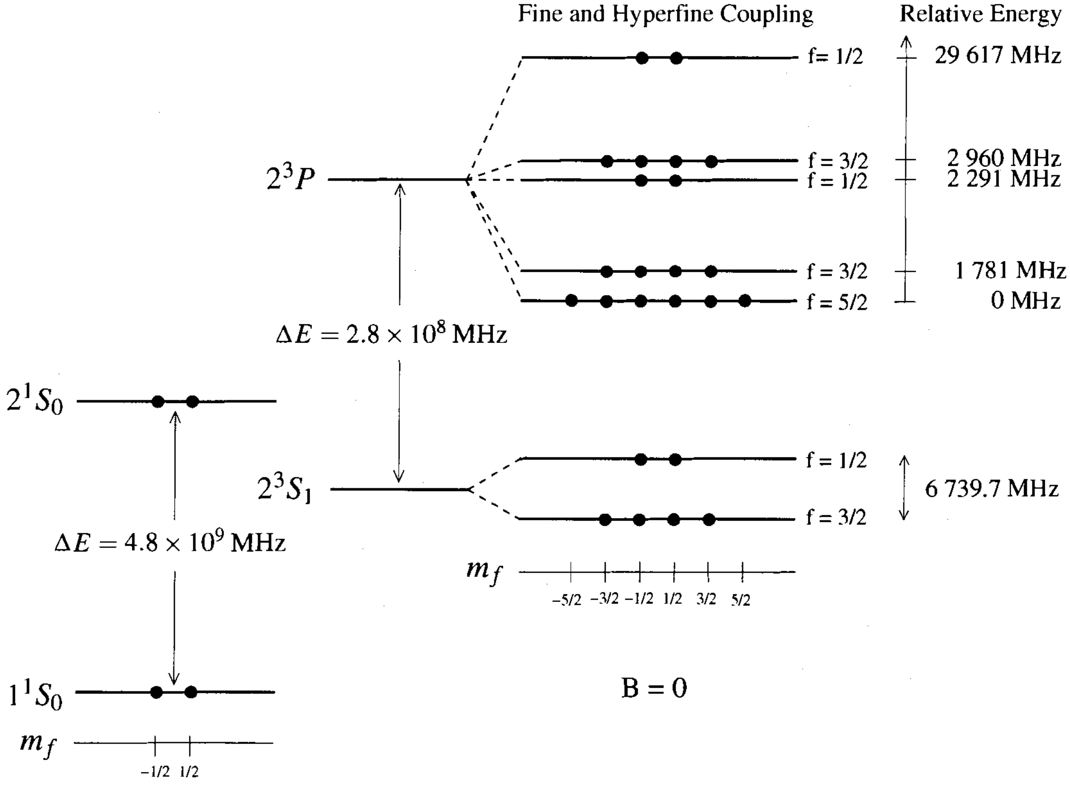

Figure 2.2: The effects of fine and hyperfine coupling on the energy-level structure of the ground and first excited states of ^{3}He in zero magnetic field. The degenerate magnetic sublevels are indicated by solid circles and have eigenvalues ranging from $m_f = -\frac{5}{2}$ to $+\frac{5}{2}$. The energy-level spacings are not drawn to scale, but are specified in frequency units [14].

energy levels having $\ell > 0$. The energy shifts in the 2^3P states of Helium resulting from spin-orbit coupling are of order a few GHz (see Figure 2.2).

Spin-orbit coupling does not fully explain the energy level structure observed in ^{3}He. This is because the nuclear-spin of ^{3}He gives rise to hyperfine structure in some of the energy levels, an effect that is absent in the case of the spin-zero ^{4}He isotope. The nuclear-spin $\mathbf{I}$ of ^{3}He interacts with the total electron angular momentum ($\mathbf{J} = \mathbf{S}_1 + \mathbf{S}_2 + \mathbf{L}$) giving rise to the hyperfine structure of the ^{3}He energy-levels. The energy associated with the hyperfine interaction is directly proportional to the scalar product of the two angular momenta:

$$U_{hyperfine} \propto \mathbf{J} \cdot \mathbf{I} \tag{2.14}$$

Again, it is useful to write the scalar product of the energy in terms of the square of the atom's total angular momentum, **F**, where $\mathbf{F} = \mathbf{J} + \mathbf{I}$. That is,

$$U_{hyperfine} \propto \mathbf{F}^2 - \mathbf{J}^2 - \mathbf{I}^2 \ . \tag{2.15}$$

Similar to the previous discussion for **J** in $U_{spin-orbit}$, the eigenvalues of $\mathbf{F}^2$ can be either $f_\pm\,(f_\pm + 1)$ depending on whether the electron and nuclear spin angular momenta are parallel (f_+) or antiparallel (f_-). The atom's total angular momentum eigenvalues $f_\pm$ are determined by the total electron angular momentum eigenvalues $j_\pm$ and the nuclear spin eigenvalue $i = \frac{1}{2}$ as follows:

$$f_+ = j_\pm + i \qquad \mathbf{J} \text{ and } \mathbf{I} \text{ parallel} \tag{2.16}$$

$$f_+ = j_\pm - i \qquad \mathbf{J} \text{ and } \mathbf{I} \text{ anti-parallel} \ , \tag{2.17}$$

where $j_\pm$ is determined by the relative alignment of the electron spin and orbital angular momentum as discussed previously in the context of fine structure. $U_{hyperfine}$ can thus be written in terms of the angular momentum eigenvalues as follows:

$$U_{hyperfine} \propto f_\pm(f_\pm + 1) - j(j+1) - i(i+1) \ . \tag{2.18}$$

It will be useful to go through several of the energy level splittings to better understand the hyperfine structure of ^{3}He summarized in Fig. 2.2.

In the ground state the two electrons will be in the spin-singlet state (see bottom left of Fig. 2.2), as required by the Pauli exclusion principle, and will have total spin angular momentum, $s = 0$. This is denoted as the 1^1S_0 state, where the leading 1 indicates the value of the principal quantum number, the superscript 1 indicates the electron-spin singlet state ($s = 0$), S represents the fact that $\ell = 0$ and finally the subscript indicates that the total electron-angular momentum $j = 0$. There is no fine structure in the 1^1S_0 state because both the electron spin and orbital angular momentum are zero. The hyperfine structure is also absent in the 1^1S_0 state because the total angular momentum of the electrons is zero (ie. $j = \ell + s = 0 + 0 = 0$). In addition, since there is no electron angular momentum, the consideration of parallel and antiparallel **J** and **I** is not relevant. The atom's total angular momentum is $\frac{1}{2}$ since $f = j + i = 0 + \frac{1}{2} = \frac{1}{2}$, and thus there are two degenerate eigenstates in the ground state that correspond to $m_f = \pm\frac{1}{2}$. The m_f states are indicated by solid circles in Fig. 2.2.

In the first excited state, $n = 2$ and, from Eq. 2.7, ℓ can be 0 or 1. Now that one electron is in an excited state, the total electron-spin quantum number s can be either 1 or 0. When $\ell = 0$ and $s = 0$ the atom is in the 2^1S_0 state. The total electron angular momentum is zero ($j = 0 + 0 = 0$) and hence there is no fine or hyperfine coupling. The atom's total angular momentum is $\frac{1}{2}$ (ie. $f = j + i = 0 + \frac{1}{2} = \frac{1}{2}$) and this state also has a two-fold degeneracy resulting from the two eigenstates $m_f = \pm\frac{1}{2}$.

When $\ell = 0$ but the electrons are in the spin-triplet state ($s = 1$), the total electron angular momentum is $j = 0 + 1 = 1$ and the atom is in the 2^3S_1 state. There is still no fine structure, but with $j \neq 0$, the hyperfine coupling removes some of the degeneracy of the energy eigenstates. If $\mathbf{J}$ and $\mathbf{I}$ are parallel, then f_+ must be used which is $\frac{3}{2}$ in the 2^3S_1 state ($f_+ = 1 + \frac{1}{2} = \frac{3}{2}$). If $\mathbf{J}$ and $\mathbf{I}$ are antiparallel, then f_- must be used which is $\frac{1}{2}$ for the 2^3S_1 state ($f_- = 1 - \frac{1}{2} = \frac{1}{2}$). The hyperfine coupling gives rise to two different energy eigenstates that depend on the relative alignment of the total electron and nuclear spin angular momentum. Even after the hyperfine coupling is included in the energy-level structure, there is still degeneracy in these energy-levels. For example the 2^3S_1 state has a four-fold degeneracy when $f = 3/2$ ($m_f = -\frac{3}{2}, -\frac{1}{2}, \frac{1}{2}, \frac{3}{2}$) and a two-fold degeneracy when $f = \frac{1}{2}$ ($m_f = -\frac{1}{2}, \frac{1}{2}$).

The energy levels get really interesting in the electron spin-triplet states (2^3P) when $\ell = 1$ and $s = 1$, because both fine and hyperfine structures are present. Spin-orbit coupling splits the 2^3P states into two separate states since j is $j_+ = 1 + 1 = 2$ for $\mathbf{L}$ parallel to $\mathbf{S}$ and $j_- = 1 - 1 = 0$ for $\mathbf{L}$ antiparallel to $\mathbf{S}$. Hyperfine coupling further splits the energy levels for non-zero values of j. First consider the case when $\mathbf{L}$ and $\mathbf{S}$ are parallel and j is 2 ($j_+ = s + \ell = 1 + 1 = 2$) which corresponds to the 2^3P_2 state. Again, f can assume one of two values: $f_+ = j_+ + i = 2 + \frac{1}{2} = \frac{5}{2}$ or $f_- = j_+ - i = 2 - \frac{1}{2} = \frac{3}{2}$. The energy eigenstate $f_+ = \frac{5}{2}$ has a six-fold degeneracy ($m_f = -\frac{5}{2}, -\frac{3}{2}, -\frac{1}{2}, \frac{1}{2}, \frac{3}{2}, \frac{5}{2}$) and the energy eigenstate $f_- = \frac{3}{2}$ has a four-fold degeneracy ($m_f = -\frac{3}{2}, -\frac{1}{2}, \frac{1}{2}, \frac{3}{2}$). In the 2^3P_1 state, $j = 1$ and f can be either $\frac{3}{2}$ or $\frac{1}{2}$. Finally, in the 2^3P_0 state $j = 0$ and there is no hyperfine splitting of this energy level, however there is still a two-fold degeneracy in this state since $f = j + i = 0 + \frac{1}{2} = \frac{1}{2}$, and $m_f = -\frac{1}{2}, \frac{1}{2}$.

2.3 Metastability Exchange Optical Pumping (MEOP)

Metastability exchange optical pumping (MEOP) can be used to produce a large non- equilibrium nuclear-spin polarizations in an ensemble of ground-state ^{3}He atoms. MEOP is conducted in ^{3}He at low pressures (1-10 Torr) in a homogeneous magnetic field [28]. The magnetic field strength need not be large, even the Earth's magnetic field is strength is sufficient at a mere 0.5 mT, and its direction is used to define the quantization axis. Because MEOP involves the transfer of angular momentum from light to electrons, the direction of propagation of the optical pumping light must lie along the quantization axis and hence be colinear with the magnetic field [16]. A flow-chart for MEOP has been included (see Fig. 2.3) and will be used to aid in the following discussion.

The nuclear-spin polarization of an ensemble of ^{3}He atoms is achieved indirectly by optically pumping the $2^3S_1 \rightarrow 2^3P$ transition. An RF discharge is ignited in the gas to populate the long-lived (metastable) 2^3S_1 state, as indicated in Fig. 2.4 and by step 1 in Fig. 2.3. Once the 2^3S_1 state has been populated, circularly polarized 1083 nm light can be used to optically pump any of the 22 allowed $2^3S_1 \rightarrow 2^3P$ transitions [14]. By optically pumping with right circularly polarized light the change in the quantum number m_f is restricted to be +1. The various transitions are distinguished by the change in energy and can be divided into nine groups: $C_1 \rightarrow C_9$, where C_1 is the lowest energy transition and C_9 is the highest energy transition (see Fig. 2.5). Because of the degeneracy in f, there may be more than one transition for a given C_i. However, for right circularly polarized light there is only one transition that corresponds to the energy change of C_8 (the transition that is optically pumped in the experiments described in this thesis). C_8 is exclusively the transition from $m_f = -\frac{1}{2}, f = \frac{1}{2}$ of the 2^3S_1 metastable state to $m_f = +\frac{1}{2}, f = \frac{1}{2}$ of the 2^3P state. Optically pumping the C_8 transition is indicated in step 2 of Fig. 2.3. Note that the electron spin-state of the upper electron changes from spin down ($m_f = -\frac{1}{2}$) to spin up ($m_f = +\frac{1}{2}$) in the transition from the 2^3S_1 energy level to the 2^3P energy level.

Once an electron has been optically pumped to some higher energy state, it will relax back to any of the lower-energy states with equal probability (as depicted on the right hand side of Fig. 2.5) [29]. MEOP relies on this sequence of events to create an overpopulation of atoms with electrons in a particular state. For example, when optically pumping the electrons in the 2^3S_1 ($m_f = -\frac{1}{2}$) state, an overpopulation of electrons is created in the 2^3S_1

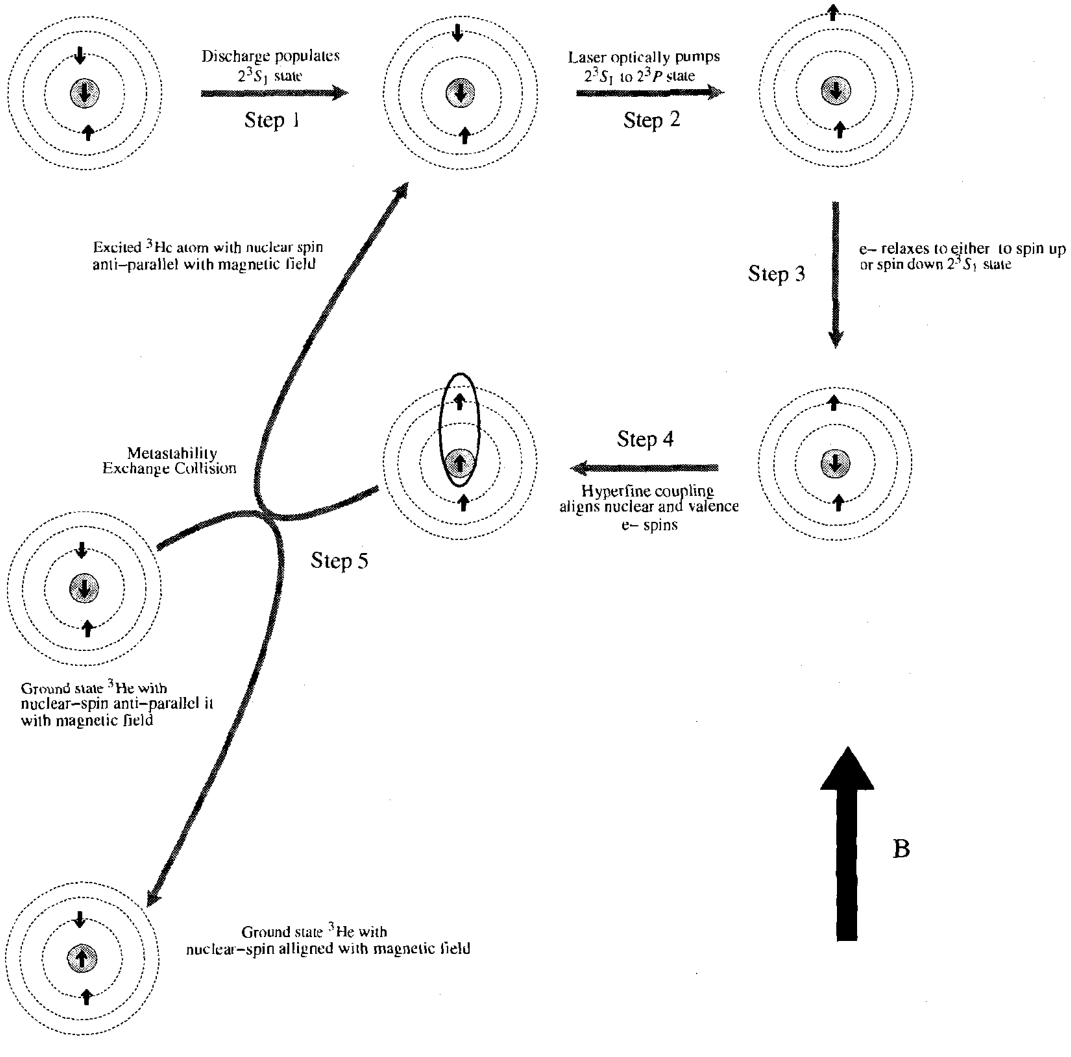

Figure 2.3: A flow-chart for MEOP. The small arrows represent the electron and nuclear spins and their respective orientations in a qualitative sense. The nucleus is enclosed by a series of concentric circles that represent the 1^1S_0, 2^3S_0 and 2^3P atomic states.

($m_f = +\frac{1}{2}$) state. This overpopulation of electrons in the $m_f = +\frac{1}{2}$ state translates to a electron-spin polarization in the 2^3S_1 state. This accumulation of electron-spin polarization is indicated in step 3 of Fig. 2.3. As the polarization builds up in the 2^3S_1 state, the absorption of the 1083 nm optical pumping light decreases as there are less ^{3}He atoms with electrons that can absorb the light [30].

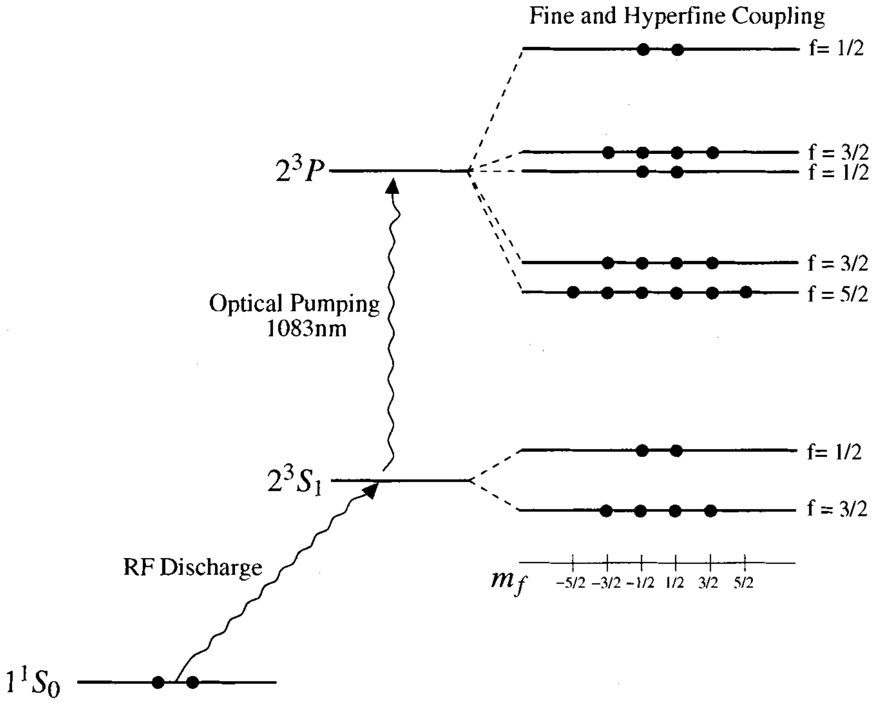

Figure 2.4: The RF discharge drives ^{3}He atoms to various excited states, some of which populate the metastable 2^3S state through radiative decay. These processes are qualitatively summarized with an arrow linking the 1^1S_0 and 2^3S_1 states. Circularly polarized light at 1083 nm is then used to optically pump the metastable atoms into 2^3P states.

The 2^3S_1 electron-spin state is strongly coupled by the hyperfine interaction to the nuclear-spin states. As a result, the electron-spin polarization is partially transfered to create a nuclear-spin polarization in the 2^3S_1 atoms. Hyperfine coupling is indicated schematically by the alignment of the electron and nuclear-spins in step 4 of Fig. 2.3.

Finally, the nuclear-spin polarization is transferred to ground-state atoms by metastability exchange collisions. These collisions occur at a rate of $\sim 10^6\,\mathrm{s}^{-1}$ in low pressure, room temperature helium gas which is significantly faster than the relaxation rate of the 2^3S_1 state. The latter is set by the time for an atom to diffuse across the cell and collide with a wall, about 10^{-3} s for many practical applications [16, 31]. During these collisions, the electrons of ground state atoms can be exchanged with those of 2^3S_1 atoms, without affecting the nuclear-spin orientation [13]. The metastability exchange collision is indicated

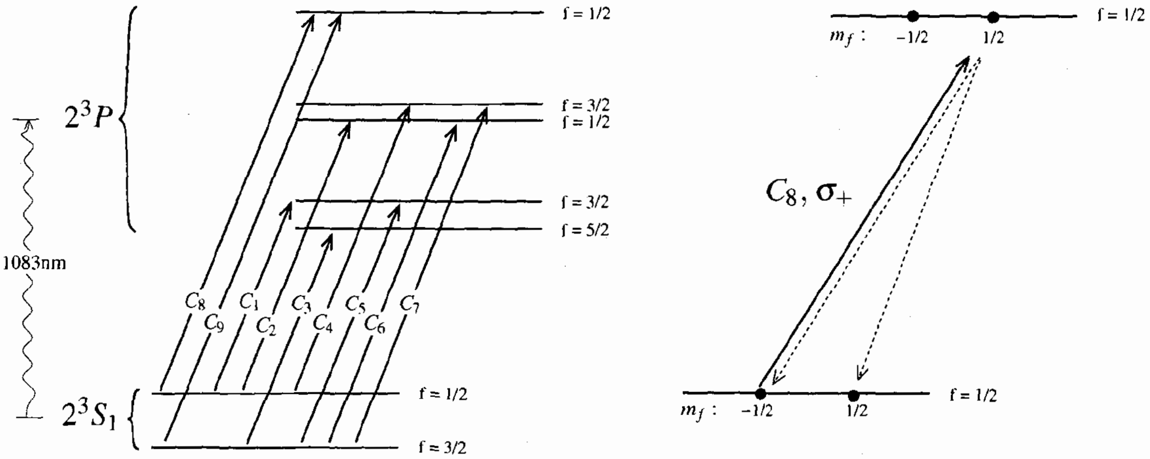

Figure 2.5: The labels $C_1 - C_9$ indicate the allowed $2^3S_1 \rightarrow 2^3P$ transitions when optically pumping with circularly polarized light. The diagram on the right depicts the situation when the C_8 transition is optically pumped with right circularly polarized light. Once the atom has been optically pumped to one of the 2^3P states, it will relax back to the lower energy states with equal probability, as indicated by the dashed arrows.

in step 5 of Fig. 2.3. The ^{3}He atom that acquired the electrons in the 2^3S_1 excited state can now undergo the entire process again!

There are many experimental factors that influence the time required to achieve maximum nuclear-spin polarization in a given sample of ^{3}He. These factors include the material and dimensions of the optical pumping cell, the RF discharge strength, the laser intensity and the pressure of the ^{3}He gas to name only a few. In typical applications this time scale is of order 10 s [10, 13].

In summary, MEOP results in a nuclear-spin polarization of ground-state ^{3}He atoms through optical pumping of the 2^3S_1 state. The nuclear-spin polarization P is defined as

$$P = \frac{N_+ - N_-}{N_+ + N_-} \tag{2.19}$$

where $N_{+(-)}$ is the number of ^{3}He atoms with nuclear spin parallel (antiparallel) to the magnetic field.

2.4 Nuclear Magnetic Resonance

Nuclear magnetic resonance (NMR) can be discussed from either a quantum mechanical or a classical physics perspective. The quantum mechanical treatment is more elegant and is more representative of the underlying physical processes, however the classical treatment is useful as it allows for a more visual interpretation of the phenomena. The classical description of NMR is outlined in this chapter while the quantum mechanical description can be found in most quantum mechanics textbooks such as *Modern Quantum Mechanics* by J.J. Sakurai [32].

Classical Description of NMR

To begin the discussion of NMR, consider a single nuclear-spin. There is a magnetic moment associated with the nuclear-spin that is directly proportional to the gyromagnetic ratio γ of the atom and the the nuclear-spin angular momentum **I**:

$$\boldsymbol{\mu} = \gamma \mathbf{I} \ . \tag{2.20}$$

When the atom is placed in a homogeneous magnetic field $\mathbf{B}_0$ a torque

$$\boldsymbol{\tau} = \boldsymbol{\mu} \times \mathbf{B}_0 \tag{2.21}$$

acts on the magnetic moment. Because the time rate of change of angular momentum is equal to the applied torque, Eq. 2.21 can also be written as

$$\frac{\mathrm{d}\mathbf{I}}{\mathrm{dt}} = \boldsymbol{\mu} \times \mathbf{B}_0 \ . \tag{2.22}$$

Finally, using the relation between the nuclear magnetic moment $\boldsymbol{\mu}$ and spin angular momentum **I**, Eq. 2.22 can be expressed as

$$\frac{\mathrm{d}\boldsymbol{\mu}}{\mathrm{dt}} = \gamma \boldsymbol{\mu} \times \mathbf{B}_0 \ . \tag{2.23}$$

Equation 2.23 reveals that the time rate of change of the magnetic moment is perpendicular to both the magnetic field and the magnetic moment itself. Thus, the magnitude of the magnetic moment is unchanged as it precesses about the magnetic field $\mathbf{B}_0$. The direction of the time rate of change of the magnetic moment defines the sense of the precession of $\boldsymbol{\mu}$

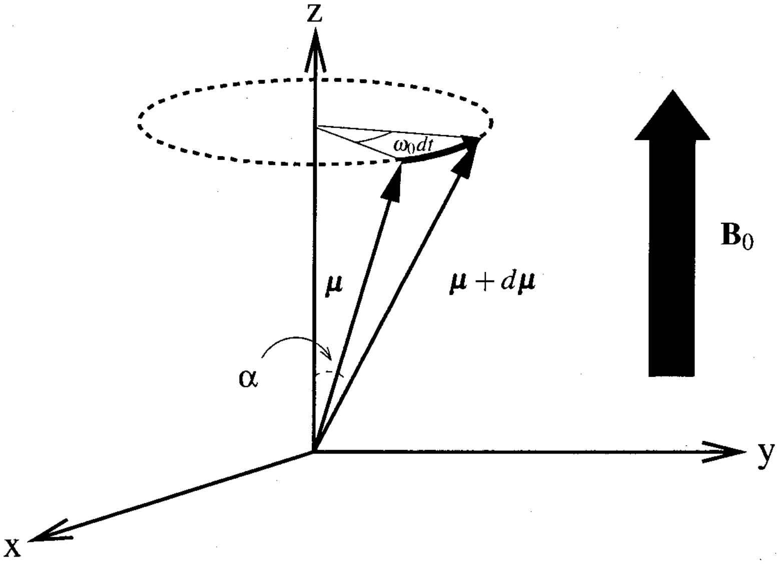

Figure 2.6: The precession of a magnetic moment $\boldsymbol{\mu}$ about $\mathbf{B}_0$. The sense of the precession shown here corresponds to an atom with a negative gyromagnetic ratio, such as ^{3}He.

about $\mathbf{B}_0$. The precession of a nuclear-spin with negative gyromagnetic ratio (eg. γ of ^{3}He is -2.0321×10^8 s^{-1}T^{-1}) is depicted in Fig. 2.6 [33].

The angular frequency ω_0 of the precession can be determined by equating the incremental arc length depicted in Fig 2.6

$$\mathrm{d}\mu = (\omega_0 \mathrm{dt})\,(\mu \sin\alpha) \tag{2.24}$$

with the expression

$$d\mu = \gamma \mu B_0 \sin\alpha \, dt \ , \tag{2.25}$$

obtained from Eq. 2.23. The result, known as the Larmor frequency, is

$$\boldsymbol{\omega}_0 = -\gamma \mathbf{B}_0 \ . \tag{2.26}$$

Typically NMR experiments are conducted on samples containing a large number of nuclear-spins. The sample will exhibit a total magnetic moment $\boldsymbol{m}_{tot}$ which is the the vector sum of the individual magnetic moments of the sample. Though $\boldsymbol{m}_{tot}$ determines the maximum amplitude of an NMR signal, the magnetization is the physical parameter that is often used to describe the magnetic properties of an ensemble of nuclear-spins. The magnetization of the ensemble $\mathbf{M}$ is defined as the total magnetic moment per unit volume

$$\mathbf{M} = \frac{\sum_i \boldsymbol{\mu}_i}{V} = \frac{\boldsymbol{m}_{tot}}{V} \tag{2.27}$$

where the sum is over all of the nuclear spins in the volume V.

In the absence of all interactions, the magnetization $\mathbf{M}$ of an ensemble will exhibit the same time evolution as a single magnetic moment when placed in a magnetic field, namely

$$\frac{\mathrm{d}\mathbf{M}}{\mathrm{dt}} = \gamma \mathbf{M} \times \mathbf{B_o} \; . \tag{2.28}$$

However, since $\mathbf{M}$ is the magnetization of an ensemble, its magnitude changes if the relative alignment or phase of the individual magnetic moments change. Equation 2.28 cannot fully describe the time evolution of $\mathbf{M}$ for an ensemble because it suggests that the magnetization precesses about $\mathbf{B}_0$ indefinitely, and this is not the case for two reasons. The first is that the spins relax back to their equilibrium orientation, by processes collectively referred to as longitudinal or spin-lattice relaxation, characterized by the time constant T_1. The second is that the spins will also de-phase with respect to one-another, by processes collectively referred to as transverse relaxation or spin-spin relaxation, characterized by the time constant T_2. A more complete description of the time evolution of $\mathbf{M}$ is then given by the phenomenological Bloch equation

$$\frac{\mathrm{d}\mathbf{M}}{\mathrm{dt}} = \gamma \mathbf{M} \times \mathbf{B}_0 - \frac{M_x\,\hat{\mathbf{x}} + M_y\,\hat{\mathbf{y}}}{T_2} - \frac{(M_z - M_0)\,\hat{\mathbf{z}}}{T_1} \; , \tag{2.29}$$

where the magnetization is written in terms of its components in the $\hat{\mathbf{x}}$, $\hat{\mathbf{y}}$ and $\hat{\mathbf{z}}$ directions. Using the standard NMR convention and defining $\hat{\mathbf{z}}$ as the direction parallel to $\mathbf{B}_0$, the $\hat{\mathbf{x}}$, $\hat{\mathbf{y}}$ and $\hat{\mathbf{z}}$ components of the Bloch equations can be written separately as

$$\frac{\mathrm{dM_x}}{\mathrm{dt}} = \gamma M_y B_0 - \frac{M_x}{T_2} \tag{2.30}$$

$$\frac{\mathrm{dM_y}}{\mathrm{dt}} = -\gamma M_x B_0 - \frac{M_y}{T_2} \tag{2.31}$$

$$\frac{\mathrm{dM_z}}{\mathrm{dt}} = -\frac{M_z - M_0}{T_1} \; . \tag{2.32}$$

The solutions to these equations are [34]

$$M_x(t) = \left[M_x(0)\cos\omega_0 t + M_y(0)\sin\omega_0 t\right]e^{-t/T_2} \tag{2.33}$$

$$M_y(t) = \left[-M_x(0)\sin\omega_0 t + M_y(0)\cos\omega_0 t\right]e^{-t/T_2} \tag{2.34}$$

$$M_z(t) = M_0\left[1 - e^{-t/T_1}\right] + M_z(0)\,e^{-t/T_1}\ . \tag{2.35}$$

The solutions for $M_x(t)$ and $M_y(t)$ reveal that the transverse magnetization, the component of the magnetization in the xy-plane, precesses about about $\mathbf{B}_0$ with frequency ω_0. The longitudinal magnetization $M_z(t)$, the component of the magnetization along $\mathbf{B}_0$, returns to M_0 as the spins redistribute to the Boltzmann polarization.

In most NMR experiments, an initial magnetization is first established in an ensemble of nuclear-spins. The magnetization is then deliberately perturbed from its alignment with $\mathbf{B}_0$ through the application of second magnetic field $\mathbf{B}_1$ that oscillates as a function of time. To effectively tip the magnetization into the transverse plane, $\mathbf{B}_1$ must be orthogonal to $\mathbf{B}_0$ and sinusoidal, with a frequency equal to the Larmor frequency. The requirements for an effective tipping field can be discussed qualitatively using classical physics.

The technique often used for the classical description of the tipping field is to carry out an analysis in a rotating reference frame. First, let $\mathbf{B}_1$ be linearly polarized along the x-axis with a magnitude $2\mathrm{B}_1$ and frequency ω

$$\mathbf{B}_1 = 2B_1\cos(\omega t)\hat{\mathbf{x}} \qquad . \tag{2.36}$$

$\mathbf{B}_1$ is then expressed as the sum of two circularly-polarized magnetic fields of opposite polarity and equal magnitudes:

$$\mathbf{B}_1 = \left[B_1\cos(\omega t)\hat{\mathbf{x}} + B_1\sin(\omega t)\hat{\mathbf{y}}\right] \tag{2.37}$$

$$+\left[B_1\cos(\omega t)\hat{\mathbf{x}} - B_1\sin(\omega t)\hat{\mathbf{y}}\right] \qquad . \tag{2.38}$$

The component of $\mathbf{B}_1$ that rotates with the same sense as the magnetization is the component that will act to tip the magnetization into the transverse plane. Keeping only the component of $\mathbf{B}_1$ that rotates in a counterclockwise direction, $\mathbf{B}_1$ can then be expressed in the lab frame as

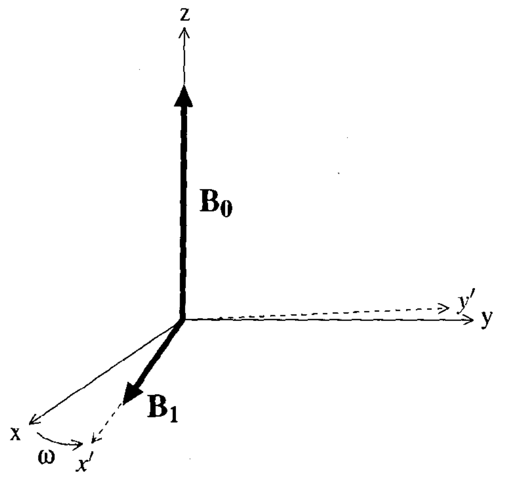

Figure 2.7: The rotating frame (with angular frequency ω) and the laboratory frame. The z-axis of the two frames coincide.

$$\mathbf{B}_1 = B_1\left[\cos(\omega t)\hat{\mathbf{x}} + \sin(\omega t)\hat{\mathbf{y}}\right] \tag{2.39}$$

and in the rotating frame as

$$\mathbf{B}_1 = B_1\hat{\mathbf{x}}' \; . \tag{2.40}$$

At this point it will be useful to define some coordinates. It has already been established that $\mathbf{B}_0$ is parallel to the z-axis, which is also referred to as the longitudinal direction. The rotating frame is indicated by primed coordinates and rotates with a frequency $\boldsymbol{\omega}$, where the direction of $\boldsymbol{\omega}$ is along the positive z-axis, as depicted in Fig. 2.7. Thus, the z′-axis of the rotating frame coincides with the z-axis of the rest frame. The xy-plane and x′y′-plane are referred to as the transverse plane.

To transform dM/dt into the rotating frame, the transformation of the standard time derivative of a vector into a rotating frame is used [35]. That is

$$\frac{\mathrm{d}\mathbf{M}}{\mathrm{d}t} = \frac{\delta\mathbf{M}}{\delta t} + \boldsymbol{\omega} \times \mathbf{M} \tag{2.41}$$

where dM/dt is the time derivative of M in the laboratory frame, $\delta\mathbf{M}/\delta t$ is the time derivative of M in the rotating frame and $\boldsymbol{\omega} = \omega\hat{\mathbf{z}}$. By direct substitution of Eq. 2.28 into Eq. 2.41, an expression for $\delta\mathbf{M}/\delta t$ can be obtained

$$\frac{\delta\mathbf{M}}{\delta t} = \mathbf{M} \times [\gamma\mathbf{B}_0 + \boldsymbol{\omega}] \ . \tag{2.42}$$

This expression can be re-written as

$$\frac{\delta\mathbf{M}}{\delta t} = \gamma\mathbf{M} \times \left[\mathbf{B}_0 + \frac{\boldsymbol{\omega}}{\gamma}\right] \ . \tag{2.43}$$

Equation 2.43 has the same form as Eq. 2.28, if the term in square parentheses is interpreted as an effective magnetic field ($\mathbf{B}_e$) felt by the magnetization in the rotating frame. If an additional magnetic field $\mathbf{B}_1$ directed along the $\mathbf{x}'$-axis is applied, the effective magnetic field felt by the spins in the rotating frame is

$$\mathbf{B}_e = B_1\hat{\mathbf{x}}' + \left(B_0 + \frac{\omega}{\gamma}\right)\hat{\mathbf{z}} \ . \tag{2.44}$$

The purpose of applying $\mathbf{B}_1$ is to tip the magnetization into the transverse plane. Equation 2.44 reveals that if $\mathbf{B}_1$ rotates with angular frequency $\boldsymbol{\omega} = -\gamma\mathbf{B}_0$ (precisely the Larmor frequency), then the effective magnetic field in the rotating frame is simply $\mathbf{B}_1$. The time evolution of $\mathbf{M}$ in the rotating frame is thus governed by:

$$\frac{\delta\mathbf{M}}{\delta t} = \gamma\mathbf{M} \times \mathbf{B}_1 \tag{2.45}$$

and the magnetic moment precesses about $\mathrm{B}_1\hat{\mathbf{x}}'$.

The resonant condition of NMR is when the angular frequency $\boldsymbol{\omega}$ of $\mathbf{B}_1$ is equal to the Larmor frequency $\boldsymbol{\omega}_0$. At resonance, $\mathbf{B}_e = \mathrm{B}_1\hat{\mathbf{x}}'$, and the magnetization will precess about the x$'$-axis at a frequency $\boldsymbol{\omega}_1 = \gamma\mathbf{B}_1$. The B_1 field is usually applied for a short period of time τ in order to rotate the magnetization through an angle α about the x$'$-axis. The tip angle α is

$$\alpha = \omega_1\tau = \gamma B_1\tau \ . \tag{2.46}$$

The tip angle produced through application of $\mathbf{B}_1$ can be adjusted by changing either the magnitude of $\mathbf{B}_1$ or the length of time for which it is applied.

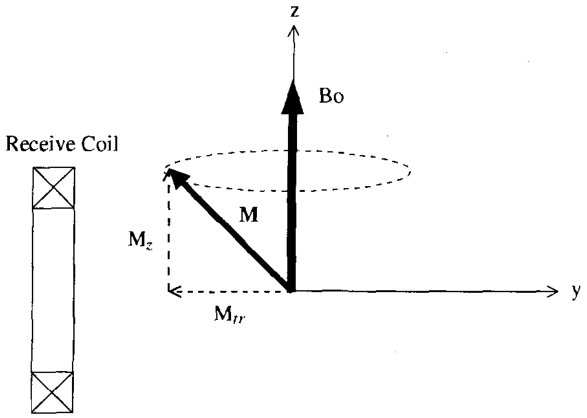

Figure 2.8: A voltage will be induced across a receive coil as the magnetic flux through the receive coil changes in response to the precession of M_{tr} about $\mathbf{B}_0$.

2.4.1 The NMR Signal

Receive coils are used to detect the component of the precessing magnetization that is in the transverse plane. The plane of a receive coil is oriented parallel to $\mathbf{B}_0$ and $\mathbf{B}_1$. This orientation is chosen to optimize the emf induced by the precessing magnetization and to minimize the emf induced by $\mathbf{B}_1$.

To get a better understanding of the parameters that determine the magnitude of the induced emf, consider the geometry depicted in Fig. 2.8. For simplicity, the magnetic flux ϕ_B through a receive coil of N turns and area A is taken to be

$$\phi_B = NAB_y \ . \tag{2.47}$$

Here B_y is the y-component of the magnetic field generated by the magnetization $\mathbf{M}$ and thus B_y is proportional to M_y. If all of the magnetization were tipped onto the y-axis then

$$M_y(t) = M\cos(\omega_0 t)\, e^{-t/T_2} \ . \tag{2.48}$$

By including a constant of proportionality k, ϕ_B can then be expressed in terms of the magnetization

$$\phi_B = kNAM\cos(\omega_0 t)e^{-t/T_2} \ . \tag{2.49}$$

By Faraday's law, the time rate of change of the magnetic flux through the receive coil is equal to the induced emf v

$$v = \frac{d\phi_B}{dt} = kNAM\left[-\omega_0 \sin(\omega_0 t) - \frac{1}{T_2}\cos(\omega_0 t)\right] e^{-t/T_2} \tag{2.50}$$

where M is assumed to be constant. However, for magnetic field strengths of order mT, ω_0 will be of order tens of kHz. In contrast, even for very short transverse relaxation times (< 50ms), $1/T_2$ is only of order a few tens of Hz. Thus, Eq. 2.50 can be approximated as

$$v = -kNAM\omega_0 \sin(\omega_0 t)e^{-t/T_2} \ . \tag{2.51}$$

The $\sin(\omega_0 t)$ term in Eq. 2.51 gives rise to oscillations in the voltage induced across the receive coil. These oscillations are a direct result of the precessing magnetization. The e^{-t/T_2} term of Eq. 2.51 results in a decay of the induced emf amplitude as the uniform phase coherence is lost. The voltage induced across the receive coils is typically passed through several amplification stages. In this thesis, the amplified voltage will be referred to as the NMR signal.

Hyperpolarized gas MR experiments are often conducted in readily-available conventional MRI scanners that operate with magnetic fields of order several Tesla. However, the experiments described in this thesis were conducted at field strengths of order one mT. There are numerous reasons for operating at low-field strengths. Operating at magnetic fields strengths of order mT enables the use of resistive magnets, removing the expense of cryogenic cooling. A low-field resistive magnet also allows for novel magnet designs incorporating more versatility in the orientation of subjects. The rate at which energy is deposited in the subject by radio frequency eddie currents also decreases with frequency, allowing for faster and more intense pulse sequences during an NMR experiment [36]. Finally, gradients resulting from differences in magnetic susceptibilities decrease with field strength. This is an important factor in lung airspace imaging where the difference in magnetic susceptibilities of the alveolar wall and the surrounding air can result in gradients as large as 1 T/m at the alveolar walls for $B_0 = 1.5$ T [2, 6, 37]. By operating at low field strengths these gradients are reduced which gives rise to an increase in the duration of the NMR signal.

2.5 Hyperpolarized ^{3}He NMR

The motivation for using hyperpolarized ^{3}He for MR experiments is revealed through a comparison of its magnetization relative to that of water.[1] In general, the magnetization is proportional to the magnetic moment of the atom μ, the polarization P and the total number of spin-bearing atoms N. For a sample of volume V:

$$M = \frac{\mu NP}{V} . \tag{2.52}$$

Because of the difference in atomic densities, the number of spin-bearing atoms and hence the magnetization of a water sample will be much larger than that of a gaseous sample with the same polarization and volume. For example, the number of ^{1}H atoms in 1 mL of H_2O is of order 6700×10^{19}, whereas only 2.4×10^{19} ^{3}He atoms are contained in the same volume at room temperature and atmospheric pressure. Thus, for the same polarization, the magnetization of the water sample will be three orders of magnitude larger than that of the gas sample.

In conventional MR experiments, the magnetization results from the Boltzmann distribution of ^{1}H atoms between nuclear-spin states and can be calculated using statistical mechanics. As described in Section 2.2, at zero magnetic field the ground state of a spin $\frac{1}{2}$ atom (^{1}H or ^{3}He) has two degenerate eigenstates: $m_f = \pm\frac{1}{2}$, as depicted in Fig. 2.9. This degeneracy is lifted when the atoms are placed in a magnetic field, $\mathbf{B}_0$ and the nuclear magnetic moments will either align parallel (↑ the lower, energetically-favored eigenstate) or antiparallel to $\mathbf{B}_0$ (↓ the higher energy eigenstate). If E_+ denotes the energy of the state with nuclear magnet moment $\boldsymbol{\mu}$ parallel to $\mathbf{B}_0$ and E_- the energy of the state with $\boldsymbol{\mu}$ antiparallel to $\mathbf{B}_0$, then by use of $U = -\boldsymbol{\mu} \cdot \mathbf{B}_0$

$$E_+ = -\frac{|\gamma|\hbar B_0}{2} \tag{2.53}$$

$$E_- = +\frac{|\gamma|\hbar B_0}{2} . \tag{2.54}$$

---

[1] The comparison is made with water because the human body is mostly water and the vast majority of human MRI scans interrogate the protons (^{1}H atoms) associated with water molecules.

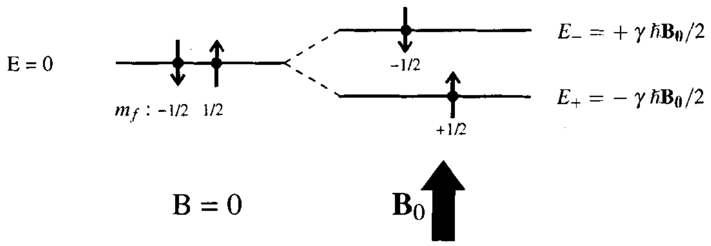

Figure 2.9: In zero magnetic field, the two magnetic sublevels of the ground state $m_f = \pm\frac{1}{2}$ are degenerate. The application of a magnetic field lifts this degeneracy.

The energy difference ΔE between the two states is given by

$$\Delta E = \gamma\hbar B_0 \ . \tag{2.55}$$

As previously discussed, the polarization is defined as

$$P \equiv \frac{N_+ - N_-}{N_+ + N_-} \ , \tag{2.56}$$

where $N_{+(-)}$ is the number of atoms with nuclear spins parallel (antiparallel) to $\mathbf{B}_0$. The distribution of atoms between states is

$$\frac{N_+}{N_-} = e^{-\frac{\Delta E}{kT}} \ . \tag{2.57}$$

By combining Eqs. 2.55, 2.56 and 2.57 an expression for the Boltzmann polarization is obtained:

$$P = \tanh\left[\frac{\gamma\hbar B_0}{2kT}\right] \ . \tag{2.58}$$

where k is the Boltzmann constant and T is the temperature of the sample. For a conventional MR field strenth of 1 T, the Boltzmann polarization of 1 mL of water is only 5 ppm and results in a magnetization of order 5×10^{-3} J/T/m^3. The polarization of hyperpolarized gas produced by MEOP is typically of order 0.5 (three out of every four), and for 1 cm^3 of ^{3}He at atmospheric pressure, this gives rise to a magnetization of order 0.01 J/T/m^3! The actual magnetization of hyperpolarized gas used in MR experiments is usually smaller than this because the hyperpolarized gas is often produced at lower pressures (tens of Torr) and is then diluted with ^{4}He or N_2 to achieve a desired volume at atmospheric pressure. On the other hand, the NMR signal amplitude is determined by the magnitude of the magnetization that is tipped into the transverse plane. This is particularly important in hyperpolarized gas NMR because the magnetization is non-renewable, forcing experiments to be conducted using combinations of small tip angles. In summary, the NMR signal amplitudes from hyperpolarized gas can be made comparable to those achieved in conventional MR imaging.

2.5.1 Relaxation

In NMR, relaxation refers to a loss of magnetization that results from the redistribution of nuclear-spins amongst the available eigenstates. Nuclear-spin relaxation is categorized as either longitudinal or transverse relaxation. Longitudinal relaxation is the decay of magnetization colinear with $\mathbf{B}_0$ and results in a re-establishment of the equilibrium nuclear-spin polarization. Transverse relaxation is the decay of magnetization that has been tipped into the transverse plane and amounts to an irreversible loss of coherence associated with the precessing nuclear-spins.

Longitudinal Relaxation

The magnetization of a hyperpolarized ensemble of nuclear-spins will always decay irreversibly as the spins redistribute into the Boltzmann polarization. The longitudinal relaxation time T_1 for hyperpolarized gas is defined as the time for the magnetization colinear with $\mathbf{B}_0$ to decay to 1/e of the initial magnitude. Under optimal conditions, T_1's of hundreds of hours have been achieved for hyperpolarized ^{3}He [10]. For the work discussed in this thesis, achieving long T_1's in hyperpolarized ^{3}He is desirable for two reasons. The first is that a longer T_1 allows for an increase in the magnetization of the collected gas. This is because the maximum polarization is determined by the production and loss rates. The second reason is that a longer T_1 gives rise to an increase in the time during which hyperpolarized gas can be stored as well as the time during which NMR experiments can be conducted.

The longitudinal relaxation time can be expressed in terms of contributions from gradient-induced relaxation due to inhomogeneities in $\mathbf{B}_0$ ($T_{1,\nabla B}$), interactions with paramagnetic O_2 (T_{1,O_2}) present as a contaminant in the gas and wall relaxation ($T_{1,w}$):

$$\frac{1}{T_1} = \frac{1}{T_{1,\nabla \mathrm{B}}} + \frac{1}{T_{1,O_2}} + \frac{1}{T_{1,w}} . \tag{2.59}$$

For hyperpolarized ^{3}He diffusing in a magnetic field $\mathbf{B}_0$ oriented in the z-direction, it is the gradient of the z-component of the field that determines $T_{1,\nabla B}$. A relatively simple formula that governs the longitudinal relaxation rate $T_{1,\nabla B}$ has been written here in terms of the mean time between interatomic collisions τ_c and the mean squared velocity $< v^2 >$ of colliding atoms [38]:

$$\frac{1}{T_{1,\nabla B}} = \frac{2}{3} < v^2 > \left[\frac{1}{B_0^2} \left(\frac{\partial B_0}{\partial z} \right)^2 \right] \frac{\tau_c}{1 + \omega_0{}^2 \tau_c{}^2} . \tag{2.60}$$

The longitudinal relaxation time $T_{1,\nabla B}$ only includes the effect of the diffusive motion of ^{3}He in the gradient $\partial B_0 / \partial z$ when $\mathbf{B}_0$ is the dominant field. Schearer et al. measured $\tau_c = 2.2 \pm 0.2 \times 10^{-7} p^{-1}$ s^{-1} at room temperature, where p is the pressure of the gas in Torr [38]. In the experiments discussed in this thesis, the Larmor frequencies are of order 20 kHz and the pressures are of order 1-10 Torr making the term $\omega_0{}^2 \tau_c{}^2$ negligeable compared to 1. In this regime, the last term of Eq. 2.61 is reduced to τ_c and thus $T_{1,\nabla B}$ is directly proportional to pressure

$$\frac{1}{T_{1,\nabla B}} \propto \frac{2}{3} < v^2 > \left[\frac{1}{B_0^2} \left(\frac{\partial B_0}{\partial z} \right)^2 \right] \frac{1}{p} . \tag{2.61}$$

As a result, $T_{1,\nabla B}$ can be increased by improving the homogeneity of $\mathbf{B}_0$ or by increasing the pressure of the gas [24, 38, 39].

Oxygen gas (O_2) is a paramagnetic molecule that generates a large, short-ranged dipolar magnetic field. Because O_2 is one of the constituents of air, quantifying the relaxation effect it has on hyperpolarized ^{3}He is important for MR imaging as it will determine the available imaging time. During collisions between ^{3}He and O_2, the dipolar interaction will act to destroy the orientation of the ^{3}He nuclear-spin with $\mathbf{B}_0$, ultimately leading to a destruction of the polarization of the ensemble. The presence of O_2 will reduce the longitudinal relaxation time T_1 of hyperpolarized ^{3}He gas [40]. Saam, Happer and Middleton determined an expression for T_1 that is written as a function of the concentration $[O_2]$ of O_2 in Amagat and the temperature T of the sample

$$\frac{1}{T_1} = 0.45[O_2]\left(\frac{299\ \mathrm{K}}{T}\right)^{0.42} \mathrm{s}^{-1}\mathrm{Amagat}^{-1} \tag{2.62}$$

where 1 Amagat = 44.614774 mol m^{-3} under STP conditions [40, 41]. By rewriting Eq. 2.62 in terms of p_{O_2}, the partial pressure of O_2 in Pascals, and taking $T = 300$ K, a formula that is very useful for our work is derived [10]

$$\frac{1}{T_1} = 3.85 \times 10^{-6}\ p_{O_2}\ \mathrm{s}^{-1}\,\mathrm{Pa}^{-1}\ . \tag{2.63}$$

When hyperpolarized ^{3}He is used to acquire MR images of lung airspaces, the unavoidable presence of O_2 in the lungs will decrease T_1 once the gas has been inhaled. If the volume percentage of O_2 in air is taken to be 20%, and the lungs are assumed to contain air at atmospheric pressure, then Eq. 2.63 indicates that T_1 would only be 13 s! This implies that MR imaging of ^{3}He in the lungs must be done in seconds.

The material of the cell walls used to contain the hyperpolarized gas can also influence the relaxation time [24, 25, 42]. This effect can be isolated by measuring T_1 in pure ^{3}He in sufficiently homogeneous fields, thus minimizing the contributions from $T_{1,\nabla B}$ and T_{1,O_2}.

The effect of longitudinal relaxation appears slightly different for hyperpolarized gases than for conventional MR samples. This can be explained using the solution to the Bloch equation for the longitudinal component of the magnetization M_z (given in Eq. 2.35) which is

$$M_z(t) = M_0\left[1 - e^{-t/T_1}\right] + M_z(0)\, e^{-t/T_1} \tag{2.64}$$

where M_0 is the magnetization corresponding to the Boltzmann polarization. Equation 2.64 governs the time evolution of the longitudinal magnetization for both conventional and hyperpolarized gas NMR. However, the initial magnetization $M_z(0)$ corresponding to hyperpolarized gas is typically several orders of magnitude larger than M_0, and as a result the magnetization appears to behave very differently in the two cases. This can be understood by first considering how the magnetization evolves in conventional MRI. If the magnetization of a sample is unperturbed for a time much longer than T_1, it will have reached its equilibrium magnetization which is precisely the magnetization that corresponds to the Boltzmann (equilibrium) polarization (see Eq. 2.64). Now consider the magnetization after a 90° tipping pulse is applied at time $t = 0$. Immediately after the pulse, there is no magnetization in the longitudinal direction and so $M_z(0) = 0$. As time progresses the first term in Eq. 2.64 increases and the magnetization returns to its equilibrium value, M_0. If a smaller tipping angle is applied only a fraction of M_0 is rotated into the transverse plane. For example, if a 60° tipping pulse is applied, $\frac{1}{2}M_0$ is left in the longitudinal direction. In this case, immediately after the 60° tipping pulse, the longitudinal magnetization $M_z(0) = \frac{1}{2}M_0$. As time evolves, the contribution from the first term increases toward M_0 and the contribution from the second term decreases toward zero. Overall the longtidunal magnetization evolves towards its equilibrium value M_0.

The time evolution of the magnetization corresponding to a hyperpolarized gas sample is also governed by Eq. 2.64. However, the initial magnetization $M_z(0)$ is several orders of magnitude larger than the equilibrium magnetization M_0 and thus at time $t = 0$ the longitudinal magnetization $M_z(0)$ is the magnetization M of the hyperpolarized gas: $M_z(0) = M$. As time progresses, the contribution from the first term in Eq. 2.64 increases toward M_0 and the contribution from the second term decreases toward zero. However, $M_z(0)$ is so much larger than M_0 that the second term dominates the evolution of the magnetization and it appears as though the magnetization is decaying towards zero! For this reason, the time evolution of the magnetization of a hyperpolarized gas sample can be approximated by dropping the M_0 term in Eq. 2.64

$$M(t) \cong M(0)\, e^{-t/T_1} \ . \tag{2.65}$$

This means that the magnetization will decay even if left unperturbed by a tipping pulse. Thus, the non-equilibrium nature of the magnetization imposes a *time* limit on the NMR experiments.

Transverse Relaxation

Transverse relaxation results from nuclear-spin dephasing and from longitudinal relaxation combined. Nuclear-spin dephasing is caused by interactions between the nuclear-spins of different atoms (characterized by the spin-spin relaxtion time T_2) and from random displacement of atoms in the presence of field inhomogeneities in $\mathbf{B}_0$. Longitudinal relaxation causes a decay in transverse magnetization as the nuclear-spins redistribute into a Boltzmann polarization. Once the magnetization is tipped into the transverse plane, the NMR signal will decay exponentially with a characteristic time constant T_2^*. T_2^* can be written in terms of these three contributions as

$$\frac{1}{T_2^*} \cong \frac{1}{2T_1} + \frac{1}{T_2} + \gamma \Delta B_0 \tag{2.66}$$

where T_1 is the longitudinal relaxation time, T_2 is the transverse relaxation time constant for spin-spin interactions alone and ΔB_0 is a measure of the field inhomogeneities experienced by atoms as they move within the confines of the sample [43].

In Section 2.4.1, the effects of the field inhomogeneity and longitudinal relaxation were ignored and the NMR signal amplitude decay was governed by the spin-spin relaxation time T_2. However, for the experiments discussed in this thesis, these effects cannot be ignored and the decay of the NMR signal amplitude is governed by T_2^*.

Let us consider the particular regime when the effect of the magnetic field inhomogeneities dominate the transverse relaxation time and

$$\frac{1}{T_2^*} \cong \gamma \Delta B_0 \ . \tag{2.67}$$

If the pressure of the gas is low (of order one Torr) then the helium atoms are restricted to diffuse within the cell and ΔB_0 can be approximated by the difference in field strengths across the sample. This approximation can be used to obtain the order of magnitude of T_2^*. The NMR signal amplitude of these low-pressure hyperpolarized gases will decay exponentially. However, when the pressure is high ($\geq$ 100 Torr) the atoms are confined to a region much smaller than the sample volume which affects the decay of the NMR signal amplitude. As an example, consider a spherical sample volume of radius R in a magnetic field with a uniform (linear) gradient $\mathbf{G}$. The magnitude of the magnetic field at position $\mathbf{r}$ is

$$B(\mathbf{r}) = B_0 + \mathbf{G} \cdot \mathbf{r} \tag{2.68}$$

where B_0 is the field strength at the centre of the sample. The envelope of NMR signal $A(t)$ is obtained by integrating the transverse magnetization over the cell volume and for this particular example is

$$A(t) = A\left[\frac{3\sin(t/\tau)}{(t/\tau)^3} - \frac{3\cos(t/\tau)}{(t/\tau)^2}\right] . \qquad (2.69)$$

The parameter $\tau = 1/\gamma GR$. Thus, Eq. 7.3 reveals that the decay of the NMR signal amplitude for a spherical sample of gas at high pressure ($\geq$100 Torr) in a magnetic field with a constant gradient is definitely not exponential! This particular example has been introduced because it is a reasonable approximation of the conditions of some experiments discussed in Chapter 7.

Chapter 3

Metastability Exchange Optical Pumping Station

This chapter provides a general description of the gas-handling manifold as well as the coils that are used to generate the magnetic field for the metastability exchange optical pumping (MEOP) station. Figure 3.1 is an overall schematic diagram of the MEOP station showing the various elements of the MEOP station. The magnetic field coils, the glassware and stainless steel sections of the gas-handling manifold will each be discussed separately.

3.1 The Homogeneous Magnetic Field

A uniform magnetic field is needed for optical pumping in order to provide a well-defined quantization axis and to remove the degeneracy between the magnetic sublevels of ground state ^{3}He atoms. MEOP can be accomplished in the Earth's magnetic field, but producing an independent homogeneous magnetic field $\mathbf{B}_0$ reduces the relative importance of local field inhomogeneities and enables a convenient orientation of the quantization-axis. To minimize gradient-induced relaxation of the nuclear-spin polarization, $\mathbf{B}_0$ should be static and homogeneous over the volume traversed by the hyperpolarized ^{3}He atoms.

In the present apparatus, $\mathbf{B}_0$ is generated by seven, 32 cm radius coils, as shown in Fig 3.2. The number of turns, the current and the exact spacing between the seven coils have been adjusted to optimize the field homogeneity in the region of the optical pumping

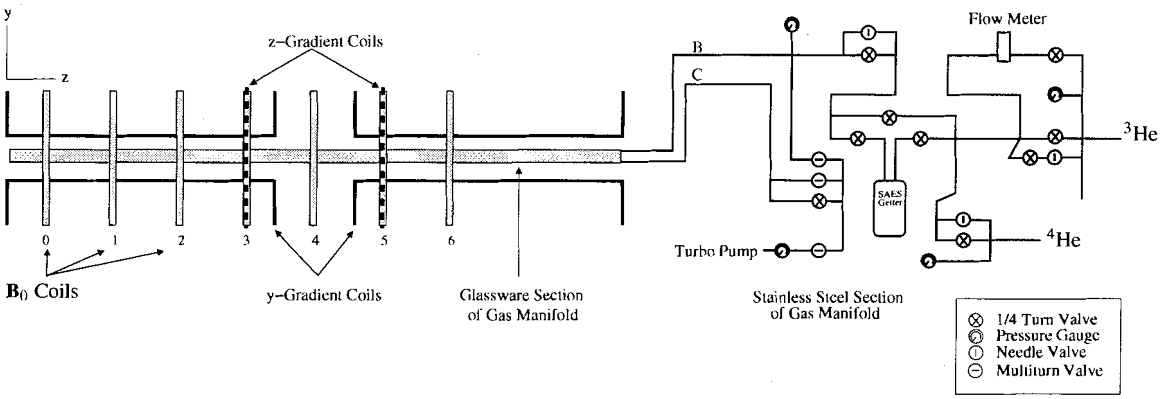

Figure 3.1: A schematic diagram showing the layout of the MOEP station. Each section of this apparatus will be shown in greater detail in later diagrams.

cell. Previous measurements indicate that $\mathbf{B}_0$ is uniform at the level of 10^{-8} T/cm or better over a 7 L cylindrical volume aligned with the axis of coil 3 [42].

For a current of 2.45 A, the magnetic field strength produced by the B_0 coils is 5.96 mT. This magnetic field strength was chosen because the corresponding ^{3}He Larmor frequency (19.28 kHz) was within a low-noise region of the laboratory environment.

3.2 The Magnetic Field Gradient Coils

Two sets of magnetic field gradient coils were added to the MEOP system to improve the field homogeneity in the vicinity of the storage cell which is located off the axis of the B_0 coils. Improving the field homogeneity within the storage cell is particularly important because field gradients will induce relaxation of the hyperpolarized gas as it diffuses within the storage cell volume. The center of the storage cell is situated at (0 cm, 10 cm, 10cm) relative to the center of coil 3 in Fig. 3.2. Because of the storage cell position relative to the region of maximum $\mathbf{B}_0$ homogeneity, the gradients in $\mathbf{B}_0$ in the the y and z-directions were larger than that in the x-direction. Two independent sets of coils were designed to generate magnetic field gradients that act to cancel gradients in $\mathbf{B}_0$. These gradient coils are used primarily to improve the T_1 of the hyperpolarized gas contained in the storage cell.

The z-gradient is produced by a pair of single-turn coils of radius 0.32 m that are sep-

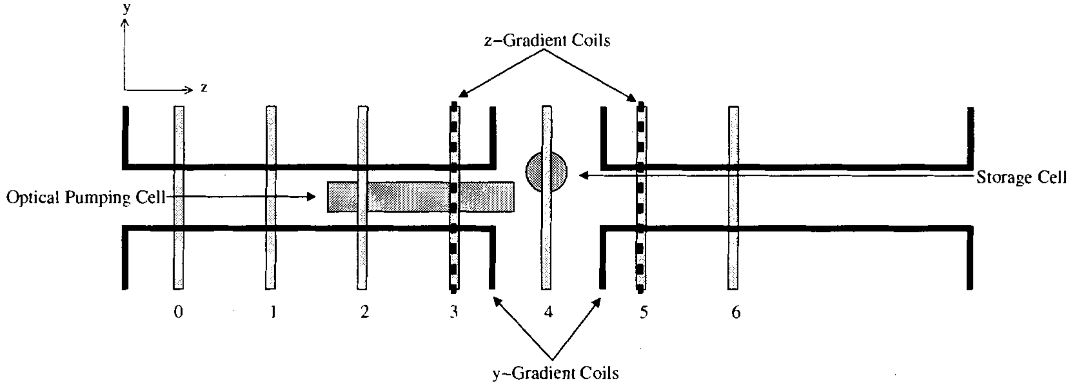

Figure 3.2: A cross-sectional view of the relative positions of the magnetic field coils, the storage and optical pumping cells. Seven coils are used to produce B_0 (labelled 0-6). The z-gradient coil is a quasi-Maxwell pair wound on top of B_0 coils 3 and 5. The y-gradient coil is a standard saddle-coil design.

arated by 0.36 m as shown in Fig. 3.3. The z-gradient coils are centered about the storage cell and to lowest order produce a linear magnetic field gradient $\mathrm{dB_z/dz}$ along the z-axis. Fig. 3.3 shows a simplified schematic diagram of the z-gradient field where the field direction and relative strength are indicated with arrows. Current flows in the opposite sense in the two coils. The strength of the z-gradient was measured using a Gaussmeter (Group3 DTM-151) and found to be 120 ±5 nT/A/cm. Improvements in field homogeneity resulting from the introduction of these coils were quantified by measuring the T_2^* of hyperpolarized gas contained in a sealed cell. When the field homogeneity has been optimized, the z-gradient field improves the T_2^* of 0.993 Torr ^{3}He contained in a cylindrical cell ($r = 2.4$ cm and $\ell = 3.5$ cm) from 0.025 s to 1.250 s. A current of 1.4 A is necessary to optimize the overall field homogeneity along the z-axis.

The y-gradient coils were constructed with 3 turns of wire wound in a standard saddle-coil geometery of radius $R = 32.4$ cm. The y-gradient coils produce a linear magnetic field gradient $\mathrm{dB_z/dy}$ along the y-axis. The y-gradient field is depicted in Fig. 3.4. The y-gradient coils are coaxial with the B_0 coils and are centered about the storage cell, as shown in Fig. 3.2. The field of interest is produced primarily by the four inner-most arcs. The positions of the most distant arcs are placed to maximize the gradient linearity at the centre of the coils. This type of coil design is attributed to Golay, and is such that each

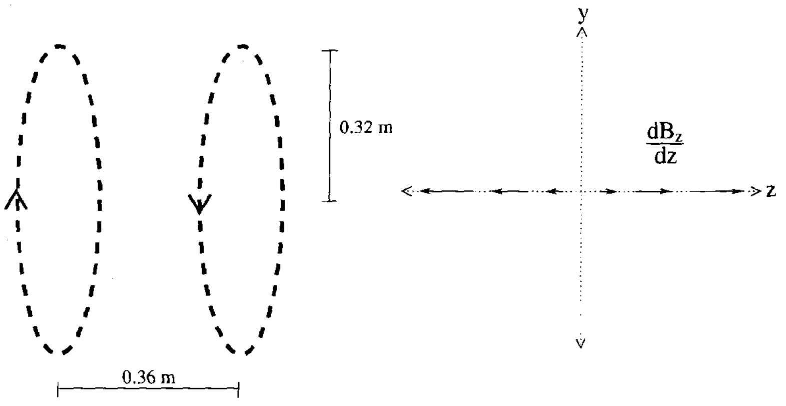

Figure 3.3: The z-gradient coils (drawn with dotted lines as in Fig. 3.2) are used to produce a linear magnetic field gradient along the z-axis. The z-gradient field is depicted on the right where the arrows represent the direction and relative strength of the magnetic field along the axis.

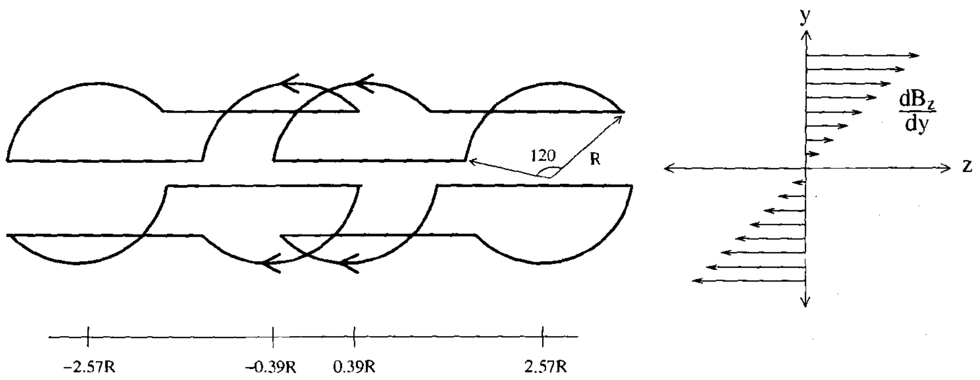

Figure 3.4: The saddle coil geometry used for the y-gradient coils. Current-flow directions are indicated by arrows. The y-gradient field is depicted on the right where the arrows represent the direction and relative strength of the magnetic field.

arc subtends 120° of a circle of radius R, and the arcs are located at $z = \pm 0.39$ R and ± 2.57 R [44]. The strength of the y-gradient was measured using a Gaussmeter and found to be $350 \pm 5\,\mathrm{nT/A/cm}$.

The expected magnetic field gradient can be calculated analytically for this saddle coil configuration. This is done by constructing an expression for the magnetic vector potential using the appropriate surface currents for a saddle coil configuration and making use of a Green's function expansion [45–47]. The expression that approximates the field gradient in the y-direction in the vicinity of the origin is given by [48]

$$\frac{1}{I}\frac{\mathrm{dB_z}}{\mathrm{dy}} = \frac{N}{R^2} 9.18 \times 10^{-7} \mathrm{T/A/m}\ . \tag{3.1}$$

For $R = 34.2$ cm, and $N = 3$ turns of wire, the above expression gives a y-gradient of $235\,\mathrm{nT/A/cm}$. There is a significant difference between the actual magnetic field gradient and the gradient that is expected to be produced. This is of secondary importance to the gradient linearity.

3.3 The Stainless Steel Section of the Gas Manifold

The stainless steel section of the gas-handling manifold lies outside the B_0 coils and is responsible for coupling the ^{3}He and ^{4}He storage tanks as well as a turbo pump to the heart of the MEOP station, which is largely constructed of glass. Its position relative to the other components of the MEOP station is shown in Fig. 3.1 and Fig. 3.5 is a larger depiction of this schematic diagram. The stainless steel is electropolished $1/4''$ tube with Swagelok fittings. The electropolished stainless steel pumps down faster than unpolished tubing and helps to maintain the purity of the helium gas. The gas manifold is equipped with needle valves for fine flow control, multi-turn valves for coarse flow control and 1/4-turn valves for on/off control of the helium flow (see Fig. 3.5). A SAES getter (Rare Gas Purifier, PS2-GC50-R) is used to purify ^{3}He and ^{4}He before it is admitted to the glassware section of the MEOP station. The getter reduces contaminants other than noble gases, to less than 10 ppb. The gas manifold is also equipped with four pressure gauges. High pressure piezoresistive transducers (Keller PAA-23S) are situated at both the ^{3}He and ^{4}He inlets. Capacitance manometers (Edwards Model 600) are used to monitor the pressure at the turbo pump and

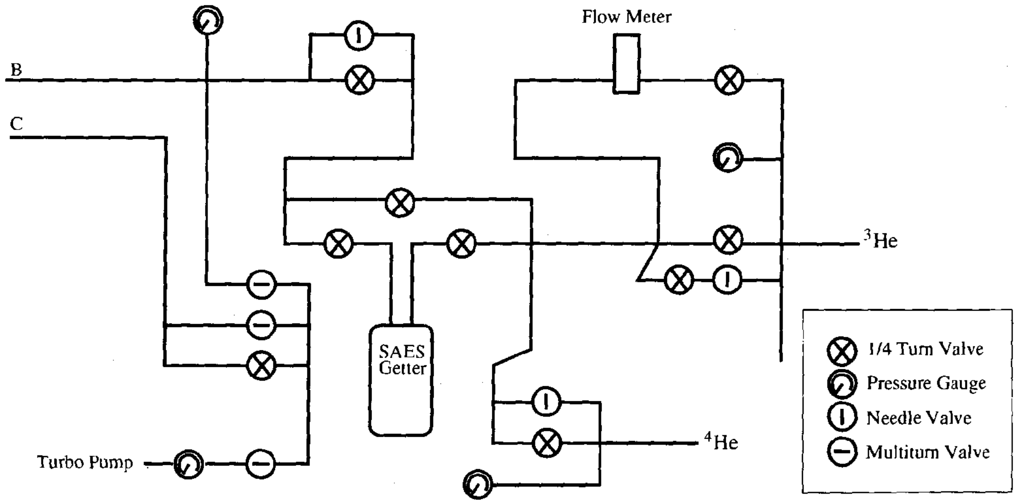

Figure 3.5: The front panel of the stainless steel section of the gas manifold. The layout of the components reflects their physical positioning. Lines B and C couple to the glass gas-handling manifold, as shown in Fig. 3.6.

at the point where the gas enters the glassware section of the MEOP station (Line B) as shown in Fig. 3.5. Lines B and C in Fig. 3.5 connect to lines B and C of the MEOP station glassware in Fig. 3.6. The stainless steel and borosilicate tubing of these lines is coupled using Swagelok 321 stainless steel to Pyrex 7740 couplers (Swagelok G321-4GX-2).

3.4 The Borosilicate Section of the Gas Manifold

Borosilicate glass is used for a large section of the gas manifold simply because it provides a compromise between low wall relaxation rates for hyperpolarized ^{3}He and ease of fabrication. A schematic diagram of the glassware section of the MEOP station gas-handling manifold, including the relative positions of the OPC, the compressor, the storage cell, the two pressure-transducers and the various valves that are used to control the gas flow is shown in Fig. 3.6. During continuous-flow MEOP, ^{3}He flows through the OPC via line B, through the compressor, and is then collected in the spherical storage cell (R= 4.5 cm). The dotted line shown in Fig. 3.6 traces this path through the MEOP station glassware.

The glassware is equipped with two non-magnetic piezoresistive pressure transducers

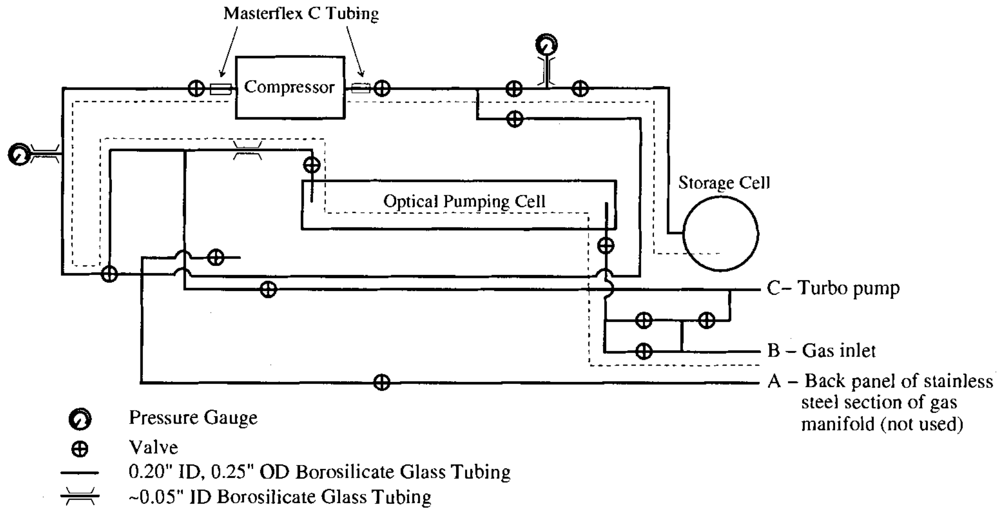

Figure 3.6: A detailed schematic of the glassware of the MEOP station gas manifold. The dotted line traces the path of ^{3}He through the glassware during continuous-flow MEOP.

(Keller PAA-2/8750). Epoxy was used to couple the transducers to the glassware with a vacuum-tight seal. The piezoresistors of the transducers are arranged in a Wheatstone-Bridge configuration and provide a voltage that is linearly proportional to pressure. The transducer at the storage cell inlet was chosen to have a lower sensitivity than the transducer at the compressor inlet because the pressure at the storage cell is routinely higher (>100 Torr) than at the compressor inlet (1-2 Torr). The transducer at the storage cell was calibrated and found to have a sensitivity of 0.138±0.01 V/Torr, whereas the the transducer at the compressor inlet was calibrated at 4.04±0.01 V/Torr. The sensitivity of the transducer has been constant during the three years they have been in use, however the offset does change periodically and should be routinely noted. Despite the transient offset, the pressure transducers are acceptable for this system because they are non-magnetic and are leak-tight under vacuum and thus do not cause relaxation of the ^{3}He magnetization.

The majority of the glassware is constructed of $1/4''$ borosilicate glassware, however there are three sections of the glassware where the tube diameter is reduced to about 1 mm (20% of diameter of the rest of the tubing) which are used to restrict the gas flow. One of these constrictions is situated imediately downstream from the OPC and is used to reduce the likelihood that gas near the compressor diffuses back into the OPC. The two other con-

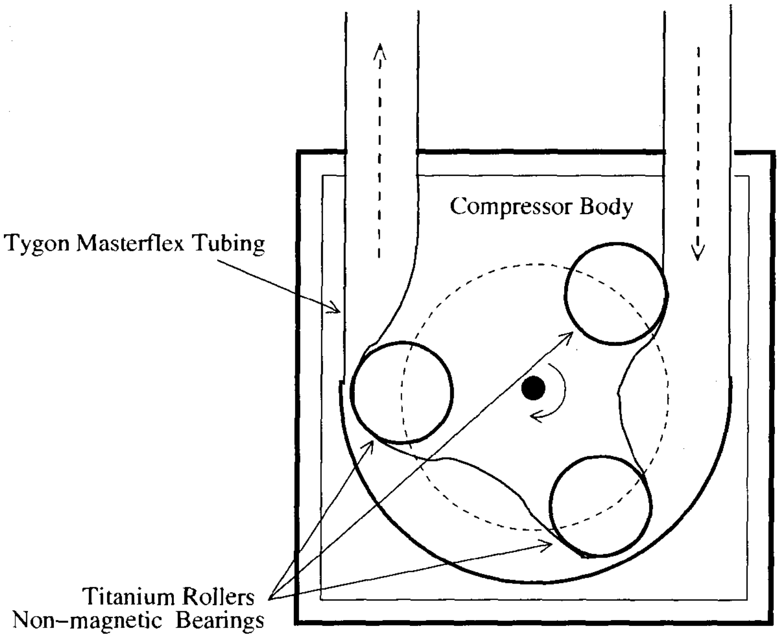

Figure 3.7: A schematic diagram of a cross-section of the compressor body.

strictions are situated between the pressure transducers and the gas manifold and are used to reduce the probability that atoms travel up to the transducer and back down again. Minimizing these occurences is necessary because the pressure transducer is slightly magnetic and will effect the nuclear-spin orientation of ^{3}He atoms in its vicinity.

3.5 The Compressor

The compressor is a peristaltic pump that is used to move low pressure ^{3}He from the OPC to the storage cell. The gas is contained within a soft, elastic tubing that is mounted along the inner circumference of the circular bore of the compressor body. The main axle of the compressor has three rollers situated at its perifery that compress the tubing and force the gas forward as the axle rotates (see Fig. 3.7).

Peristaltic pumps are more commonly used to control fluid flow. There are several aspects of the compressor design that reflect its use here to compress hyperpolarized gas. First and formost, to ensure minimal relaxation of the ^{3}He polarization, the compressor was constructed entirely out of non-magnetic materials such as PVC, titanium and glass bearings. In addition, the body of the compressor can be sealed and operated under vacuum. This prevents the soft tubing through which the gas flows from collapsing. The tubing is manufactured by Masterflex© (Tygon©, Cole-Parmer 96420-17)for the food processing industry. This tubing material is silicone-based and is attacked by hydrocarbon-based oils, thus the compressor body is partially filled with vegetable oil which serves as a lubricant. The oil also acts to increase the heat constant of the compressor body which helps prevent overheating of the non-magnetic bearings (glass balls in plastic races). An equally important design modification is the addition of a check (one-way) valve (Cole-Parmer 98553-12) that is situated immediately after the compressor outlet. The check valve effectively maintains a lower average pressure at the compressor outlet as the pressure in the storage cell increases, ultimately keeping the gas in the storage cell out of the compressor. And finally, the compressor lines are coupled to the MEOP Station glassware with $1/4''$ Masterflex C vacuum tubing (Cole-Parmer 06424-71), so that the compressor can easily be removed from the MEOP station if maintenance is required. This paritcular tubing was chosen because hyperpolarized ^{3}He has a low wall relaxation rate with Masterflex C tubing.

The compressor pumping rate is adjustable, but in use has been limited to a rotation of 300 rpm for a maximum of 10 min. This limit has been set to prevent overheating and subsequent melting of the plastic races of the non-magnetic bearings. Figure 3.8 is a photograph showing the inner workings of the compressor and illustrates the type of damage that results from overheating. For experiments presented in this thesis, the compressor was operated at about 80 rpm which corresponds to a ^{3}He atom flow-rate of about 9×10^{16} atoms/s for a pressure of 1 Torr in the OPC (assuming the pressure in the storage cell increased about 8 Torr in 10 min).

3.6 Summary

A simplifed schematic diagram of the gas flow path through the MEOP station has been included in Figure 3.9. Low pressure (1-2 Torr) ^{3}He flows from the stainless steel section (not shown in Fig. 3.9) to the glassware section of the gas-handling manifold, and finally into the optical pumping cell (OPC). The ^{3}He gas is optically pumped as it flows through the OPC. The compressor draws the low pressure hyperpolarized ^{3}He from the OPC and pumps

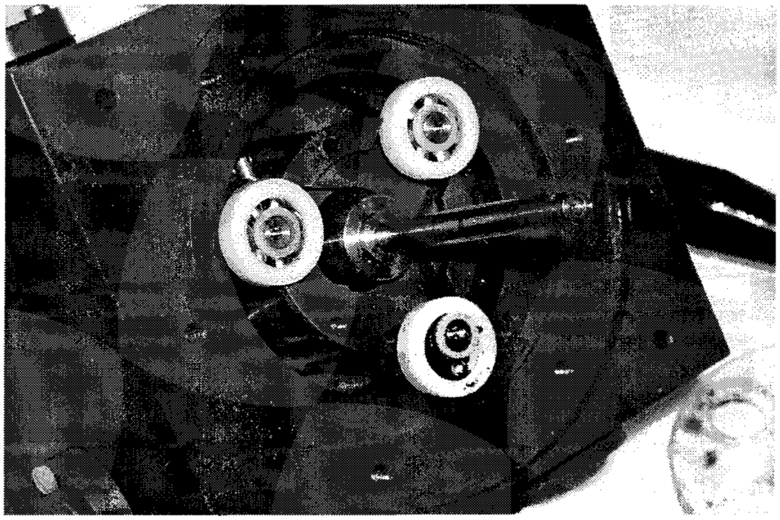

Figure 3.8: The compressor was dismantled to replace a bearing that overheated when it was operated at too high of a rotation rate.

it into a spherical glass storage cell. The glassware and compressor of the gas manifold are immersed in the magnetic field $\mathbf{B}_0$.

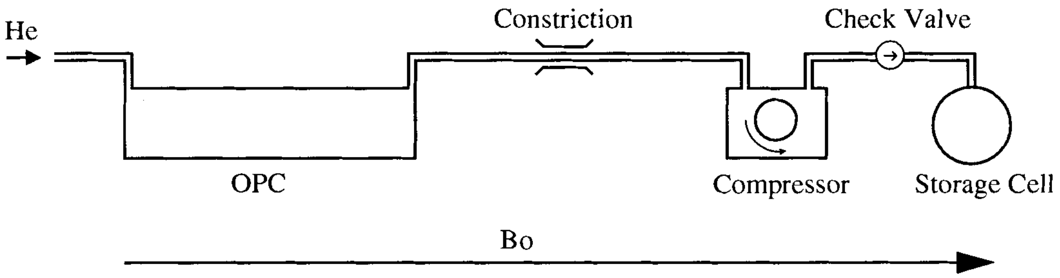

Figure 3.9: A simplified schematic diagram showing the gas flow path through the glassware section of the gas-handling manifold.

Chapter 4

Optical Pumping Cell and Laser Optics

This chapter describes the discharge circuitry, the laser, and the optical components used to carry-out MEOP in the optical pumping cell. These components of the MEOP station are directly involved in the optical pumping of ^{3}He.

4.1 The Optical Pumping Cell and the Discharge Coil

MEOP takes place as ^{3}He flows through a cylindrical borosilicate glass cell that is placed near the center of the B_0 coil, as shown in Fig 3.2. The optical pumping cell (OPC) was fabricated by fusing two borosilicate optical flats (thickness = 0.3 cm, diameter = 5.1 cm) to the open ends of a borosilicate tube (length = 28.0 cm, diameter = 5.1 cm, thickness = $\sim$0.1 cm). The inlet and outlet valves of the OPC are borosilicate vacuum-backed single bore oblique stopcock valves. Borosilicate tube (0.25$''$ outer-diameter, 0.20$''$ inner-diameter) connects the valves to the cylinder walls at opposite ends of the OPC, as shown in Fig. 4.1. The OPC is coupled to the MEOP station glassware with ground glass ball joints so that it can be removed from the system when necessary.

A 24-turn coil of 14 gauge copper wire wound around the circumference of the OPC (see Fig. 4.1) is used to ignite the low-power discharge for optical pumping and the high-power discharge for cell cleaning. By running an AC current through the 24-turn coil electromagnetic fields are generated throughout the volume of the OPC, ionizing the atoms and consequently igniting a discharge. The discharge is necessary for optical pumping as it acts to populate the ^{3}He excited states, and in particular the metastable 2^3S_1 state. The field

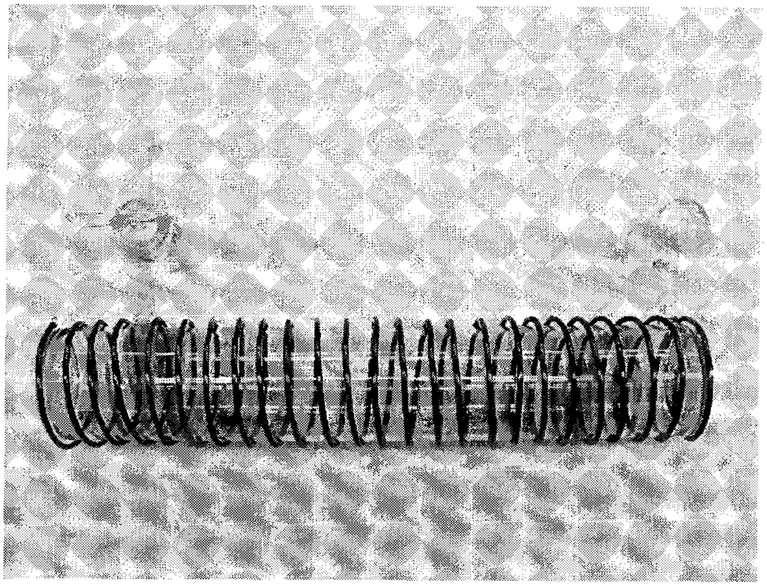

Figure 4.1: A photograph of the optical pumping cell. The wire wrapped around the cell is the RF discharge coil.

strengths near the cell walls are larger than at the cell center because of the solenoid design of the coil. There are other coil designs that provide better optical pumping conditions, however the 24-turn coil design was still implemented because the large electric fields it produces are very useful for cell cleaning, allowing the coil to serve in both optical pumping and cell cleaning procedures.

A resonant circuit, shown in Fig 4.2, was used to generate the high voltages across the 24-turn coil that are necessary to ignite the ^{3}He discharge. The 24-turn coil is represented by the inductor L_2. The inductances L_1 and L_2 have values of 0.35 μH and 7.23 μH, respectively. The two capacitors C were set at 330 pF so that the resonant frequency was of order several MHz. The resonant frequency of the RF discharge circuit is given by

$$f_o = \frac{1}{2\pi}\sqrt{\frac{2}{(L_1+L_2)C}} \tag{4.1}$$

which gives a resonant frequency of 4.5 MHz. A function generator was used to produce an sinusoidal emf at this frequency that is amplitude modulated at 100 Hz to a depth of 30%. The emf is amplified and is used to generate a current in the resonant circuit. The light

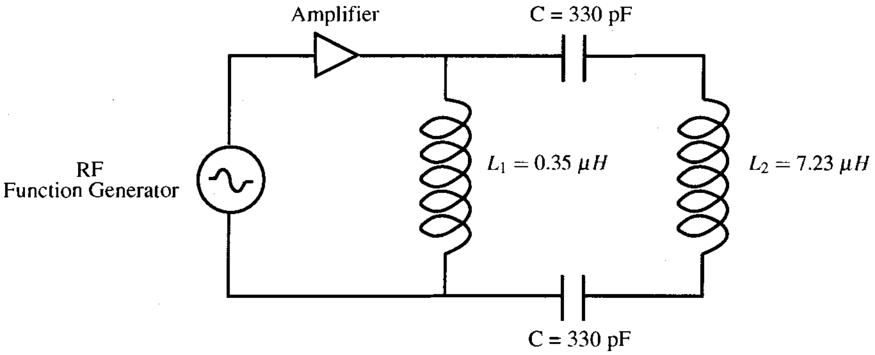

Figure 4.2: The RF resonant circuit used to ignite and maintain the discharge in the OPC. The RF resonant circuit is used to maintain the weak discharge during optical pumping and run the high-power discharge required to clean the OPC walls.

emitted from the helium discharge can be used to monitor the optical pumping conditions. However, this light is not very intense during the low-power discharge used during optical pumping and the 100 Hz modulation is used as reference frequency.

As mentioned previously, the 24-turn coil and resonant circuit can also be used to clean the OPC. However, OPC cleaning requires much larger field strengths to be generated near the cell walls than those needed for a MEOP discharge. A high power amplifier is used to deposit roughly 20 times more power in the OPC than what is typical for a low-power discharge. The large fields act to increase the kinetic energy of the helium ions. Some of this kinetic energy is transfered to thermal energy when the helium atoms collide with the cell walls. This increase in thermal energy effectively loosens impurities that have adsorbed to the walls. Overall, the increased kinetic energy of the colliding atoms combined with the increased thermal energy of the cell walls help to dislodge impurities from to the OPC walls.

4.2 The Laser and the Laser Optics

A 2 W Keopsys tunable ytterbium fiber laser (KPS-BT2-YFL-1083-20-FA-COL) is used to optically pump the $2^3S \rightarrow 2^3P$ transition. The laser emits linearly polarized 1083 nm light and is constructed such that the 1083 nm light can be fine-tuned to one of the nine allowed

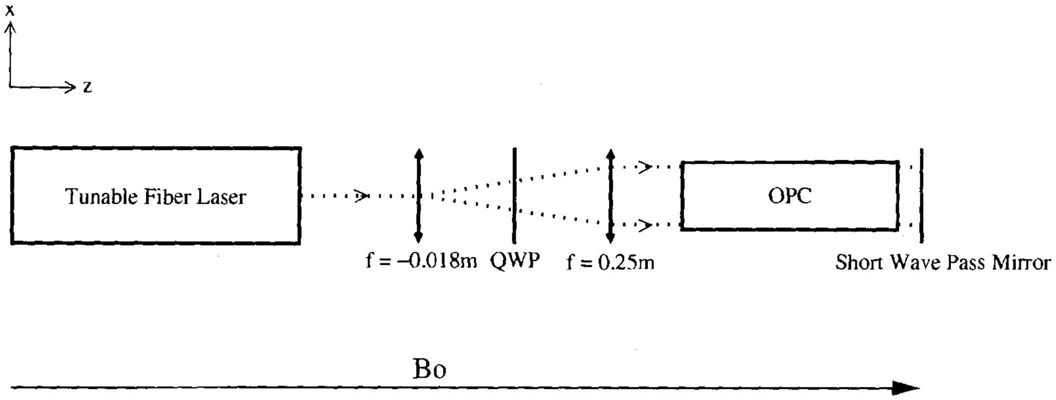

Figure 4.3: The linearly polarized 1083 nm light from the laser passes through a diverging lens, followed by a QWP and a finally converging lens. The light transmitted through the OPC is a circularly polarized parallel beam.

transitions for $m_f = +1$ (see $C_1 - C_9$ in Fig. 2.5). The spectral width of the laser is of order 2 GHz which has been designed to roughly match the Doppler width of the helium emission lines at room temperature (the Doppler full width half maximum for ^{3}He for $T = 330$K is 1.98 GHz) [30].

The linearly polarized laser light passes through a series of optical components to produce a parallel beam of circularly polarized light. The width of the beam was adjusted to be approximately equal to the OPC diameter. The laser and optics are mounted in a cage assembly that maintains their relative alignment. The laser light first passes through a diverging lens (diameter = 0.5 cm, f = -1.8 cm), a quarter wave plate (QWP) and finally through a converging lens (diameter = 5.1 cm, f=25 cm) as shown in Fig. 4.3. To maximize transmission efficiency the QWP and lenses are anti-reflection coated at 1083 nm. The optical components have been arranged such that the parallel beam of circularly polarized light is transmitted through the gas contained in the OPC and is then reflected back through the gas by a mirror that is reflective at 1083 nm light but transparent at 670 nm . The mirror is transparent at 670 nm because, as will be discussed shortly, this light is used to monitor the nuclear-spin polarization in the OPC. The mirror is used because reflecting the circularly polarized light back through the OPC is a simple method to double the optical absorption path.

The tuning of the laser is usually adjusted to optically pump the C_8 transition, as it has been shown that pumping C_8 (along with C_9) gives rise to the highest pumping efficiency [14]. The tunability of the fiber laser is achieved by changing the mechanical strain on a Bragg grating applied by a piezoelectric crystal. The piezovoltage across the crystal is controlled manually using a dial on the front panel of the laser. To adjust the tuning of the laser a silicon photodetector is used to monitor the 1083 nm emission of the helium discharge. The photodetector (ThorLabs DET110) is sensitive wavelengths of 350 - 1100 nm and is coupled with a 1000 nm long pass filter (ThorLabs FEL1000). Overall, this combination is sensitive to light at wavelengths between 1000 and 1100 nm. In an effort to ensure that the 1083 nm light collected by the photodetector is emitted by the helium discharge and is not the laser light, the photodetector is placed at a right angle to the direction of the laser light propagation. The laser is tuned to the desired absorption line ($C_1 - C_9$) by maximizing the photodetector current. The voltage across the photodetector was measured using a lock-in detector with the 100 Hz modulation of the RF discharge as a reference frequency. This voltage is plotted as a function of the piezovoltage across the Bragg-grating of the Keopsys fiber laser as shown in Figure 4.4. The C_8 and C_9 transitions are easily resolved because the energy difference between these two transitions is 6.7397 GHz which signifcantly larger than the 2 GHz spectral width of the laser [14]. The lines $C_1 - C_7$ are not clearly resolved because at low fields, the energy differences between these states are comparable to the spectral width of the laser.

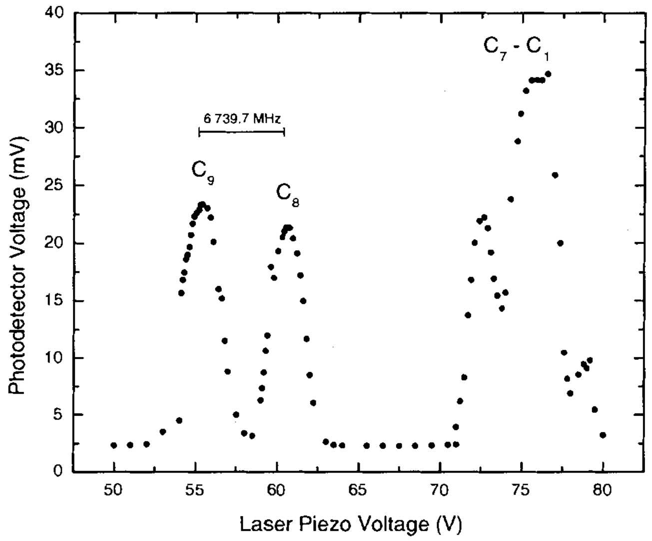

Figure 4.4: The intensity of 1083 nm light emitted from the ^{3}He discharge plotted as a function of the piezovoltage applied across the Bragg-grating of the fiber laser. The piezovoltages with high 1083 nm emissions correspond to the $2^3S_1 \rightarrow 2^3P$ transitions $C_1 - C_9$.

Chapter 5

Ancillary Equipment

Chapters 3 and 4 described all of the equipment necessary to hyperpolarize and compress ^{3}He. This chapter describes several pieces of ancillary equipment that are used to monitor nuclear-spin polarization during hyperpolarized gas collection (see Fig. 5.1). Specifically, an optical spectrometer that is used to monitor the optical emission spectrum of the discharge, a polarimeter that is used to infer nuclear-spin polarization from the optical polarization of light emitted from the discharge, and an NMR system that is used to monitor the total magnetic moment of hyperpolarized gas collected in the storage cell will be discussed. This chapter will introduce each piece of equipment, present the physics relevant to its operation, and describe its implementation.

5.1 The Spectrometer

The optical emission spectrum of the OPC discharge is used to monitor the purity of the helium gas and identify the source of any contamination. One channel of a dual-input spectrometer (Ocean Optics SD2000) equipped with a CCD detector is used to observe and record the optical emission spectrum for wavelengths from 200 - 860 nm. Ideally the emission spectrum of the OPC discharge should contain only lines associated with helium. However, because of airleaks and outgasing, other gases that diffuse into the OPC give rise to additional atomic and molecular emission lines. Ultimately, these contaminants have a detrimental effect on the ^{3}He nuclear-spin polarization. The spectra of common OPC contaminants are presented in this section.

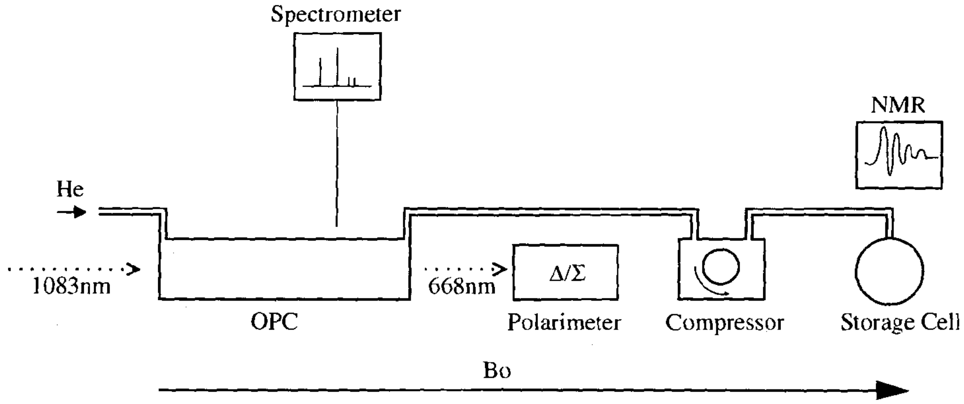

Figure 5.1: A simplified schematic diagram of the MEOP station showing the ancillary equipment.

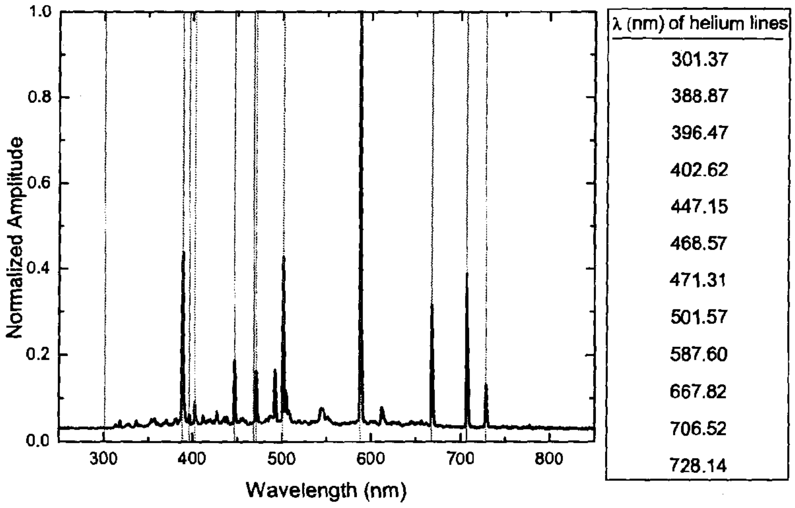

Figure 5.2: The optical emission spectrum from a helium discharge in a clean OPC. The high intensity helium emission lines are indicated by vertical lines and their corresponding wavelengths are listed on the right [49].

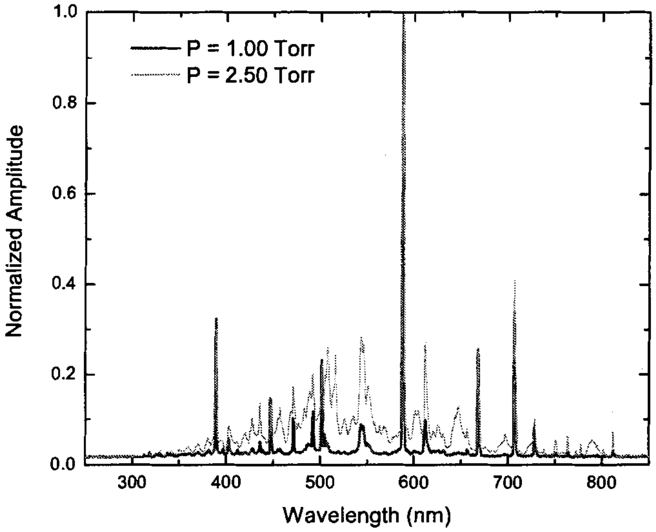

Figure 5.3: The relative intensities of the non-helium lines increase with increasing pressure. This figure shows spectra for helium discharges at pressures of 1.00 and 2.50 Torr.

An example of the optical emission spectrum from 1 Torr of helium, when the OPC walls are clean and the gas is free of contaminants, is shown in Fig. 5.2. The helium lines are indicated by vertical lines drawn on top of the spectrum, and are listed by wavelength to the right [49]. Because the line intensities increase with discharge strength and are pressure dependent, the line with the highest intensity, at 587.6 nm, is used to normalize the amplitudes of the other emission lines. The discharge strength increases the absolute intensities of the emission lines with no change in the relative intensities. For pressures below 1 Torr the intensities of non-helium lines are minimal (intensities are <0.05 relative to the 587.6 nm line for $P = 1.0$ Torr) and the discharge appears pink. As the pressure increases, the relative intensities of non-helium lines increase and the discharge appears blue. This change is evident in Fig. 5.3 which shows the emission spectrum for helium at two different pressures. The 2.5 Torr data shows the increased relative intensities of non-helium lines. Despite these pressure-dependent changes in the emission spectrum, the OPC walls are still "clean" and the gas is free of contaminants. Figures 5.2 and 5.3 are both examples of ^{3}He spectra that

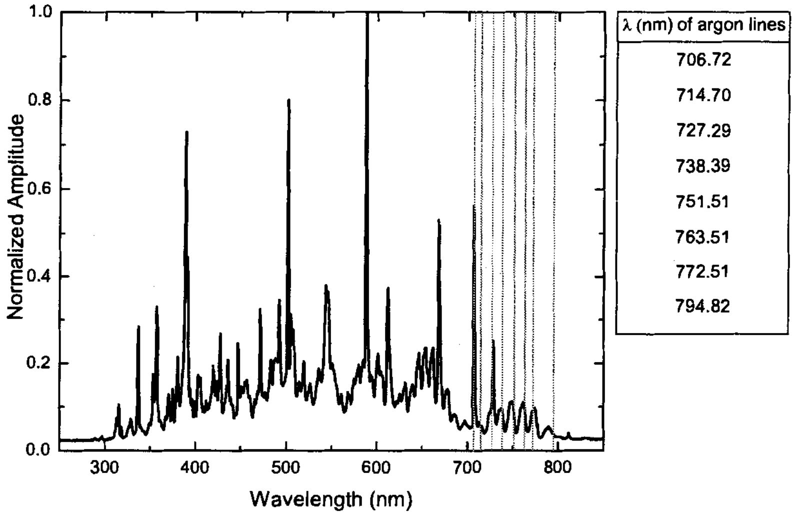

Figure 5.4: The optical emission spectrum of the discharge in the OPC when there is a small amount of air in the gas. The helium lines are still present, but there are several series of additional lines. The series of lines between 700 and 800 nm have been identified as argon lines which are indicated by vertical lines in the spectrum and their wavelengths are listed on the right. These argon lines are used to identify an airleak in the OPC.

correspond to good optical pumping conditions. Identifying the Ar lines as the signature of an airleak spectrum has been very useful for monitoring the system for unwanted air contamination (upstream of the compressor) during the hyperpolarized ^{3}He collection process. An example of an optical emission spectrum when some air has entered the OPC is shown in Fig. 5.4. Air consists primarily of N_2 and O_2 (78.08 % and 20.95 % by volume) and only a small amount of Ar (0.93 % by volume). Despite the minute quantity of Ar present in air, the Ar emission lines were clearly identifiable in the optical emission spectrum of the discharge. The Ar lines are indicated in Fig. 5.4 by vertical lines drawn over top of the spectrum and are listed by wavelength to the right [49]. A leak detector was used to estimate the leak rate of a faulty weld, and revealed that rates as low as 1×10^{-7} atm·cm^2/s are readily detected if the Ar lines are monitored. The ground-glass ball joints used to connect

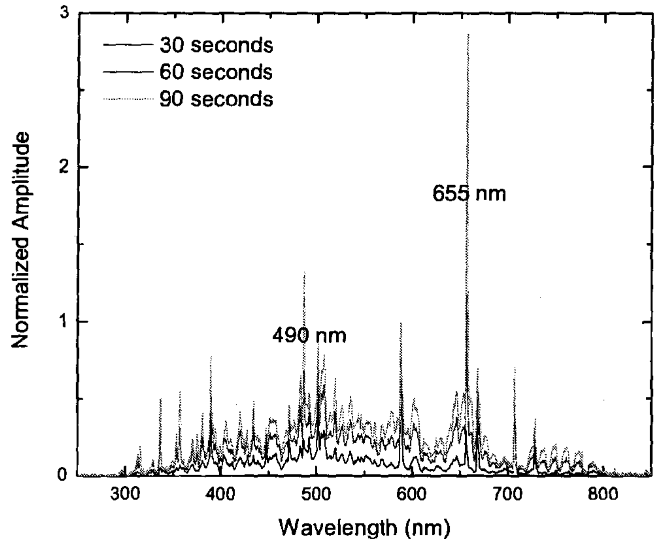

Figure 5.5: The optical emission spectrum of the OPC discharge when impurities from the outgasing of the Masterflex C tubing are allowed to enter the OPC. This contamination is most clearly identified by two intense lines, one at 490 nm and the other at 655 nm. The discharge spectrum was recorded at 0, 30 and 60 seconds after the compressor inlet valve was opened, revealing the progressive contamination of the OPC.

the OPC to the glass gas-handling manifold are the most frequent source of airleaks. These leaks can be remedied by cleaning and regreasing the ball joints.

The optical emission spectrum associated with impurities from outgasing of the Masterflex C tubing has also been identified. Identifying this spectrum has been useful because these contaminants quench the lifetime of helium atoms in the 2^3S_1 state and thus has a detrimental effect on the nuclear-spin polarization. Figure 5.5 shows an example of several emission spectra when impurities associated with the Masterflex C tubing were allowed to enter the OPC. These spectra are most easily identified by the presence of two very intense emission lines at 490 nm and 655 nm.

The optical emission spectra shown in Figs. 5.2 and 5.3 are examples of spectra obtained when the OPC walls were clean enough to conduct MEOP. However if either an airleak

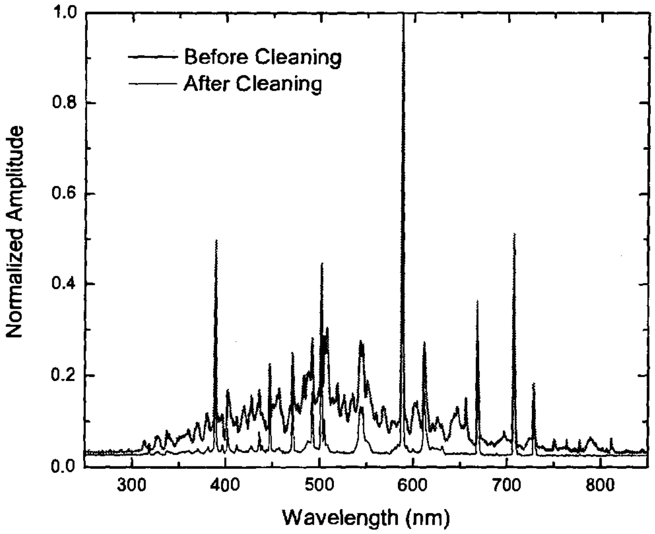

Figure 5.6: The optical emission spectrum for a low-power helium discharge was recorded before a cleaning procedure. After a high-power discharge was run for 3 min, the helium was pumped out of the OPC for ~20 min. Finally, fresh helium was admitted to the OPC and the optical emission spectrum was recorded again for a low-power discharge.

(Fig. 5.4) or a Masterflex C (Fig. 5.5) emission spectrum is observed, the OPC will need to cleaned before ^{3}He can be polarized by MEOP again. This is because when impurities enter the OPC, some will adsorb to the walls and need to be removed to regain good optical pumping conditions.

The OPC is cleaned by igniting a high-power discharge in 1 Torr of gas (^{3}He or ^{4}He) for several minutes. The optical emission spectrum of the OPC discharge is used to monitor the cleanliness of the OPC walls before and after each cleaning process. The high power discharge is ignited using the RF resonant circuit discussed in Section 4.1. This discharge deposits roughly 20 times more power in the OPC than the low-power discharges discussed up to this point. Thus the field strengths within the OPC are increased which in turn increases the kinetic energy of ions in the discharge. This increased kinetic energy helps to dislodge impurities from the OPC walls during collisions. Some energy is dissipated during collisions and warms the OPC walls to temperatures of order 340 K which helps to somewhat ease the removal of the impurities. After several minutes have passed, while leaving the high-power discharge on, the OPC outlet valve is opened to the turbo pump via line C (see schematic of gas-manifold in Fig 3.6). After a couple more minutes the high-power discharge can be shut off, but the OPC should remain open to the turbo pump until the cell walls have cooled to room temperature. Depending on the extent of the OPC wall contamination, one or two iterations of the cleaning procedure just described should be sufficient to recover the cleanliness of the OPC walls and achieve a pure helium spectrum in the OPC discharge. The emission spectra before and after a single cleaning cycle have been included in Fig. 5.6 as a reference. The intensities of non-helium lines in the emission spectra after cleaning have decreased substantially, indicating that the cleaning procedure has removed impurities from the cell walls. The emission spectrum after cleaning shows that the OPC walls are suitably clean for MEOP.

5.2 The Polarimeter

The polarimeter provides an indirect measure of the ^{3}He nuclear-spin polarization by analyzing the degree of circular polarization associated with 668 nm line emitted from the helium discharge. This section will first explain the connection between the optical polarization of the 668 nm emission line and the nuclear-spin polarization of ^{3}He. The rest of the section will present the polarimeter design and describe how it is implemented in the MEOP station.

The 668 nm line of ^{3}He is emitted when electrons relax from the 3^1D_2 to the 2^1P_1 state, as depicted in Fig. 5.7. The 668 nm emission line of ^{3}He is a combination of both right and left circularly polarized light. As a result of conservation of angular momentum, the helicity of the light reflects changes of the quantum number m_f [16, 50]. The polarization P_{668} of the 668 nm line is defined as the ratio between the difference and the sum of the intensity of the left (σ_-) and right (σ_+) circularly polarized light:

$$P_{668} = \frac{\sigma_+ - \sigma_-}{\sigma_+ + \sigma_-} \ . \tag{5.1}$$

In the absence of electron-spin polarization in the 3^1D_2 state, the intensities of both right and left circularly polarized light will be equal and $P_{668} = 0$. However, if there is an electron-spin polarization in the 3^1D_2 state, unequal intensities of right and left circularly polarized light will be emitted and $P_{668} \neq 0$.

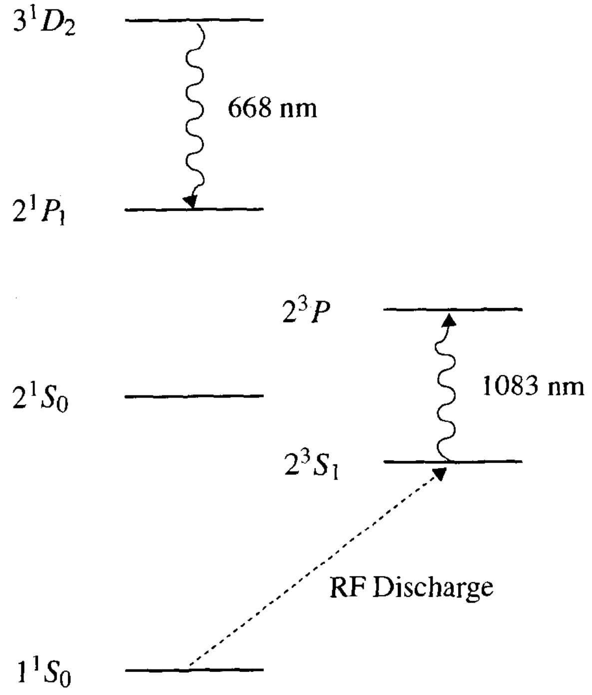

Figure 5.7: The 668 nm line is emitted when 3^1D_2 electrons relax to the 2^1P_1 state.

The functionality of the polarimeter relies on the fact that the nuclear-spin polarization of ^{3}He can be inferred from the polarization of the 668 nm light. This is possible because hyperfine coupling between the nuclear and electron-spin states give rise to an electron-spin polarization if there is a finite nuclear-spin polarization [50]. The correlation between the polarization of the 668 nm and the nuclear polarization has been theoretically modeled and measured by N.P. Bigelow, P.J. Nacher and M. Leduc [16]. Their work provides a theoretical model and measurements of the pressure-dependent ratio of the polarization of the nuclear-spins P to that of the 668 nm emission P_{668}. The ratios from the theoretical model for pressures relevant to this work have been included in the form of a graph and a table as shown in Fig. 5.8.

The polarimeter consists of basic optical components contained in two separate lens

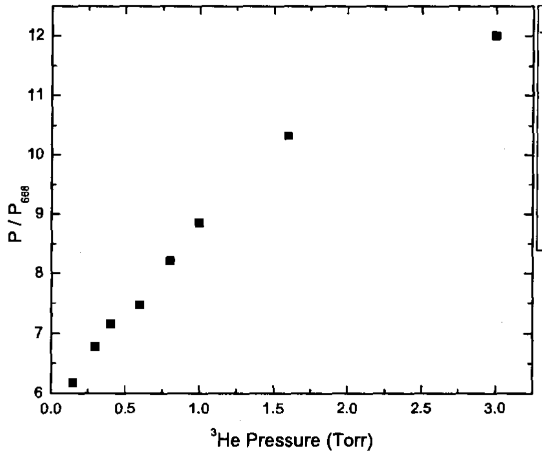

p (Torr)	P / P_{668}
0.15	6.18
0.30	6.78
0.40	7.16
0.60	4.47
0.80	8.21
1.0	8.86
1.6	10.33
3.0	12.0

Figure 5.8: The ratio of the nuclear-spin polarization to that of the 668 nm ^{3}He emission as a function of pressure [16].

tubes and a simple sum-difference circuit as shown in Fig. 5.9. One lens tube contains optical components arranged to transmit right circularly polarized 668 nm light, while the other lens tube transmits left circularly polarized 668 nm light. The light passing through each lens tube is focused onto the active region of a photodetector. The photodetector currents are fed into a sum-difference circuit which both adds (Σ channel) and subtracts (Δ channel) the photocurrents. The Δ channel is the difference between the intensities of right and left circularly polarized 668 nm light whereas the Σ channel is the sum. Because the Δ and Σ channel signals are proportional to the intensity of light incident on the photodetectors, they can be used to calculate P_{668}:

$$P_{668} = \frac{\sigma_+ - \sigma_-}{\sigma_+ + \sigma_-} = \frac{\Delta}{\Sigma} \; . \tag{5.2}$$

If there is no nuclear-spin polarization, P_{668} and hence the Δ channel will be zero. If there is a nuclear-spin polarization P_{668} and hence the Δ channel will be non-zero. The Σ channel should be approximately the same when the nuclear-spins are polarized and when they are not. This is because the helicity of the 668 nm light changes when there is a nuclear-spin polarization, but the total intensity of the emitted light stays approximately the same. To measure relative polarization, which is the most common application of this device, only the Δ channel of the polarimeter is necessary. However, the Σ channel is needed if one wants to extract the absolute polarization because it provides a measure of the total 668 nm light intensity.

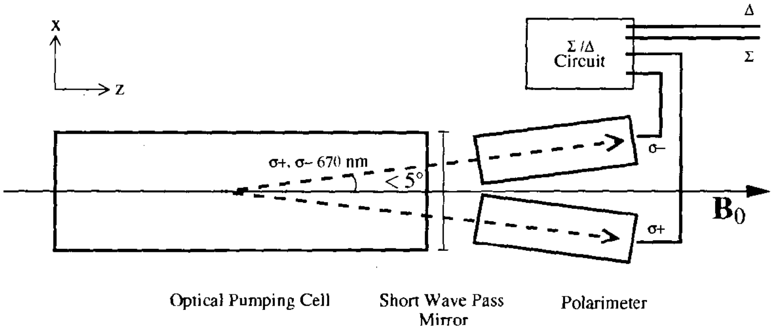

Figure 5.9: A schematic diagram of the polarimeter showing how it is placed behind the OPC cell to collect 668 nm light close to the quantization axis.

Each lens tube contains a quarter wave plate (QWP), a linear polarizer, a 668 nm interference filter (10 nm bandpass) and a converging lens (f = 25.0 mm) that focuses the transmitted light onto the photodetector located at the far end of the lens tube (see Fig. 5.10). The angle between the linear polarization axis and the QWP axes is 45°, an arrangement that transmits circularly polarized light. The relative angle between the two linear polarizers is 90° to ensure that each lens tube detects a different helicity of circularly polarized light. The polarimeter is placed such that the two lens tubes view light from the center of the OPC. The optical axes each make only very small angles ($\sim 5°$) with respect to the quantization axis. This angle must be kept small because the angular momentum transferred from the relaxing electrons to the light will lie along the quantization axis as defined by $\mathbf{B}_0$ (see Fig. 5.9).

To obtain measurements of absolute nuclear-spin polarization, the polarimeter was calibrated in two stages. The gain of the electronics associated with the sum and the difference channels of the electronics alone (photodetectors and sum/difference circuit) was calibrated first. Each photodetector was calibrated independently so that the signals observed on the Δ and Σ channels corresponded to the same intensity of light. For both photodetectors, the ratio between the signals from the Δ and Σ channel was found to be

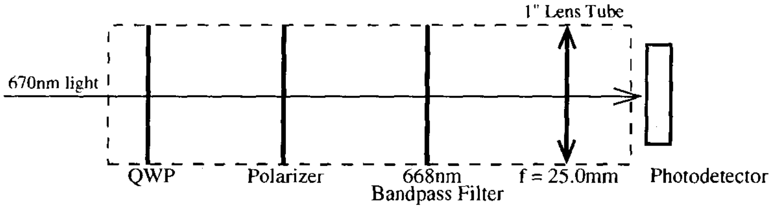

Figure 5.10: Each polarimeter lens tube contains a QWP, followed by a linear polarizer, a 668 nm bandpass filter and a converging lens that focuses 668 nm light onto the photodetector. The relative angle between the linear polarizers of each lens tube is 90° so that they detect circularly polarized light of opposite helicity.

$$\frac{\Delta}{\Sigma}=\frac{1}{19.7}\,. \tag{5.3}$$

The remaining optical components were then incorporated for the second stage of the calibration. A circularly polarized, collimated beam of light was first used to set the correct relative alignments of the QWP-linear-polarizer pairs. The combined transmission of the optical components in each lens tube was such that the ratio Δ/Σ as reported above did not change significantly ($< 1\%$). That is, the ratio between the gains of the two channels is still given by Eq. 5.3.

Phase-sensitive detection is used to measure the output of the Σ and Δ channels. As discussed in Section 4.1, the intensity of discharge light, and hence the intensity of the 668 nm light, is modulated at 100 Hz. The changes in the helicity of the 668 nm light were monitored by phase-locking to the modulated signal. Using this technique, the polarimeter was used to measure a nuclear-spin polarization of 6% in the OPC under optimal MEOP conditions.

The Δ channel of the polarimeter provides a relative measure of the nuclear-spin polarization and can thus be used to determine the characteristic time for the buildup of nuclear-spin polarization in the OPC. This can then be used to determine if any adjustments need to be made to the ^{3}He flow rate that was approximated in Section 3.5 to be roughly 9×10^{16} atoms/s. As a proof of principle, the build up of polarization in the OPC was measured when the OPC was sealed as well as when it was open to allow a continuous stream of ^{3}He to flow through the cell. Before the measurements were made, the OPC was cleaned using the high-power discharge. For the first measurement, the OPC was filled with ^{3}He to a pressure of 0.9 Torr and both the inlet and outlet valves were then closed. The laser was tuned to the C_8 transition and was operating at a power of 500 mW. Once the polarization had reached a maximum, the laser was shut off and the polarization very quickly decayed as a result of the strong electromagnetic fields produced by the discharge coil. The laser was then turned back on, and the build up of polarization was recorded as a function of time using the Δ channel of the polarimeter. For the second experiment, a continuous-stream of ^{3}He was passed through the OPC (at a pressure of $\sim$2 Torr) and the polarization was destroyed by placing a strong magnet in the vicinity of the cell. To compare the time required to achieve maximum polarization in each cell, the time dependence of the polarization during unperturbed optical pumping was approximated by

$$P(t) = P_{max}\left(1 - e^{-t/\tau}\right) \ . \tag{5.4}$$

While Eq. 5.4 ignores many aspects of the optical pumping process, it does provide a reasonable measure of the characteristic time for the buildup of nuclear-spin polarization. Because the polarization of the gas in the first experiment is not influenced by ^{3}He atoms entering and leaving the OPC as is the case in the second experiment, the corresponding time constant τ should be smaller. The time constants extracted from fits to the data reflected exactly this, with $\tau = 2.0 \pm 0.1$ s for the stationary gas and $\tau = 2.5 \pm 0.2$ s for the continuous stream.

To ensure that the polarization achieved during continuous-flow optical pumping is reasonably close to the maximum polarization, the residency time of the ^{3}He atoms must be comparable to the characteristic polarization time. Continuous-flow procedures conducted to this point have had flow rates of 9×10^{16} atoms/s which is the rate at which ^{3}He atoms enter and exit the OPC and hence can be used to calculate residency time of ^{3}He atoms as they flow through the OPC. For a flow-rate of 9×10^{16} atoms/s and a pressure of 1.5 Torr, the velocity of the atoms down the length of the cylindrical OPC is $\sim$2 mm/s. The flow rate sets the residency time $\sim$130 s.[1] Since the characteristic polarization time for a continuous stream of ^{3}He was 2.5 s, it can be concluded that the residency time corresponding to a flow-rate of 9×10^{16} atoms/s is far longer than necessary to achieve a reasonably high

---

[1] During this time, the atoms will have diffused the length of the OPC many times, resulting in uniform polarization along the length of the OPC.

nuclear-spin polarization in the gas. To improve the rate of hyperpolarized gas production, the flow rate should be increased to reduce the residency time to a value that is comparable to the characteristic polarization time.

5.3 The NMR System

A rudimentary pulsed NMR spectrometer is used with the MEOP station to verify that the gas collected in the storage cell is hyperpolarized. The NMR system relies on phase-sensitive detection of the small voltages induced across the receive coils. This section discusses the configuration of the B_1 coil, the receive coils, and the electronics comprising the NMR system.

The B_1 coil is intended to produce a uniform, oscillating magnetic field in the x-direction, perpendicular to $\mathbf{B}_0$. It is made of 20 parallel current-carrying wires arranged in a $\sin\phi$ distribution that spans the length of a cylindrical former (see Figs. 5.11 and 5.12). The $\sin\phi$ distribution is revealed in the angular spacing of the wires; the spacing corresponds to intervals of equal integrated axial surface current for wires carrying the same current [46]. The $\sin\phi$ distribution was used for the B_1 coil because it produces a uniform transverse field for an infinitely long cylinder [51]. The particular coil constructed for this work, however, has a finite length (about 10 cm) that reduces the field uniformity, as shown in Fig. 5.13. The field map shown in this figure reveals that the magnetic field strength drops to about 50% of its maximum value at either end of the B_1 coil. This results in the production of a non-uniform tip angle and reduces the NMR signal amplitude somewhat.

The NMR system is equipped with a set of four 100 turn, 1.7 cm radius, circular receive coils, each with a resistance of approximately 6 Ω. The arrangement of these receive coils acts to enhance the amplitude of the NMR signal while reducing the noise. The four receive coils are placed around the circumference of the cylindrical former with the plane of each receive coil oriented parallel to $\mathbf{B}_1$, in the xz-plane (see Fig. 5.12). This minimizes the flux of $\mathbf{B}_1$ through the receive coils, as depicted in Fig. 5.14. Before the exact configuration of the receive coils is described, it will be useful to first consider a magnetic moment that has been tipped into the transverse plane and is therefore precessing about $\mathbf{B}_0$. Figure 5.15 depicts the precessing magnetic moment at a particular instant in time when the moment points along the positive y-axis. Because the sign of the magnetic flux is important to this

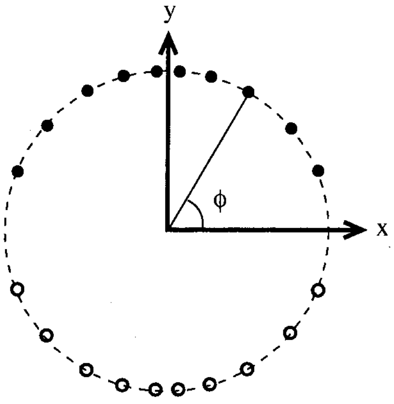

Figure 5.11: A schematic diagram showing the $\sin\phi$ distribution of the B_1 coil used in the MEOP station NMR system. The circles indicate the positions of the current carrying wires. The solid circles indicate current flow in the opposite sense as the open circles. The B_1 coil is used to generate a magnetic field in the x-direction and has a magnet constant of 0.5 μT/A.

discussion, a qualitative sketch of two of the magnetic field lines has been included in this figure. Notice that if the coils were all wound in the same sense, the magnetic flux through the top and bottom coils would have the opposite sign of that through the two side coils. To avoid this, the receive coils are connected in series such that the two coils on the top and bottom are counterwound with respect to the coils on the sides, as indicated by the $+$ and $-$ signs in Fig. 5.15. This configuration increases the emf induced by a precessing magnetic moment located at the geometric center of the coils. The total signal from the four receive coils is larger than that of one receive coil because the precessing magnetic moment induces a flux of the same sense in all four coils. More importantly, the counterwinding of the coils acts to reduce the NMR signal noise caused by homogeneous time-varying magnetic fields.

To ensure the small changes in flux through the receive coils are detected, two separate techniques are used to filter out noise. The first technique involves making a differential measurement. This is carried out by first measuring the emf across the receive coils in pairs. One measurement is made across two of the coils to ground while the other measurement is made from ground across the two other coils (see the upper left corner of Fig. 5.16). The two signals are then fed into two separate channels of a pre-amplifier (Stanford Research

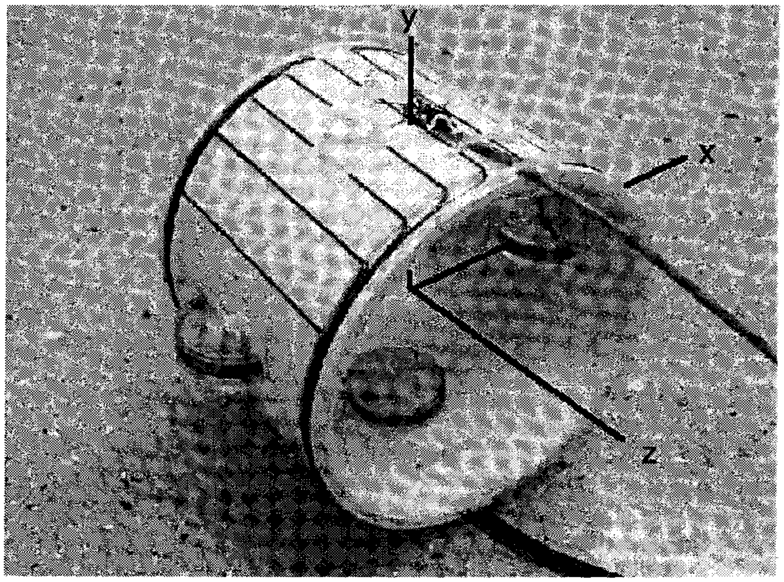

Figure 5.12: A photograph of the B_1 and receive coils used to conduct NMR experiments on the hyperpolarized gas in the storage cell. The B_1 coils run the length of a cylindrical former and are arranged in a $\sin\phi$ distribution. The four receive coils are placed symmetrically around the circumference of the former.

Systems SR560). To obtain the total emf across all four coils, the difference between the two signals is measured. This differential measurement removes noise common to both signals after traveling the length of the transmission lines. The second technique is to connect a capacitor in parallel with the receive coils creating a resonant circuit (see Fig. 5.16).[2] The capacitance in the resonant circuit is 36 nF and the DC resistance of the coils is 24 Ω, placing the resonant frequency at around 20 kHz. The Q-value of the resonant circuit is thus about 5, making the receive coils sensitive to frequencies around 18-22 kHz. These two techniques combined, namely differential detection and bandpass filtering, act to reduce the overall noise amplitude and to filter the noise picked up by the receive coils.

Figure 5.16 is a schematic diagram of the quadrature-detection NMR system used to perform measurements on hyperpolarized ^{3}He in the storage cell of the MEOP Station. The components of the NMR system depicted in Fig 5.16 will be described by following

---

[2] The two diodes in parallel shown at the top of Fig. 5.16 are used to protect the pre-amplifier from overloading and play no role in noise reduction.

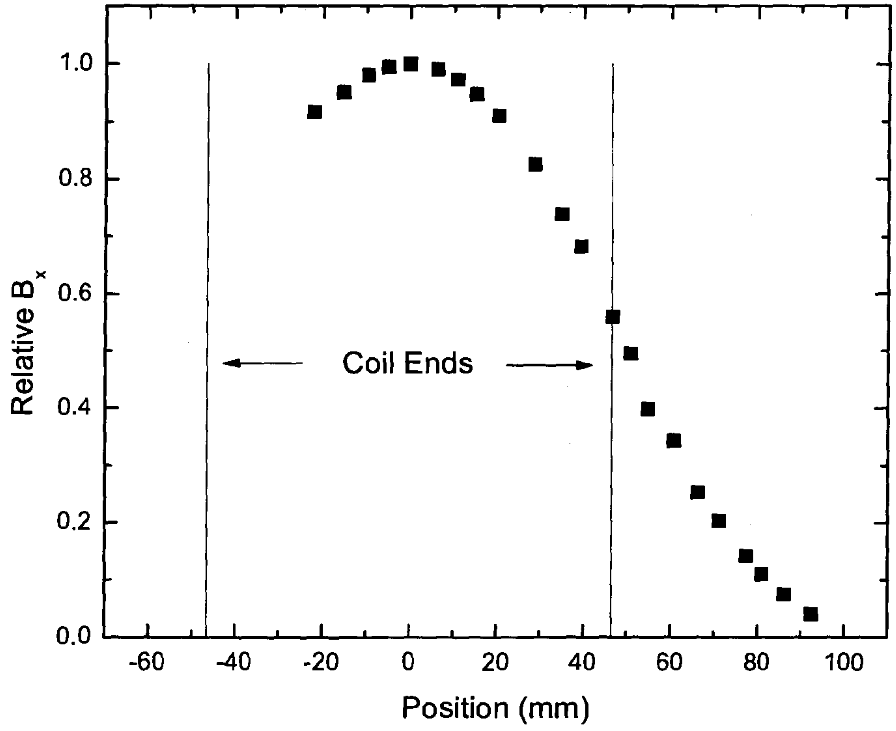

Figure 5.13: The relative magnetic field strength, measured with a probe coil, of the $\mathbf{B}_1$ plotted as a function of position along the z-axis.

the path of an electronic pulse that is used to trigger the $\mathbf{B}_1$ tipping pulse. A 3.5 V, 2 ms long pulse is used to blank the pre-amplifier and to trigger the function generator (DS345) that produces the B_1 pulse train. The function generator transmits a 20-cycle sinusoidal pulse train at the Larmor frequency (19.275 kHz for $B_0 = 6.0$ mT, $dB_z/dz = 170 \pm 5$ nT/cm, $dB_z/dy = 260 \pm 5$ nT/cm) to the B_1 coils. The pulse train is amplified by an audio amplifier (chosen for its low noise output in the frequency range of these experiments) which is placed in series with a 10 Ω resistor, a noise gate, and the B_1 coil as shown in the lower left corner of Fig. 5.16. The 10 Ω resistor increases the load seen by the amplifier and compensates for the small resistance of the B_1 coils (R = 0.16 Ω). The noise gate is a

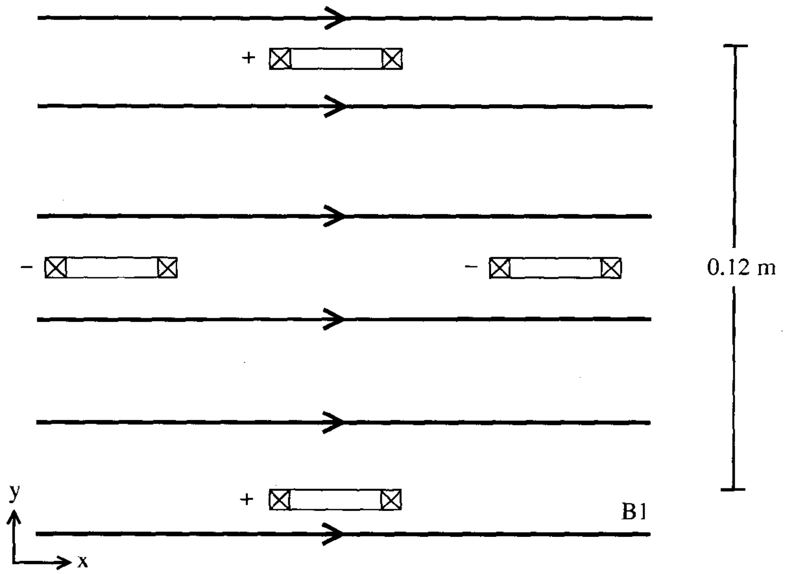

Figure 5.14: The planes of the NMR receive coils are oriented parallel to $\mathbf{B}_1$, indicated by solid lines pointing in the x-direction, to minimize the magnetic flux from the magnetic field during the $\mathbf{B}_1$ tipping pulse.

series of crossed diodes (1N914) that is only forward biased by large voltages (>2 V), which effectively eliminates low-level rumble from the amplifier from being transmitted to the coils. The noise gate is crucial in this experiment as it is responsible for reducing the noise induced in the receive coils to a level below the NMR signal. The voltage induced across the receive coils is then amplified by a factor of 1×10^4 using the pre-amplifier and fed into a lock-in detector (Stanford Research Systems SR810). The lock-in performs the quadrature-detection of the voltage induced across the receive coils. The lock-in output is the NMR signal and is viewed on an oscilloscope.

The NMR system was calibrated to measure the total magnetic moment of the hyperpolarized gas contained in the storage cell. The total magnetic moment $\mathbf{m}_{tot}$ of the hyperpolarized gas is directly proportional to the voltage induced across the NMR receive coils, and consequently to the NMR signal amplitude A

$$\mathbf{m}_{tot} = \kappa A \ . \tag{5.5}$$

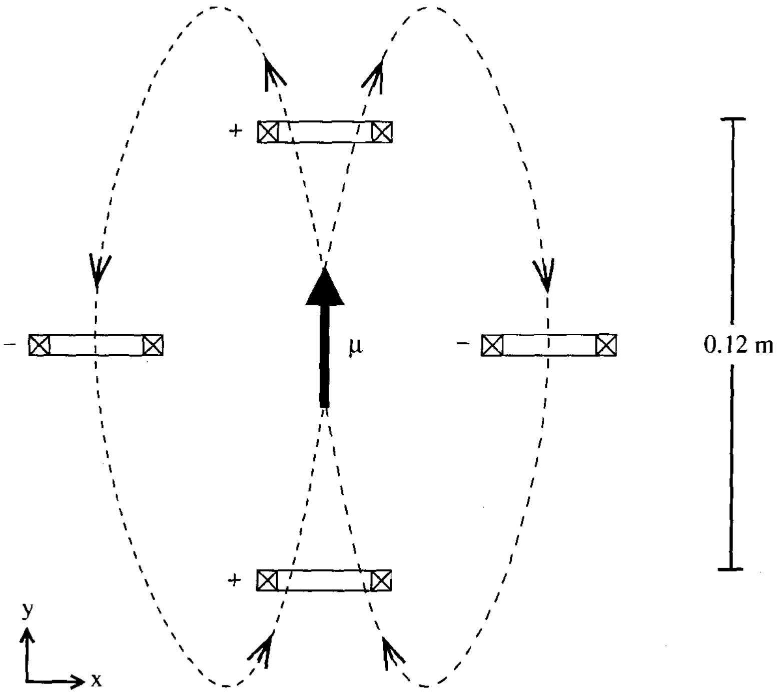

Figure 5.15: The four NMR receive coils are counter-wound in pairs which acts to reduce the inductively-detected noise while increasing the amplitude of the emf enduced by a precessing magnetic dipole located at the geometric center of the set.

The calibration constant κ was measured using a current-loop as a magnetic dipole where the magnetic moment m for n turns of wire carrying a current I and enclosing an area a is

$$m = nIa \ . \tag{5.6}$$

An AC current was driven through the loop at a frequency equal to the Larmor frequency. The NMR signal amplitude was recorded (using the oscilliscope) for different AC currents, and hence magnetic moments, to give a calibration constant $\kappa = 1.1 \pm 0.1 \times 10^{-8}$ J/T/mV. For an initial NMR signal amplitude A_0 recorded in mV using the oscilloscope, this yields

$$\mathbf{m}_{tot} = \kappa A_0 \ . \tag{5.7}$$

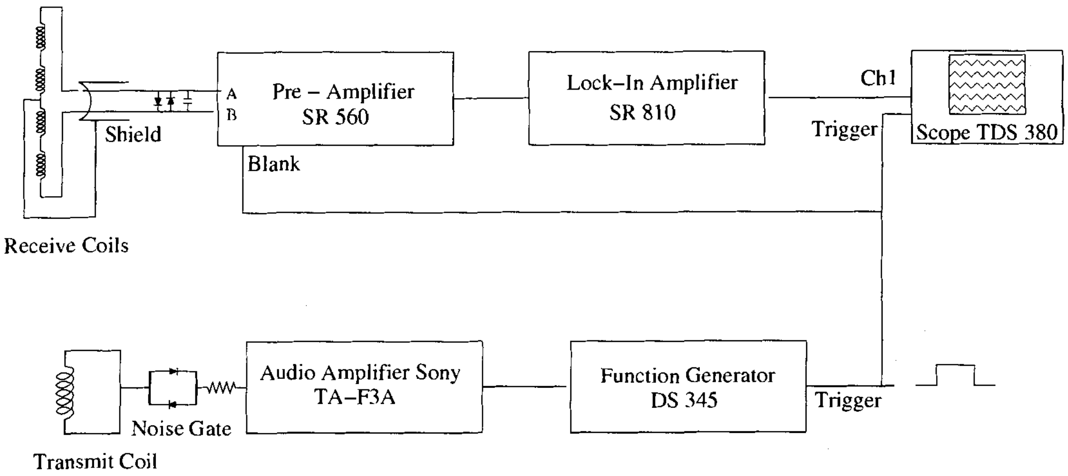

Figure 5.16: A schematic diagram of the quadrature detection NMR system used in the MEOP station.

The calibration constant corresponds to a pre-amplifier gain of 1×10^4, lock-in sensitivity of 200 mV and time constant 3 ms.

As an example of an NMR signal acquired using the system just described, Figure 5.17 shows an NMR signal for a $\pi/2$ pulse applied to 60 cm^3 of hyperpolarized ^{3}He at a pressure of 0.993 Torr (sealed test cell). As discussed in Section 2.5.1, because this is a low pressure sample, the NMR signal amplitude will decay exponentially with a decay constant T_2^*. Thus, the initial amplitude A_0 of the NMR signal can be extracted from an exponential decay fit to the data:

$$A(t) = A_0 e^{-t/T_2^*} + b \ . \tag{5.8}$$

For the NMR signal shown in Fig. 5.17 this amplitude was 300 ±5 mV which corresponds to a total magnetic moment of approximately $3.3 \pm 0.1 \times 10^{-6}$ J/T. The time constant T_2^* is the time it takes for the NMR signal amplitude to decay to 1/e of the initial amplitude, and is about 1.5 s. In this example the NMR signal amplitude was of order 300 mV for a pre-amp gain of 1×10^4 and a lock-in sensitivity of 200 mV (time constant, $\tau = 3$ ms). For these same settings the noise level is of order 34 mV and the SNR is of order 10.

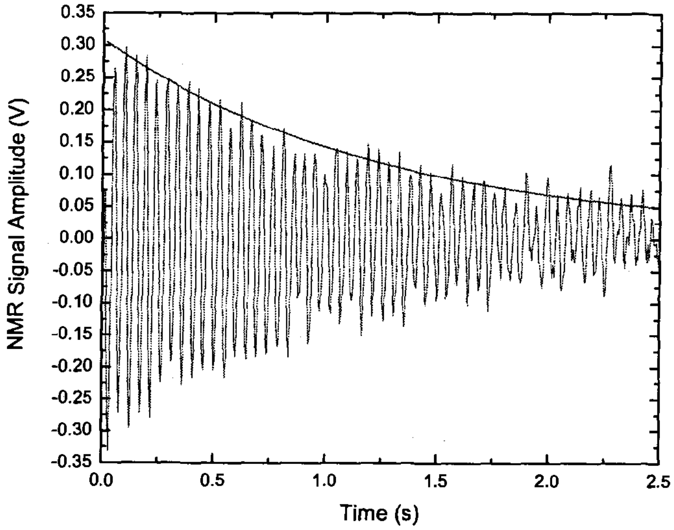

Figure 5.17: An NMR signal recorded by the MEOP Station quadrature detection NMR system. The NMR signal is from hyperpolarized ^{3}He atoms in a sealed test cell situated at the storage cell location after being subjected to a $\pi/2$ tipping pulse.

5.4 The Imaging Magnet

An imaging magnet was used to measure the total magnetic moment and the longitudinal relaxation time of hyperpolarized gas collected in the MEOP station. The imaging magnet was used for these measurements because it provided superior homogeneities in the both the main magnetic field $\mathbf{B}_0$ and in the tipping field $\mathbf{B}_1$ than the NMR system of the MEOP station. For these experiments, the receive coils described in Section 5.3 were used and were situated at the magnet centre. The $\mathbf{B}_1$ field was produced by two 30 cm coils that are typically used as the imaging magnet receive coils. A TecMag Apollo NMR system was used for phase-sensitive detection of the voltage induced across the receive coils. This system can be used to display the NMR signal in NTNMR units. The NTNMR units correspond to a voltage between +5 and−5 volts. A schematic diagram of the imaging magnet NMR system is shown in Fig. 5.18 and a more thorough description of the imaging magnet can be found in Ref. [52].

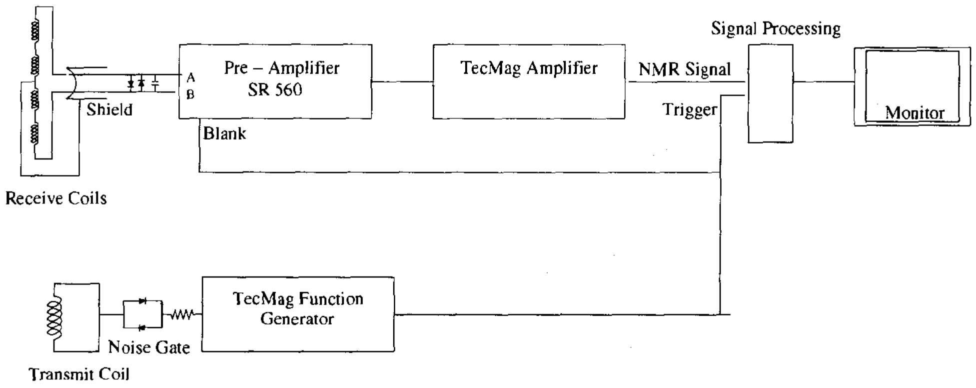

Figure 5.18: A schematic diagram of the NMR system used for the imaging magnet. In this system phase-sensitive detection is carried out by a TecMag Apollo NMR system which has been labelled as 'signal processing' in this diagram. The NMR signal is displayed on a computer monitor using a NTNMR software.

Chapter 6

Continuous-Flow Optical Pumping Procedure

This chapter is intended to serve as an operator's manual for the MEOP station. In it, I outline a step-by-step procedure for the collection of hyperpolarized ^{3}He using the continuous-flow optical pumping apparatus. This outline is followed by a description of and the motivation behind each of the steps. The valves shown on the schematic diagram of the MEOP station glassware that are relevant to this procedure have been assigned numbers (see Fig. 6.1) which will be used throughout this chapter. The procedure should be carried out in the order it is presented. In particular, the order of steps II-1 to II-6 should be followed exactly, as it was determined to effectively minimize contamination of the OPC and hyperpolarized ^{3}He from outgasing and potential airleaks.

6.1 Step-by-Step Procedure

I. **System Preparation**

The glassware should be under vacuum and valves $1-5$ should be closed, whereas valves $6-9$ may be either open or closed.

(1) **Check for airleaks.**

(2) **Turn on the getter.**

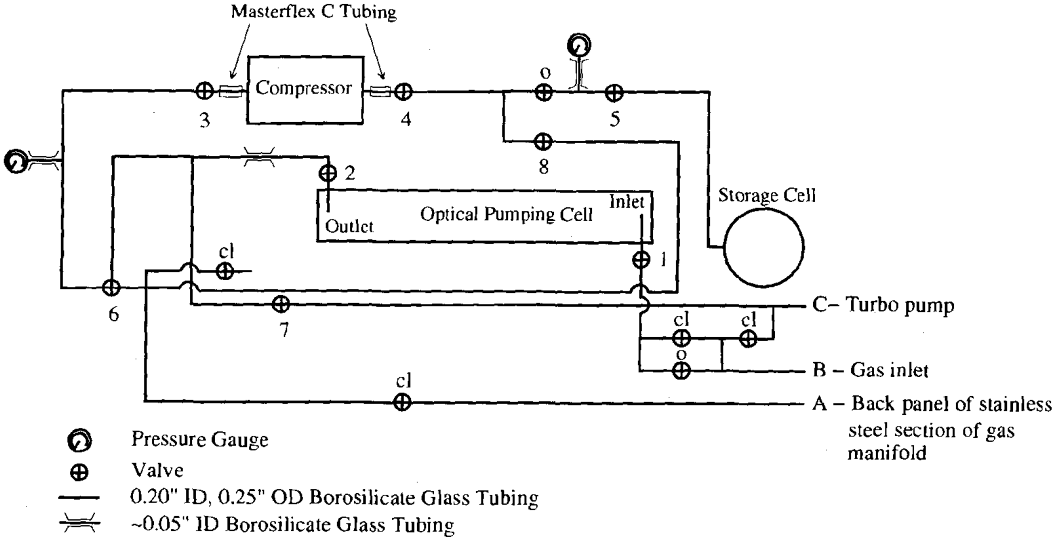

Figure 6.1: The glassware associated with the MEOP station: the numbering of the valves shown here corresponds to the step-by-step procedure of continuous-flow MEOP. Valves that are not used are shown here for reference, but are simply labeled with a 'cl' if they are normally closed and an 'o' if they are normally open. Ports A, B and C connect to corresponding ports of the stainless steel section of the gas manifold (see Fig. 3.5). The placement of the components is intended to reflect their physical location in the glassware section of the gas manifold.

(3) **Pump out any gas that has accumulated in lines C and B.**

(4) **Clean the OPC.**

(5) **Evacuate the compressor body, as well as the lines upstream and downstream of the compressor.**

(6) **Fill the storage cell with ^{4}He to a pressure of 100 Torr.**

(7) **Open line C, as well as the section between the OPC outlet and the compressor inlet to the turbo pump.**

(8) **Let ^{3}He into the OPC.**

(9) **Turn on the discharge, the laser, and the B_0, y- and z-gradient fields.**

(10) **Check the optical pumping conditions in the OPC.**

II. **Starting Continuous-Flow Optical Pumping**

Valves 1, 3, 4, 7 and 8 should be open, whereas valves 2 and 5 should be closed.

(1) **Close valves 3 and 8 and turn on the compressor.**

(2) **Open the storage cell valve (valve 5) and close valve 7.**

(3) **Open the OPC outlet valve (valve 2).**

(4) **Pass a *continuous* stream of ^{3}He through the OPC.**

(5) **Once the compressor has been running for $\sim$2 min, open the compressor inlet valve (valve 3).**

III. **Terminating Continuous-Flow Optical Pumping**

(1) **Shut off the discharge.**

(2) **Close the storage cell valve (valve 5).**

(3) **Close the OPC outlet valve followed by the inlet valve (valves 2 and 1, respectively).**

(4) **Close the compressor inlet valve followed by the compressor outlet valve (valves 3 and 4, respectively).**

(5) **Shut off the compressor.**

6.2 Detailed Procedure

I. **System Preparation**

The MEOP station must be checked for airleaks and evacuated of any build up of gas that may have accumulated while the system was not in use. Before starting this procedure, verify that the system is in standby mode, where valves $1-5$ are closed and valves $6-9$ may be either open or closed and the entire system is under vacuum. The system should be returned to this state when it is not being used.

(1) **Check for airleaks.**

Before commencing any gas-flow operation, the vacuum grease (Apiezon L) associated with the MEOP station glassware should be visually inspected for airleaks. The L-grease will appear streaky and opaque (rather than smooth and clear) when the vacuum seal has broken, and should be removed using toluene and reapplied after the toluene has evaporated. The L-grease on the ball joints of the OPC and storage cell will usually hold a seal for several weeks, while the L-grease on the stopcock valves will hold a seal for several months. When all of the ball joints and stopcocks are properly sealed, outgasing will typically cause an average pressure increase of 100 mTorr/min in the glassware volume (with valves 1-5 closed and valves 6 and 7 open) in the first 12 hrs after the turbo pump is shut off. The pressure can be monitored using either of the two pressure transducers coupled to the glassware or using the pressure gauge at the gas inlet (if line C is opened to line B of the stainless steel section of the gas-handling manifold. If the rate of pressure increase is greater than 100 mTorr/min, the system should be inspected for airleaks. Once the MEOP station is vacuum-tight, the system (with valves 1-5 closed) should be pumped out for several hours using the turbo pump (via line C).

(2) **Turn on the getter**

The getter should be allowed to warm up for an hour before any ^{3}He or ^{4}He is admitted. Air should *never* be let into the getter.

(3) **Pump out any gas that has accumulated in lines C and B.** At this point, any gas that has accumulated in lines B and C should be evacuated using the turbo pump. the pressure in these lines can be monitored using the two pressure transducers coupled to the glassware section of the gas-handling manifold.

(4) **Clean the OPC.**

The OPC should be cleaned before each experiment. The cleaning procedure is described in Sec. 5.1. Once the OPC has been cleaned, the OPC inlet and outlet valves (valves 1 and 2) should be closed.

(5) **Evacuate the compressor body, as well as the lines upstream and downstream of the compressor.**

Before every flow experiment, the Masterflex C lines upstream and downstream of the compressor (shown in Fig. 6.1) and the compressor body need to be evacuated. The lines upstream and downstream of the compressor are evacuated to remove accumulated impurities from the outgasing of the Masterflex C tubing and thus prevent contamination of the OPC. These lines are evacuated using the turbo pump via line C. Once evacuated, the compressor inlet and outlet valves (valves 3 and 4) should be closed to confine subsequent outgasing of the Masterflex C tubing to the volume immediately adjacent to the compressor. The compressor body placed under vacuum using a roughing pump which prevents the soft tubing from collapsing under a large pressure differential. The compressor body is backfilled to 30 Torr (absolute pressure) with nitrogen gas to help minimize the increase in temperature of the plastic races of the non-magnetic bearings as the compressor operates.

(6) **Fill the storage cell with ^{4}He to desired pre-pressure (100 Torr was used for experiments described in this thesis).**
The storage cell can now be evacuated and filled with ^{4}He to a pressure of 100 Torr via line C. This increase in pressure within the storage cell slows down the diffusion of the gas which in turn acts to increase T_1. After filling the storage cell, the storage cell valve (valve 5) is closed and the remaining ^{4}He in the stainless section gas manifold and MEOP glassware is removed using the turbo pump.

(7) **Open line C, as well as the section between the OPC outlet and the compressor inlet to the turbo pump.**
At this point the OPC, compressor and storage cell valves (valves 1, 2, 3, 4 and 5) should all be closed. To minimize the amount of outgasing from the Masterflex C tubing that accumulates before continuous gas flow begins, valves 3, 4, 6, 7 and 8 can now be opened to the turbo pump via line C.

(8) **Let ^{3}He into the OPC (pressures of 1 Torr were used for experiments described in this thesis).**
Before ^{3}He is let into the OPC, ensure that the valve between line B and the turbo pump is closed. This will prevent opening the ^{3}He line directly to the

turbo pump (not shown in Fig 6.1). The OPC inlet (valve 1) can be opened to admit ^{3}He from the getter into the OPC to achieve a pressure of 1 Torr. The pressure in the OPC is monitored using the pressure gauge coupled to line B of the stainless steel section of the gas-handling manifold (see Fig. 3.5). The OPC inlet valve can be left open.

(9) **Turn on the discharge, the laser, and the B_0, y- and z-gradient fields.** The RF discharge can be turned on using a 4.5 MHz sinusoidal voltage. The amplitude of this voltage needs to be modulated (a modulation frequency of 100 Hz to a depth of 30% was used for experiments discussed here). The laser can be turned on to the desired power output (an output power of 500 mW was used here). The DC currents used to generate the $\mathbf{B}_0$ and the y- and z- gradient fields were 2.45 A, 0.8 A and 1.4 A respectively.

(10) **Check the optical pumping conditions in the OPC.**

The ^{3}He that has just been admitted to the OPC will be used to tune the laser and verify that the optical pumping conditions are suitable for continuous-flow optical pumping. The low-power RF discharge can now be ignited and the main magnetic field ($\mathbf{B}_0$) and gradient fields can all be turned on. The ^{3}He emission spectrum from the discharge can be used to evaluate the OPC cleanliness (as discussed in Section 5.1). At this point, the emission spectrum should be that of pure helium. Prior to optical pumping, the laser must be turned on and tuned to either the C_8 or C_9 transition (as described in Sec. 4.2). The laser tuning may need to be adjusted and should be monitored throughout the procedure. The polarimeter is used to verify that a substantial nuclear-spin polarization is produced in the OPC. The zero of the polarimeter Δ channel can be checked by moving a strong permanent magnet into the vicinity of the OPC. The Δ channel of the polarimeter should change when the magnet is removed again, whereas the Σ channel should not change more than a few mV's. The ratio of the change in the Δ channel to the Σ channel voltage is used to quantify the optical pumping conditions, where a ratio of 0.1 is indicative of good conditions. If no change is observed in the Δ channel voltage, the ^{3}He is not being optically pumped and the laser tuning, QWP alignment, magnetic field and OPC emission spectrum should all be verified.

II. **Starting Continuous-Flow Optical Pumping**

The MEOP station has now been fully prepared and continuous-flow optical pumping can begin. Currently, valves 3, 4, 6, 7 and 8 should all be open to the turbo pump via line C, while valves 2 and 5 should be closed.

(1) **Close valves 3 and 8 and turn on the compressor.**

Valve 3 should now be closed to keep impurities from the Masterflex C tubing from diffusing into the OPC. For the same reason, the compressor should be running for $\sim$2 min before valve 3 is opened in step II-6. Valve 8 should be closed to direct gas from the compressor into the storage cell.

(2) **Open the storage cell valve (valve 5) and close valve 7.**

Before the OPC outlet valve is opened, valve 7 must be closed; otherwise the OPC will be opened to the turbo pump!

(3) **Open the OPC outlet valve (valve 2).**

The OPC outlet valve (valve 2) can now be opened. There should be no change in the intensity of the optical emission spectrum from the OPC. If either the Masterflex C outgasing impurity spectrum or an air spectrum is observed (see Figs. 5.4 and 5.5), the procedure will need to be terminated and, after rectifying the problem, the OPC will need to be cleaned again.

(4) **Pass a continuous stream of ^{3}He through the OPC.**

The needle valve on the gas manifold can now be opened slowly to admit ^{3}He to the OPC. The pressure can be monitored using the pressure gauge connected to line B of the stainless steel section of the gas manifold (see Fig. 3.5) and should not exceed 3 Torr. The needle valve must be left open to permit a *continuous* stream of ^{3}He to flow through the compressor. This helps to minimize contamination of the OPC by preventing backstreaming of impurities from the Masterflex C tubing.

(5) **Open the compressor inlet valve (valve 3).**

After the compressor has been running for at least two-minutes and the pressure in the OPC has reached 2-3 Torr, the compressor inlet valve (valve 3) can be opened to commence continuous-flow optical pumping of ^{3}He.

At this point, ^{3}He flows through the OPC, where it is hyperpolarized by MEOP. The hyperpolarized gas is then drawn into the compressor and pumped into the storage cell for approximately 10 min. The optical emission spectrum should be that of pure helium throughout the hyperpolarized gas collection period. Figure 6.2 shows the optical emission spectrum at the beginning and end of a typical hyperpolarized ^{3}He collection period. The non-helium lines of the emission spectrum recorded at 9.5 min are slightly more intense, but overall the spectra are very similar. When only slight changes in the spectra occur, as in the example shown in Fig. 6.2, the polarization of the gas in the OPC at the end of the collection period should be comparable to that at the start.

III. Terminating Continuous-Flow Optical Pumping

After 10 min, continuous-flow is terminated to prevent over-heating of the compressor bearings. To minimize relaxation of the hyperpolarized ^{3}He and the contamination of the OPC, the steps in this section should be followed exactly.

(1) **Shut off the discharge.**

(2) **Close the storage cell valve (valve 5).**

(3) **Close the OPC outlet valve followed by the inlet valve (valves 2 and 1, respectively).**

(4) **Close the compressor inlet valve followed by the outlet valve (valves 3 and 4, respectively).**

(5) **Shut off the compressor.**

NMR experiments can now be conducted on the collected hyperpolarized gas using the NMR system of the MEOP station, described in Section 5.3. Alternatively, the gas may be transported to another NMR system, such as the imaging magnet.

Typical NMR signals have been included in Figures 6.3 and 6.4 as references for SNR and T_2^* in the MEOP station. These NMR signals correspond to two consecutive tipping pulses with angles of 34° and 90°, respectively. They were detected with the equipment and settings provided in Section 5.3. Because of the short T_2^* (approximately 25 ms) and the detuning of the local oscillator frequency only a few oscillations are observed. The SNR

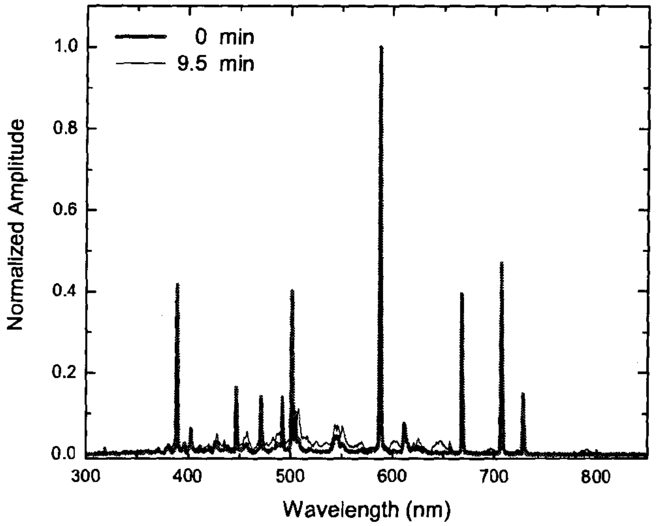

Figure 6.2: The ^{3}He emission spectrum before (0 min) and after (9.5 min) a continuous-flow MEOP operation. The intensities of the non-helium lines remain quite low after 9.5 min of continuous-flow through the OPC.

for the initial NMR signal of the 34° tipping pulse is approximately 10 whereas the SNR for the 90° tipping pulse is approximately 17.

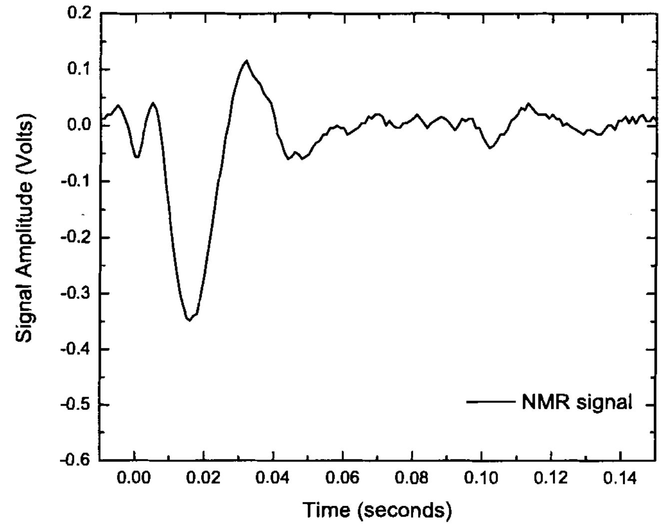

Figure 6.3: One phase of a NMR signal acquired in the MEOP station from ^{3}He in the storage cell. The tip angle was 34° and the gas pressure was 7 Torr.

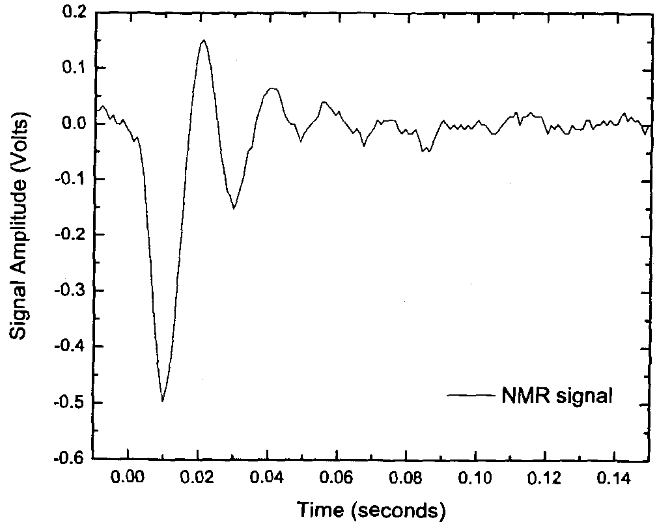

Figure 6.4: One phase of a NMR signal acquired from ^{3}He in the storage cell of the MEOP station. The tip angle was 90° and was applied after the tipping pulse corresponding the the NMR signal in Fig. 6.3.

Chapter 7

Preliminary Measurements and System Assessment

There are two preliminary measurements included in this chapter that characterize the compressed hyperpolarized ^{3}He and hence the performance of the MEOP station. The first measurement is of the total magnetic moment of the gas, which is important because it ultimately determines the magnitude of the NMR signal that can be obtained for a given set of experimental conditions. The second measurement is of the longitudinal relaxation time constant T_1 which can be used, in combination with the ^{3}He flow rate, to optimize the total magnetic moment of the collected gas. These measurements are used to asses the current status of the MEOP station. They are also used to deduce the some modifications that need to be made to the system so that it can be used to produce samples of hyperpolarized ^{3}He gas suitable for lung airspace MRI.

7.1 Total Magnetic Moment Measurement

The total magnetic moment can be used to characterize the performance of the MEOP station because it depends on the polarization achieved in the OPC and the relaxation of that polarization during subsequent compression, storage and transportation. As discussed in Section 5.3, the initial NMR signal amplitude A is directly proportional the total magnetic moment of the gas

$$m_{tot} = \kappa A \ . \tag{7.1}$$

The constant of proportionality κ corresponds to the gain factor of the NMR system and depends on several experimental parameters including: the configuration, area and number of turns of the receive coils, the Larmor frequency of the ^{3}He atoms and the gain of pre-amplifier. There are several methods that can be used to calibrate the gain factor of the NMR system of the imaging magnet. All involve measuring the NMR signal amplitude for a known magnetic moment. At high field strengths, this calibration is often conducted using the magnetic moment of a Boltzmann polarized water sample. This method works well because the geometry of the water sample can be made to mimic that of the hyperpolarized gas sample and this approach can ultimately be used to make measurements that do not depend on the absolute value of the tipping angle. However, this calibration method cannot be conducted at low field strengths because the Boltzmann polarization is very small and the total magnetic moment of the gas will produce an NMR signal that is below the noise threshold of the system. Instead, a current-loop was used to produce a magnetic dipole. The magnetic moment m of the current-loop can be calculated from the number of turns n, the current I and the area a of the loop

$$m = nIa \ . \tag{7.2}$$

The magnetic dipole of a current loop is an accurate representation of the total magnetic moment of the hyperpolarized gas in the spherical storage cell. When conducting this calibration the experimental conditions were mimicked as closely as possible as it was important that the gain factor was not modified. This was accomplished in part by driving an AC current at the Larmor frequency through the coil to prevent any damping of the signal amplitude due to filtering.

The NMR system of the imaging magnet (described in Section 5.4) was calibrated using a single-turn of copper wire ($r = 0.05$ mm) that was placed at geometric center of the NMR receive coils. The NMR signal amplitude was recorded for different magnetic moments by changing the amplitude of the AC current. The pre-amplifier gain was 1×10^4 and the NTNMR amplifier gain was 0%. The NMR signal amplitude was then plotted as a function of the magnetic moment of the current-loop, as given in Eq. 7.2, to extract the constant of proportionality $\kappa = 6.62 \pm 0.04 \times 10^{-11}$ J/T (where the NTNMR amplitude units have been dropped). This calibration can be used to measure the total magnetic moment from the initial NMR signal amplitude from a sample of hyperpolarized ^{3}He gas.

Hyperpolarized ^{3}He was collected in the storage cell using the experimental procedure described in Chapter 6. After the gas collection was completed, the currents of the y- and z- magnetic gradient fields, followed by the $\mathbf{B}_0$ field were ramped down. The storage cell valve was closed and the ^{3}He-^{4}He mixture (8 Torr and 101 Torr, respectively) was transported a distance of about 30 m in 1 min to the imaging magnet. During the relocation of the storage cell, the Earth's field provided the quantization axis for the nuclear-spins. The storage cell was placed at the center of the NMR receive coils, which were situated at the center of the imaging magnet. Once the storage cell was in position, the imaging magnet $\mathbf{B}_0$ field, followed by the gradient fields were ramped up. The hyperpolarized gas was then subjected to an $\alpha = 23^\circ$ tipping pulse. The component of the total magnetic moment that was tipped into the transverse plane, combined with the gain factor, determines the magnitude of the NMR signal. It is the initial amplitude of the NMR signal (included in Fig. 7.1) that corresponds to the transverse component of the total magnetic moment. The NMR signal $A(t)$ was fit to a function of the form

$$A(t) = A_0 \left[\frac{3\sin(t/\tau)}{(t/\tau)^3} - \frac{3\cos(t/\tau)}{(t/\tau)^2} \right] \cos\left(\frac{\omega'}{\tau} t - \phi \right) . \tag{7.3}$$

As discussed in Section 2.5.1, this function can be used to fit the amplitude of an NMR signal in a high pressure ($\geq$100 Torr) spherical sample of gas where the transverse decay time T_2^* is gradient-dominated. The amplitude A_0 extracted from the fit to the data in Fig. 7.1 was 340 $\pm$50 (in NTNMR units), which corresponds to a total magnetic moment of $5.8 \pm 0.8 \times 10^{-8}$ J/T.

In order to use this measurement of the total magnetic moment to evaluate the status of the system, it will be compared to the total magnetic moment that have been used to successfully image human lung airspaces. Other research groups have used 40 cc of 30-40% polarized ^{3}He at atmospheric pressure to conduct lung airspace MRI [6, 17, 37].[1] These samples involve roughly ten times the ^{3}He atoms collected in the storage cell during the

---

[1] Often, a buffer gas (^{4}He or N_2) is added to the hyperpolarized ^{3}He to create a sample at atmospheric pressure with suitable volume for inhalation (~300 cc).

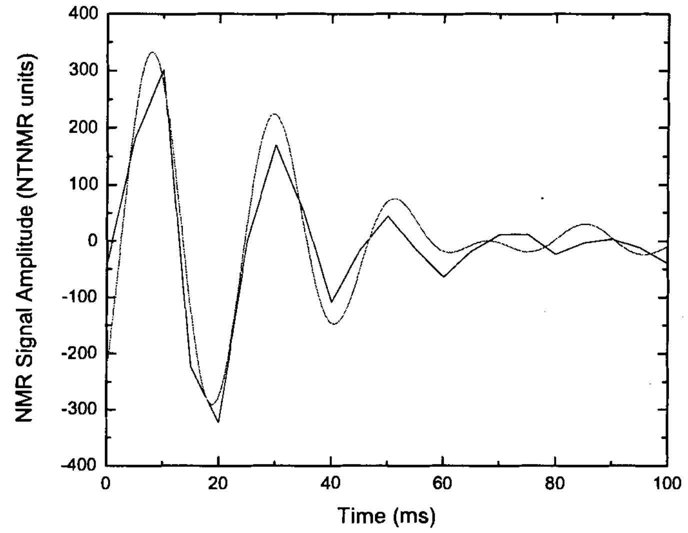

Figure 7.1: An NMR signal acquired in the imaging magnet from 8 Torr of hyperpolarized ^{3}He collected in the storage cell. A function of the form given in Eq. 7.3 was fit to the data in order to extract a reasonable estimate of the initial NMR signal amplitude. Here, the fit gave $A_0 = 340 \pm 50$ (in NTNMR units).

experiment described above. Hence the corresponding magnetic moment of these samples should be ten times that of the hyperpolarized gas collected in the storage cell. Using Eq. 2.52 and the magnetic moment of a single ^{3}He atom[2], the magnetic moment of these samples is calculated to be of order $\sim 1 \times 10^{-6}$ J/T. This is actually 15 times larger than the total magnetic moment of the sample produced in the MEOP station. Thus for 1/10 of the atoms, the total magnetic moment was 1/15 that of what is typically used for MR imaging of lung airspaces. This suggests that the polarization of the gas is adequate and that the focus of future modifications needs to be on increasing the total magnetic moment of the gas that is collected.

---

[2] $\mu_{He} = 1.0745 \times 10^{-26}$ J/T

7.2 T_1 Measurement

The T_1 measurement was carried out by using small tip angles to sample the magnetization over a suitable time interval. However, in order to extract the longitudinal relaxation time from the data, the losses that result from each tipping pulse must be corrected.

To understand how the correction is done, first consider a series of NMR signals that are recorded after a tipping pulse of known tip angle α. The NMR signal is a result of the precession of the portion of the magnetization tipped into the transverse plane M_{tr}

$$M_{tr} = M(t_i)\sin(\alpha) \tag{7.4}$$

where $M(t_i)$ is the longitudinal magnetization at time t_i just before the application of the tipping pulse. The longitudinal magnetization remaining after the tipping pulse is given by

$$M = M(t_i)\cos(\alpha)\ . \tag{7.5}$$

The total, longitudinal and transverse magnetization at the time of the tipping pulse t_i are depicted on left-hand side of Fig. 7.2. After the tipping pulse, the decay of the longitudinal magnetization is governed by Eq. 2.65 and at the time t_{i+1} of next tipping pulse, the longitudinal magnetization will have decayed to

$$M = M(t_i)\cos(\alpha)e^{\frac{-(t_{i+1}-t_i)}{T_1}}$$

and the tipping pulse will only tip

$$M(t_i)\cos(\alpha)e^{\frac{-(t_{i+1}-t_i)}{T_1}}\sin(\alpha)$$

into the transverse plane. By induction, the magnetization tipped into the transverse plane M_{tr} by the nth tipping pulse is then

$$M_{tr}(t_n) = M(t_n)\sin(\alpha) \tag{7.6}$$

$$M_{tr}(t_n) = M(t_1)\left[\cos(\alpha)\right]^{n-1}e^{\frac{-t_n}{T_1}}\sin(\alpha)\ . \tag{7.7}$$

By moving the $[\cos(\alpha)]^{n-1}$ to the left-hand side of Eq. 7.7 one obtains

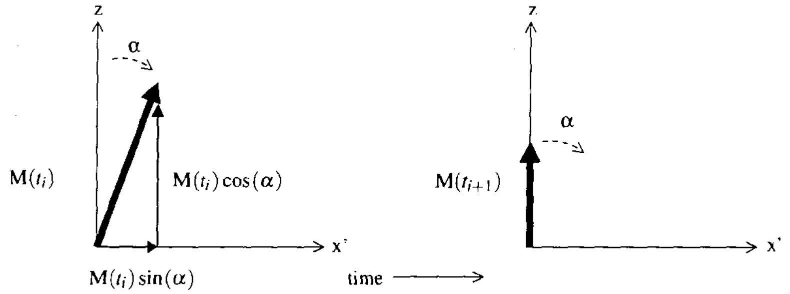

Figure 7.2: The NMR signal amplitude resulting from the application of a small tipping pulse α.

$$\frac{M_{tr}(t_n)}{[\cos(\alpha)]^{n-1}} = M(t_1)e^{\frac{-t_n}{T_1}}\sin(\alpha)\ . \tag{7.8}$$

Since $M(t_1)$ and $\sin(\alpha)$ are constant, the decay is governed by the longitudinal relaxation time.

For this measurement the hyperpolarized gas was collected and transported to the imaging magnet using the same procedure described in the previous section. T_1 was measured in the imaging magnet for a ^{3}He-^{4}He mixture (8 Torr and 101 Torr, respectively) sealed within the volume of the storage cell. A total of 6 tipping pulses were applied and the NMR signal corresponding to each pulse was fit to a function of the form given by Eq. 7.3. Since the NMR signal is directly proportional to the transverse magnetization, Eq. 7.8 can be used to extract the longitudinal relaxation time from the fit amplitudes. If the fit amplitude for the NMR signal corresponding to the i^{th} tipping pulse (applied at time t_i) is expressed as $A_0(t_i)$, then the corrected fit amplitude $A_0^c(t_i)$ is

$$A_0^c(t_i) = \frac{A_0(t_i)}{[\cos\alpha]^{i-1}}\ . \tag{7.9}$$

The corrected NMR signal amplitudes $A_0^c(t_i)$ are then plotted as a function of time as shown in Fig. 7.3. As expected, the NMR signal amplitudes decrease with time. However, now that the correction for tipping pulse losses has applied, the decrease in NMR signal amplitude should reflect the longitudinal relaxation rate. Consequently, the corrected NMR signal amplitudes were fit to another exponential decay

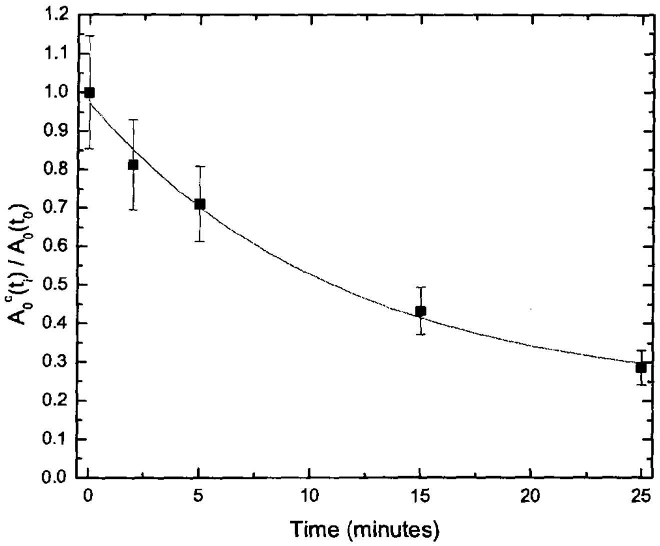

Figure 7.3: The NMR signal amplitude is plotted as a function of the time at which the tipping pulse was applied. A fit to a decaying exponential allows one to extract the longitudinal relaxation time T_1 of the hyperpolarized ^{3}He. Here T_1 is of order 17 min.

$$A_0^c(t_i) = A_0^c e^{-t/T_1} \quad , \tag{7.10}$$

but this time the decay constant of the fit is the longitudinal relaxation time T_1, which was measured to be of order 17 min. A longitudinal relaxation time of 17 min would only allow for a couple of collection iterations before a the magnetic moment in the storage cell reaches a steady state. The T_1 needs to be improved so that a substantial amount of hyperpolarized ^{3}He can be collected.

7.3 Necessary System Improvements

The measurements described in this section can be used to determine what type of modifications should be made to the MEOP station. The goal of the modifications is to increase the rate of hyperpolarized gas production and to ultimately increase the total magnetic moment of the gas that is collected in the storage cell. The production rate can be improved by operating the laser at full power in conjunction with increasing the flow rate. By operating the laser at 2 W, the power will be increased by a factor of 4. If the flow rate is increased by an equal factor, the same polarization should be produced in the gas while increasing the production rate by a factor of 4. In addition, the total collection time can be increased by repeating the collection process several times. This will increase the total magnetic moment of the gas by increasing the total number of atoms that are collected. However, because of longitudinal relaxation, the magnetization decays during the collection process. Thus, in order for there to be an increase in total magnetic moment, the longitudinal relaxation time must be at least comparable to the total collection time. The T_1 was measured to be 17 min, which is already comparable to the duration of one iteration of a collection process. Thus, the T_1 in the storage cell must be increased.

In Section 2.5.1, it was shown that the longitudinal relaxation is governed by the contributions by wall relaxation and gradient-induced relaxation. The effect of gradient-induced relaxation in the very homogeneous field of the imaging magnet should be small and there should be no paramagnetic O_2 molecules present in the gas sample, which leaves only wall relaxation as the major contributor the longitudinal relaxation. Previous work has shown that applying a thin cesium or rubidium coating to the cell walls can increase the longitudinal relaxation time by two orders of magnitude, however this approach cannot be used here as it is not conducive to the subject's health [24]. There are, however, techniques that can be used to remove impurities from the cell walls, such as igniting low-pressure air-discharges and rinsing with strong acids. Rather than trying to clean the storage cell, it may be worth replacing it with a new cell altogether. This would provide an excellent opportunity to try a different glass-type, such as an aluminosilicate glass [24, 25]. These techniques and maybe others need to be investigated in an effort to increase the longitudinal relaxation time in the storage cell. Longitudinal relaxation times of order several hours will be necessary to efficiently produced and collect hyperpolarized ^{3}He.

The MEOP station still requires several modifications before it can be used to produce hyperpolarized gas samples suitable for MR imaging of lung airspaces. However, the results presented in this chapter demonstrate that the system has been successfully commissioned. In addition, despite the simplicity of the design, the procedure outlined in Chapter 6 can be used to produce a substantial polarization in the hyperpolarized gas that is collected in the storage cell. Once the flow rate, laser power and collection time have been appropriately adjusted, the gas will still need to be transferred to a collapsable container. For this particular system, this container will be a soft plastic (Tedlar$^{\copyright}$) bag which allows subjects to inhale the gas directly into their lungs. Some additional gas-lines will need to be added to the gas handling system to accommodate the transfer of the gas from the spherical glass storage cell to the Tedlar$^{\copyright}$ bag. The ancillary equipment discussed in Chapter 5 will be very useful during the implement these final modifications to the system.

Appendix A

Cell Specifications

Cell	Shape	Dimensions (cm)	Volume (cm^3)
optical pumping cell	cylinder	$\ell = 28.0$, $r = 2.35$	486
storage cell	sphere	$r = 4.25$	322
test cell	cylinder	$\ell = 3.45$, $r = 2.35$	59.9

Bibliography

[1] PC Lauterbur. Image formation by induced local interactions: examples employing nuclear magnetic resonance. *Nature*, 242:190–191, 1973.

[2] JR Mayo and ME Hayden. Hyperpolarized ^{3}He diffusion imaging of the lung. *Radiology*, 222:8–11, 2002.

[3] XJ Chen, HE Möller, MS Chawla, GP Cofer, B Driehuys, LW Hedlun, JR MacFall, and GA Johnson. Spatially resolved measurements of hyperpolarized gas properties in the lung *in vivo* Part II: T_2^*. *Magnetic Resonance in Medicine*, 42:729–737, 1999.

[4] M Estilaei, A Mackay, K Whittall, and J Mayo. In vitro measurements of water content and T_2 relaxation times in lung using a clinical MRI scanner. *Journal of Magnetic Resonance Imaging*, 9:699–703, 1999.

[5] EJR van Beek, JM Wild, H-U Kauczor, W Schreiber, JP Mugler, and EE de Lange. Functional MRI of the lung using hyperpolarized ^{3}He gas. *Journal of Magnetic Resonance Imaging*, 20:540–554, 2004.

[6] CP Bidinosti, J Choukeife, G Tastevin, A Vignaud, and PJ Nacher. MRI of the lung using hyperpolarized ^{3}He at very low magnetic field (3 mT). *MAGMA*, 16:255–258, 2004.

[7] MS Albert, GD Cates, B Driehuys, W Happer, B Saam, CS Springer, and A Wishnia. Biological magnetic resonance imaging using laser-polarized ^{1}29Xe. *Nature*, 370: 199–201, 1994.

[8] HU Kauczor, XJ Chen, EJR van Beek, and WG Schreiber. Pulmonary ventilation imaged by magnetic resonance: at the doorstep of clinical application. *European Respiratory Journal*, 17:1008–1023, 2001.

[9] M Salerno, TA Altes, JP Mugler, M Nakatsu, H Hatabu, and EE de Lange. Hyperpolarized noble gas MR imaging of the lung: Potential clinical applications. *European Journal of Radiology*, 40:33–44, 2001.

[10] HE Möller, XJ Chen, B Saam, KD Hagspiel, GA Johnson, TA Altes, EE de Lange, and HU Kauczor. MRI of the lungs using hyperpolarized noble gases. *Magnetic Resonance in Medicine*, 47:1029–1051, 2002.

[11] M Batz, S Baeβler, W Heil, EW Otten, D Rudersdorf, J Schmiedeskamp, Y Sobolev, and M Wolf. ^{3}He spin filter for neutrons. *Journal of Research of the National Institute of Standards and Technology*, 110(3):293–298, 2005.

[12] TR Gentile, GL Jones, AK Thompson, RR Rizi, DA Roberts, IE Dimitrov, R Reddy, DA Lipson, W Gefter, MD Schnall, and JS Leigh. Demonstration of a compact compressor for application of metastability exchange optical pumping of ^{3}He to human lung imaging. *Magnetic Resonance in Medicine*, 43:290–294, 2000.

[13] PJ Nacher and M Leduc. Optical puming in ^{3}He with a laser. *Journal de Physique*, 46:2057–2073, 1985.

[14] E Courtade, F Marion, PJ Nacher, G Tastevin, K Kiersnowski, and T Dohnalik. Magnetic field effects on the 1 083 nm atomic line of Helium. *European Physics Journal D*, 21:25–55, 2002.

[15] G Tastevin. Optically polarized Helium-3 for NMR imaging in medicine. *Physica Scripta*, T86:46–50, 2000.

[16] NP Bigelow, PJ Nacher, and M Leduc. Accurate optical measurement of nuclear polarization in optically pumped ^{3}He gas. *Journal de Physique II*, 2:2159–2179, 1992.

[17] K Suchanek, K Cieslar, Z Olejniczak, T Palasz, M Suchanek, and T Dohnalik. Hyperpolarized ^{3}He gas production by metastability exchange optical pumping for magnetic resonance imaging. *Optica Applicata*, 35(2):263–276, 2005.

[18] F Laloe, M Leduc, PJ Nacher, LN Novikov, and G Tastevin. Optical polarization of ^{3}He nuclei. *Physical Review C*, 28(11):941–955, 1985.

[19] G Eckert, W Heil, M Meyerhoff, EW Otten, R Surkau, M Werner, M Leduc, PJ Nacher, and LD Schearer. A dense polarized ^{3}He target based on compression of optically pumped gas. *Nuclear Instruments and Methods in Physics Research*, A320: 53–65, 1992.

[20] TE Chupp and ME Wagshul. Polarized, high-density, gaseous ^{3}He targets. *Physical Review C*, 36(6):2244–2251, 1987.

[21] CH Tseng, GP Wong, VR Pomeroy, RW Mair, DP Hinton, and D Hoffman. Low field MRI of laser polarized noble gas. *Physical Review Letters*, 181(17):3785–3788, 1998.

[22] J Coukeife, X Mitre, PJ Nacher, and G Tastevin. On-site production of hyperpolarized ^{3}He for lung MRI. *Magnetic Resonance Materials in Physics, Biology and Medicine*, 15:201, 2002.

[23] TR Gentile, DR Rich, AK Thompson, WM Snow, and GL Jones. Compressing spin-polarized ^{3}He with a modified diaphragm pump. *Journal of Research of the National Institute of Standards and Technology*, 106:709–729, 2001.

[24] W Heil, H Humblot, E Otten, M Schafer, R Sarkau, and M Leduc. Very long nuclear relaxation times of spin polarized ^{3}He in metal coated cells. *Physics Letters A*, 201: 337–343, 1995.

[25] W Heil, J Dreyer, D Hofmann, H Humblot, E Lelievre-Berna, and F Tasset. ^{3}He neutron spin-filter. *Physica B*, 267–268:328–335, 1999.

[26] WA Fitzsimmons, LL Tankersley, and GK Walters. Nature of surface-induced nuclear-spin relaxatin of gaseous ^{3}He. *Physical Review*, 179:156–165, 1969.

[27] J Bernstein, PM Fishbane, and S Gasiorowicz. *Modern Physics*. Princeton Hall, 2000.

[28] FD Colegrove, LD Schearer, and GK Walters. Polarization of ^{3}He gas by optical pumping. *Physical Review*, 132:2561–2572, 1963.

[29] E Durand. *Mise en œvre de l'imagerie par résonance magnétique du noyau d'^{3}He hyperpolarisé et contribution à la caractérisation tissulaire des voies aériennes pulmonaires.* PhD thesis, Université Paris XI (Paris-Sud) UFR Scientifique d'Orsay, 2001.

[30] G Tastevin, S Grot, E Courtade, S Bordais, and PJ Nacher. A broadband ytterbium-doped tunable fiber laser for ^{3}He optical pumping at 1083 nm. *Applied Physics B*, 78: 145–156, 2004.

[31] J Dupont-Roc, M Leduc, and F Laloe. New value for the metastability exchange cross section in helium. *Physical Review Letters*, 27(8):467–470, 1971.

[32] JJ Sakurai. *Modern Quantum Mechanics.* Addison-Wesley Publishing, revised edition, 1994.

[33] PJ Mohr and BN Taylor. CODATA recommended values of the fundamental physical constants: 2002. National Institute of Standards and Technology, 2005.

[34] WS Hinshaw and AH Lent. An introduction to NMR imaging: From the Block equation to the imaging equation. *Proceedings of the IEEE*, 71(3):338–350, 1982.

[35] A Abragam. *The Principles of Nuclear Magnetism.* Oxford University Press, 1961.

[36] EM Chapple. Fundamental SNR and SAR limitations in very low magnetic fields. Master's thesis, Simon Fraser University, 2006.

[37] CP Bidinosti, J Choukeife, PJ Nacher, and G Tastevin. In vivo NMR of hyperpolarized ^{3}He in the human lung at very low magnetic fields. *Journal of Magnetic Resonance*, 162:122–132, 2003.

[38] LD Schearer and GK Walters. Nuclear spin-lattice relaxation in the presence of magnetic-field gradients. *Physical Review*, 139(5A):A1398–A1402, 1965.

[39] RL Gamblin and TR Carver. Polarization and relaxation processes in ^{3}He gas. *Physical Review*, 138(4A):A946–A960, 1965.

[40] B Saam, W Happer, and H Middleton. Nuclear relaxation of ^{3}He in the presence of O_2. *Physical Review A*, 52(1):862–865, 1995.

[41] G Woan. *The cambridge handbook of physics formulas.* Cambridge University Press, 2000.

[42] C Lei. Preparation and characterisation of ^{3}He metastability-exchange optical pumping cells. Master's thesis, Simon Fraser University, 2002.

[43] E Fukushima and SBW Roeder. *Experimental pulse NMR a nuts and bolts approach.* Westview Press, 1981.

[44] MJE Golay. Magnetic field control apparatus. US Patent, 1957.

[45] SR Thomas, LJ Busse, and JF Schenck. *Gradient coil technology: Magnetic resonance imaging*, volume II. WB Saunders Company, 1988.

[46] CP Bidinosti, IS Kravchuk, and ME Hayden. Active shielding of cylindrical saddle-shaped coils: Appliation to wire-wound rf coils for very low NMR and MRI. *Journal of Magnetic Resonance*, 177:31–43, 2005.

[47] R Turner and RM Bowley. Passive screening of switched magnetic field gradients. *Journal of Physics E: Scientific Instruments*, 19:876–879, 1986.

[48] R Turner. Gradient coil design: a review of methods. *Magnetic Resonance Imaging*, 11:903–920, 1993.

[49] National Institute of Standards and Technology: Physical Reference Data. Atomic spectra database. physics.nist.gov/PhysRefData, June 2006.

[50] W Lorenzon, TR Gentile, H Gao, and RD McKeown. NMR calibration of optical measurement of nuclear polarization in ^{3}He. *Physical Review A*, 47(1):468–479, 1993.

[51] JM Jin. Electromagnetics in magnetic resonance imaging. *IEEE Antennas and Propagation Magazine*, 40:7–22, 1998.

[52] JL Hobson. Concomitant gradients in low-field NMR: studies of restricted diffusion. Master's thesis, Simon Fraser University, 2006.